Université de Lille

Laboratoire de Physique des Lasers, Atomes et Molécules (UMR 8523)

Ecole doctorale Sciences de la Matière, du Rayonnement et de l'Environnement

Thèse de Doctorat

Pour obtenir le titre de:

Docteur en Physique

Fibres optiques de spécialité pour endoscopes bio-médicaux ultra-miniaturisés

Présentée par: Fatima EL MOUSSAWI

15 Décembre, 2022

Johannes Fitzgerald DE BOER	PR, Université d'Amsterdam	Rapporteur
Cathie VENTALON	CR, Ecole Normale Supérieure	Rapporteur
Alexandre KUDLINSKI	PR, Université de Lille	Examinateur/ Président
Hervé RIGNEAULT	DR, Aix-Marseille Université	Examinateur
Esben Ravn ANDRESEN	MCF-HDR, Université de Lille	Directeur
Olivier VANVINCQ	MCF-HDR, Université de Lille	Co-Directeur

University of Lille

Laboratory of Physics of Lasers, Atoms and Molecules (UMR 8523)

Doctoral School of Matter, Radiation and Environment Science

Doctoral Thesis

To obtain a title of:

Doctor in Physics

Specialty optical fibers for ultra-miniaturized biomedical endoscopes

Presented by: Fatima EL MOUSSAWI

December 15, 2022

Johannes Fitzgerald DE BOER	PR, University of Amsterdam	Referee
Cathie VENTALON	CR, Ecole Normale Supérieure	Referee
Alexandre KUDLINSKI	PR, University of Lille	Examiner/ President
Hervé RIGNEAULT	DR, Aix-Marseille University	Examiner
Esben Ravn ANDRESEN	MCF-HDR, University of Lille	Supervisor
Olivier VANVINCQ	MCF-HDR, University of Lille	Co-Supervisor

Publications

Articles

- Fatima El Moussawi, Matthias Hofer, Damien Labat, Andy Cassez, Géraud Bouwmans, Siddharth Sivankutty, Rosa Cossart, Olivier Vanvincq, Hervé Rigneault, and Esben Ravn Andresen, "Tapered Multicore Fiber for Lensless Endoscopes", In: *ACS Photonics* 9.8 (2022), pp. 2547–2554. doi: https://doi.org/10.1021/acsphotonics.2c00661.

Conferences

- Fatima El Moussawi, Matthias Hofer, Damien Labat, Andy Cassez, Géraud Bouwmans, Siddharth Sivankutty, Rosa Cossart, Olivier Vanvincq, Hervé Rigneault, and Esben Ravn Andresen, "Specialty multi-core optical fiber for biomedical lensless endoscopes", in Advanced Photonics Congress, Maastricht, 2022.

- El Moussawi, M. Hofer, N. G. Kumar, A. Cassez, D. Labat, G. Bouwmans, O. Vanvincq, H. Rigneault, and E. R. Andresen, "Tapered multi-core fiber for biomedical lens-less endoscopes," in *2022 Conference on Lasers and Electro-Optics (CLEO)*, pp. 1–2, IEEE, 2022. San José, 2022.

- Fatima El Moussawi, Esben Ravn Andresen, Olivier Vanvincq, Géraud Bouwmans, "Specialty optical fibers for ultra-miniaturized biomedical endoscopes", in Optique Dijon 2021, Dijon, 2021.

UNIVERSITÉ DE LILLE

Résumé

Laboratoire PhLAM

Fibres optiques de spécialité pour endoscopes bio-médicaux ultra-miniaturisés

par Fatima El Moussawi

L'endoscope sans lentille est un outil d'imagerie prometteur, ultra-miniaturisé, qui pourrait permettre une imagerie in-vivo peu invasive et à résolution cellulaire des tissus biologiques profonds. L'idée principale de l'endoscope sans lentille est un dispositif que l'on peut monter sur la tête d'un petit animal, et qui ne contient qu'un guide d'onde optique capable de collecter la lumière, de conserver son contenu d'information et de l'acheminer vers des systèmes optiques et opto-électroniques déportés. L'intérêt de cet endoscope miniaturisé réside dans sa capacité à permettre de nouvelles fonctionnalités puisque la source de lumière et les détecteurs sont déportés ainsi que dans la légèreté et la flexibilité des fibres optiques qui constituent ici la partie principale du système d'imagerie. Nous présentons dans cette thèse un nouveau composant à fibre optique, une "fibre multi-cœur effilée", conçue pour être intégrée dans des endoscopes ultra-miniaturisés pour l'imagerie à balayage à deux photons minimalement invasive et pour résoudre le problème de livraison de puissance auquel sont confrontés les endoscopes sans lentille basés sur la fibre multi-cœurs. Nous présentons la conception, la fabrication, la caractérisation et l'application de la fibre multi- cœurs effilée, qui nous a permis de réaliser l'imagerie à deux-photons d'échantillons fluorescents dans les sens avant et arrière. Nos résultats montrent que le façonnage du profil effilé de la fibre multi-cœurs apporte de nouveaux degrés de liberté qui peuvent être exploités efficacement pour les endoscopes sans lentille.

Mots clés: Endoscopes, fibre optique, ultra miniaturisé, matrice de transmission.

UNIVERSITÉ DE LILLE

Abstract

Laboratoire PhLAM

Specialty optical fibers for ultra-miniaturized biomedical endoscopes

by Fatima El Moussawi

The lens-less endoscope is a promising ultra-miniaturized imaging tool with the potential to enable minimally invasive and cellular-level resolution in-vivo imaging deep inside biological tissue. The main idea of the lens-less endoscope is a device capable of being fixed on the head of a small animal containing only an optical waveguide capable of collecting light, retaining its information content, and transporting it fiber-optically to remote optics and opto-electronics. The interest of this miniaturized endoscope stems from its ability to allow new functionalities because light source and detectors are remote as well as the light weight and flexibility of the optical fibers that constitute here the main part of the imaging system. We present in this thesis a novel fiber-optic component, a "tapered multi-core fiber", designed for integration into ultra-miniaturized endoscopes for minimally invasive two-photon point-scanning imaging and to address the power delivery issue that has faced multi-core fiber-based lens-less endoscopes. We report the design, fabrication, characterization and application of the tapered multi-core fiber, where we were able to perform two-photon imaging of fluorescent samples in both forward and backward directions. Our results show that tailoring of the taper profile of the multi-core fiber brings new degrees of freedom that can be efficiently exploited for lens-less endoscopes.

Keywords: Endoscopes, optical fiber, ultra-miniaturized, transmission matrix.

Acknowledgements

I take this opportunity to express my heartfelt gratitude to all those who have helped and supported me in the successful completion of this thesis.

First of all, I would like to thank the members of my thesis committee, the president and examiner Mr. Alexandre Kudlinski, the referees Mr. Johannes Fitzgerald De Boer and Mme. Cathie Ventalon, and the examiner Mr. Hervé Rigneault, for accepting this role and dedicating their time in order to evaluate my thesis works. I am also thankful for their valuable comments and interesting questions that make me think more about the far future of my work.

I would like to express my sincere gratitude to my thesis supervisor, Mr. Esben Ravn Andresen, for his exceptional guidance throughout my thesis. You have been a tremendous supervisor for me, thank you for helping me to advance as a research scientist. I feel truly fortunate to have had the opportunity to work with such a creative genius supervisor. I also deeply appreciated your kindness, attention and support on the daily basis.

I would like to extend my sincere thanks to Mr. Olivier Vanvincq, the supervisor of the second and third years of my PhD, and Mr. Géraud Bouwmans, the supervisor of the first year of my PhD. Their expertise and insights have been indispensable in the successful completion of this thesis.

I'm extremely grateful to the collaborators who contributed in this work, Mr. Hervé Rigneault and Matthias Hofer from Fresnel Institute in Marseille. Many thanks to Matthias Hofer, it was a pleasure participating in your manip at Fresnel Institute, I really appreciate your cooperation. Thank you for being generous in answering my questions and providing me with any information and data I was in need.

I am also grateful to Mr. Rémy Bernard and Aymeric Pastre from the Photonics team at PhLAM laboratory, their expertise and skills in fiber coating have greatly enhanced the quality of my work in developing the genuine endoscope.

I would like to thank Mr. Serge Monneret and Mr. Laurent Heliot for being members of my PhD monitoring committee and giving instructive remarks and suggestions.

It is worth to mention that this thesis has benefited greatly from the ability to fabricate the designed multi-core fibers in house at the FiberTech Lille. I would like to thank the researchers and engineers at the technology central FiberTech, particularly Mr. Andy Cassez and Mr. Géraud Bouwmans. And a special thanks to Damien Labat who generously took the time to teach me the necessary skills to use certain equipment. I appreciate your help more than words can express.

I would like to also thank all the members of the PhLAM Photonics team at the IRCICA research institute, I was really glad to work with such friendly and humour team. And a special thanks to the team leader Laurent Bigot.

I'm deeply indebted to my family: my parents Ali and Claudia, my brother Mohamad Mahdi, and my sister Mariam, for their love, prayers, caring and sacrifices for educating and preparing me for what I am today. Thank you for always believing in me.

Last but not least, my deepest gratitude thanks to my husband, Mohamad Baker, for his support, encouragement, and love throughout my research journey. I couldn't have accomplished this without his constant support and motivation. Thank you for being a pillar of strength, and for being my life partner.

Fatima El Moussawi

Contents

List of Figures

List of Tables

List of Abbreviations

FE-BPM	**F**inite **E**lement-**B**eam **P**ropagation **M**ethod
CCD	**C**harge **C**oupled **D**evice
CMT	**C**oupled **M**ode **T**heory
DM	**D**eformable **M**irror
DMD	**D**igital **M**irror **D**evice
FWHM	**F**ull **W**idth at **H**alf **M**aximum
GDD	**G**roup **D**elay **D**ispersion
GFP	**G**reen **F**luorescent **P**rotein
LP	**L**inearly **P**olarized
ME	**M**emory **E**ffect
MFD	**M**ode **F**ield **D**iameter
MMF	**M**ulti-**M**ode **F**iber
MCF	**M**ulti-**C**ore **F**iber
NA	**N**umerical **A**perture
PSF	**P**oint-**S**pread **F**unction
PMT	**P**hoto**M**ultiplier **T**ube
SMF	**S**ingle-**M**ode **F**iber
SLM	**S**patial **L**ight **M**odulator
TIR	**T**otal **I**nternal **R**eflection
TPF	**T**wo-**P**hoton **F**leurescence
TPEF	**T**wo-**P**hoton **E**xcitation **F**leurescence
TM	**T**ransmission **M**atrix

Notation

Bold lower-case letter (e.g. $\mathbf{v}$) denotes a vector.
Bold upper-case letter (e.g. $\mathbf{M}$) denotes a matrix.

Introduction

In recent years numerous efforts have been made to miniaturize imaging instruments to enable cellular-level imaging in behaving animals. A current instance is the head-mounted miniaturized microscope for fluorescence imaging. This approach has all optical and opto-electronic elements integrated into a miniature device that is easily head-mounted and carried by rodents, thus it permits studying the cells in their natural environment. Evidently, the smaller the imaging instrument the better, especially for non-invasive imaging. But miniaturizing optical elements has a limit and thus it is still invasive, disturbing the rodent under study and prevent it from moving freely.

Fortunately, there is another approach of miniaturized imaging tools, which bases the light delivery and collection on an optical fiber. Thus it brings the advantage that the light source and detectors can be remote rather than integrated in the head-mounted device. This approach refers to fiber optic endoscopes, and we refer to as "lens-less endoscopes", meaning endoscopes without optics or other elements attached to the distal tip of the endoscope probe, which is the optical fiber itself. Therefore, there is nothing that increases the bulkiness of this fiber probe beyond the diameter of the waveguide itself. With a standard optical fiber of 125 μm outer diameter, this would allow for ultra-thin imaging probes, potentially capable of noninvasive deep-tissue endoscopic imaging. Also, this could reduce space constraints, thus allow fixing several probes simultaneously and thus the ability to study functional connectivity of neurons in two distant brain regions. Moreover, standard optical fibers are highly flexible, this gives the fiber probe the benefit to be fixed onto mouse's head allowing its free movement while studying neuronal activity.

The concept of lens-less endoscope relies on using a spatial-light modulator (SLM) to shape the wavefront going into the fiber. Since the fiber is a linear medium which means that it can be described mathematically by a transmission matrix (TM), the wavefront coming out the other end of the fiber is also shaped; the output is usually shaped into a focus that is then scanned across the transverse plane of the sample under study for point-scanning imaging.

This thesis presents a specialty optical fiber "tapered multi-core fiber" designed for integration into ultra-miniaturized endoscopes for minimally invasive two-photon point-scanning imaging. We report the design, fabrication, characterization and application of the tapered multi-core fiber, and quantify the gains in imaging performance.

Outline of the manuscript

The dissertation is composed of six chapters. The first chapter presents an overview of the basic notions and theories on which our work is based.

The second starts with the fundamental concepts for the formation of an image, through a linear optical system, in Fourier optics. Then displays technical concepts of optical microscopy imaging techniques. Afterwards, we present the current state-of-the-art in miniaturized imaging tools and the latest endoscopes that were applied in neuron imaging. This chapter ends with the positioning of this thesis work.

The third chapter presents a numerical investigation of a potential solution for ameliorating spatial resolution in lens-less endoscopes..

The fourth chapter is dedicated to the main results of our work. It includes the model, the design, the fabrication, the characterization and the application of a novel specialty multi-core fiber lens-less endoscope.

The fifth chapter is an extension and further advance of the work presented in Chapter 4.

Finally, chapter six is the conclusion and perspectives.

Chapter 1

Theory

1.1 Introduction

This chapter will present the concepts required for a thorough understanding of this manuscript. It starts by introducing the principles of light transmission in optical fibers and presenting its characteristics. Then, presents the propagation of light in optical fibers in matricial formalism by defining the transmission matrix and expressing it in different basis. Furthermore, last section demonstrates the coupled-mode theory to analyze coupling between waveguides.

1.2 Guiding mechanism: Total internal reflection

Optical fiber is a cylindrical dielectric waveguide made of a low-loss material, such as silica glass. The simplest optical fiber is made up of homogeneous core with index n_{co}, surrounded by a cladding of slightly lower refractive index n_{clad}. Since the core has a higher index of refraction than the cladding, light beam is confined to the core if the angular condition for Total Internal Reflection (TIR) is met at the core/cladding interface. Consequently, light rays undergo total internal reflection and are guided through the core without refraction into the cladding. These rays of light continue to experience total internal reflection as it encounters core/cladding interfaces while propagating down the fiber until it emerges from the other side.

Light rays with incident angle θ_i passes freely through the core of the optical fiber after refraction at the air/core interface, with angle ϕ given by Snell's law as:

$$\sin\phi = \sin\theta_i / n_{\text{co}} \tag{1.1}$$

Inside the core, the light ray strikes the core/cladding interface at an angle $(\frac{\pi}{2} - \phi)$. Then the condition for total internal reflection at the core/cladding interface is given by the following equation:

$$n_{\text{co}} \ \sin(\frac{\pi}{2} - \phi) \geq n_{\text{clad}} \tag{1.2}$$

Since the angle ϕ is related with the incident angle θ_i by $\sin\theta_i = n_{\text{co}} \sin\phi \leq \sqrt{n_{\text{co}}^2 - n_{\text{clad}}^2}$, we obtain the critical condition for the total internal reflection to

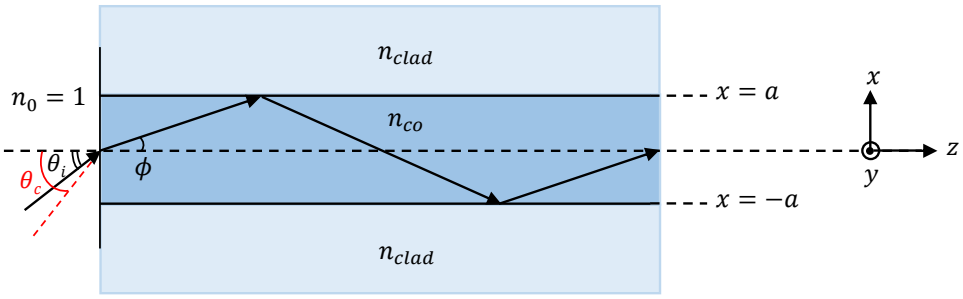

FIGURE 1.1: Description of the Total Internal Reflection (TIR) in an optical fiber.

occur is that incident angle θ_i should be less than a critical angle θ_c, which is defined as:

$$\theta_c = \sin^{-1}(n_{\text{clad}}/n_{\text{co}}) \tag{1.3}$$

The maximum incident angle ($\theta_{i,max}$) at which light is guided defines the numerical aperture (NA) of the fiber. NA is the measure of the ability of an optical fiber to collect or confine the incident light ray inside its core, in another words its the light guiding capacity of an optical fiber. NA is given by the following equation:

$$NA = n_0 \sin(\theta_{i,max}) = \sqrt{n_{\text{co}}^2 - n_{\text{clad}}^2} \tag{1.4}$$

The geometric approach to waveguides; which present in this section; fails to describe them completely. The complete description of waveguides is provided by the electromagnetic approach, as we will detail in the following sections.

1.3 Wave equations

The first theoretical description of mode propagation along a dielectric guide was done by Hondros and Debye in 1910. The first dielectric waveguide to be examined at optical frequencies was the glass fiber used primarily for fiber optics imaging applications [1].

Waveguides are usually defined as a cylindrical structure used for guiding the flow of electromagnetic wave in a direction parallel to its axis, confining it to a region either within or adjacent to its surfaces. In order to study the propagation of light in a waveguide, it is imperative to derive the wave equations. The electromagnetic wave equation can be derived from Maxwell's equation (formulated by James Clark Maxwell in 1865), assuming that we are operating in a source free (charge density ρ and current density $\vec{J}$ are null) , linear (electric permitivity ϵ and magnetic permeability μ of the medium are independent of

E and H), and an isotropic medium. E and H are the electric and magnetic field of electromagnetic wave respectively.

$$\vec{\nabla} \times \vec{E} = -\mu_0 \frac{\partial \vec{H}}{\partial t} \tag{1.5}$$

$$\vec{\nabla} \times \vec{H} = \epsilon_0 n^2 \frac{\partial \vec{E}}{\partial t} \tag{1.6}$$

$$\vec{\nabla} \cdot \epsilon_0 n^2 \vec{E} = 0 \tag{1.7}$$

$$\vec{\nabla} \cdot \mu_0 \vec{H} = 0 \tag{1.8}$$

Applying the curl operator on Equation (1.7) and substituting in Ampere's law in a source free region, the wave equations of the electric and magnetic fields can be written respectively as:

$$\vec{\nabla}^2 \vec{E} - \mu_0 \epsilon \frac{\partial^2 \vec{E}}{\partial t^2} = 0 \tag{1.9}$$

$$\vec{\nabla}^2 \vec{H} - \mu_0 \epsilon \frac{\partial^2 \vec{H}}{\partial t^2} = 0 \tag{1.10}$$

ϵ is related to its respective value in a vacuum by: $\epsilon = \epsilon_0 \epsilon_r = n^2 \epsilon_0$ and related to μ_0 by $\epsilon_0 \mu_0 c^2 = 1$. Where c is the light velocity in a vacuum ($c = 1/\sqrt{\epsilon_0 \mu_0}$) and n is the refractive index of the medium.

For the analysis of wave propagation in optical fibers, which are homogeneous and axially symmetric, we consider a monochromatic wave propagating along z-direction and its electromagnetic fields (electric field $\vec{E}$ and magnetic field $\vec{H}$) can be expressed as:

$$\vec{E}(\vec{r}, t) = \vec{E}(r, \theta) e^{i(\beta z - \omega t)} \tag{1.11}$$

$$\vec{H}(\vec{r}, t) = \vec{H}(r, \theta) e^{i(\beta z - \omega t)} \tag{1.12}$$

where r denotes the position in the plane transverse to the z-axis and θ is the phase. ω is the angular frequency of the sinusoidally varying electromagnetic fields with respect to time, $\omega = 2\pi c/\lambda$, with λ the wavelength.

1.3.1 Characteristics of propagating guided modes

The modes are the solutions for the propagation of the light. Guided modes are characterized by a transverse energy distribution of constant amplitude, invariant during propagation. And a wave-vector $\vec{k}$ whose norm is called the wavenumber and is related to the angular frequency by the dispersion relation

$$k = n_{\text{co}} k_0 = n_{\text{co}} \frac{\omega}{c} \tag{1.13}$$

Noting that k_0 is the wavenumber in a vacuum, and related to the wavelength by

$$k_0 = \frac{2\pi}{\lambda} \tag{1.14}$$

The projection of the wave vector on the axis of propagation (z-direction) is what defines the propagation constant β

$$\beta = k_z = k_0 \; n_{\text{co}} \; \cos\theta \tag{1.15}$$

Then each guided mode has a discrete propagation constant which satisfies

$$n_{\text{clad}} \; k_0 < \beta < n_{\text{co}} \; k_0 \tag{1.16}$$

Then we can define the effective index n_{eff} which is the refractive index experienced by the mode while propagating with propagation constant β. n_{eff} is a dimensionless value and it is expressed as:

$$n_{\text{eff}} = \frac{\beta}{k_0} \tag{1.17}$$

The mode can be guided within the optical fiber if its propagation is possible in the core but not in the cladding. Therefore the effective indices of guided modes constitute a discrete and finite set and satisfy the following condition:

$$n_{\text{clad}} \leq n_{\text{eff}} \leq n_{\text{co}} \tag{1.18}$$

In each optical fiber, we can introduce the following normalized parameters:

$$U = \frac{2\pi}{\lambda} \; a \; \sqrt{n_{\text{co}}^2 - n_{\text{eff}}^2} \tag{1.19}$$

$$W = \frac{2\pi}{\lambda} \; a \; \sqrt{n_{\text{eff}}^2 - n_{\text{clad}}^2} \tag{1.20}$$

These parameters are related by the following equation

$$U^2 + W^2 = V^2 \tag{1.21}$$

Where V is called the normalized frequency and represented by the following equation

$$V = \frac{2\pi}{\lambda} \; a \; \sqrt{n_{\text{co}}^2 - n_{\text{clad}}^2} \tag{1.22}$$

The normalized frequency depends on the structural parameters of the fiber: the core radius, the core refractive index, the cladding refractive index, and the working wavelength.

Indeed, within plane electromagnetic waves, there are points of constant phase. These constant phase points form a surface called a wavefront. As a monochromatic light wave propagates along a waveguide in the z-direction these points of constant phase travel at a phase velocity v_p given by

$$v_p = \frac{\omega}{\beta} = \frac{c}{n_{\text{eff}}} \tag{1.23}$$

the group velocity v_g is the propagation velocity of the electric field envelope

$$\begin{aligned} v_g &= \frac{\mathrm{d}\omega}{\mathrm{d}\beta} \\ &= \frac{\mathrm{d}\lambda}{\mathrm{d}\beta} \cdot \frac{\mathrm{d}\omega}{\mathrm{d}\lambda} \end{aligned} \tag{1.24}$$

Substituting $\beta = n_{\text{eff}} k_0$ from Equation (1.17), $k_0 = 2\pi/\lambda$, $\omega = 2\pi c/\lambda$, we obtain

$$v_g = \frac{c}{\left(n_{\text{eff}} - \lambda \frac{\mathrm{d}n_{\text{eff}}}{\mathrm{d}\lambda}\right)} \tag{1.25}$$

Equation (1.25) is comparable to Equation (1.23), therefore the group index n_g is given by

$$n_g = n_{\text{eff}} - \lambda \frac{\mathrm{d}n_{\text{eff}}}{\mathrm{d}\lambda} \tag{1.26}$$

1.4 Weakly guiding fibers

The refractive-index difference Δn of practical fibers is very small ($\Delta n << 1$), this means that core and cladding refractive indices are nearly the same ($n_{\text{co}}/n_{\text{clad}} \approxeq 1$). The analysis of fibers based on the approximation with $n_{\text{co}}/n_{\text{clad}} \approxeq 1$ was first presented by Snyder [2]. Afterwards Gloge [3] used the term "weakly guiding fiber" for describing these optical fibers and he designated the mode groups of weakly guiding fiber as linearly polarized (LP) modes. Therefore, the LP modes are the approximate modes of the fibers in the weakly guiding approximation.

1.4.1 Wave theory in step-index fiber

The step-index fibers have a transverse refractive index profile defined by

$$n(r) = \begin{cases} n_{\text{co}} & \text{for } 0 \leq r < a \\ n_{\text{clad}} & \text{for } r > a \end{cases} \tag{1.27}$$

And is characterized by its refractive index step $\Delta n = n_{\text{co}} - n_{\text{clad}}$ and its core radius a, and its refractive index profile is shown in Figures 1.2(a) and 1.2(b).

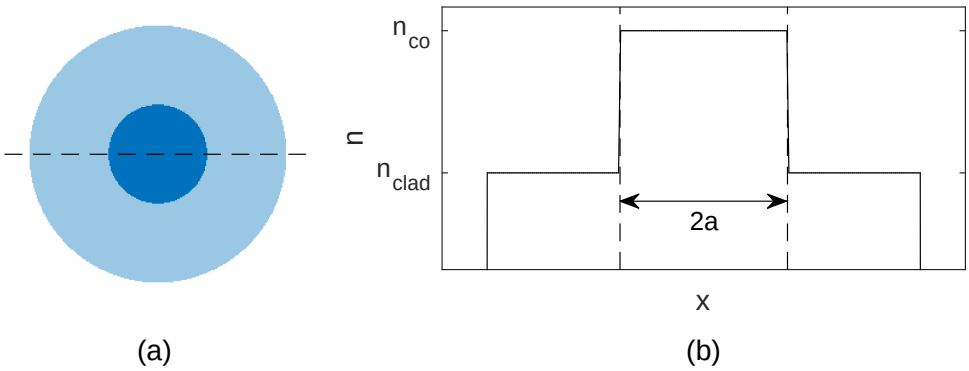

FIGURE 1.2: (a) Structure of step-index fiber. (b) Refractive index profile along the dashed line in (a).

Eigenvalue equation

The wave equation of electric field in weakly guiding fiber with a step index profile is given by:

$$\vec{\nabla}^2 \vec{E}(\vec{r}) + k_0 n^2 \vec{E}(\vec{r}) = \vec{0} \tag{1.28}$$

The LP modes are determined by assuming $E_z = 0$. Then E_x and E_y components are independent and therefore each mode can be linearly polarized along x or y. In other words, each spatial mode can exist in two polarization states, and can then be written as:

$$\vec{E}_x = \psi_l(r, \phi)\ \hat{x} \tag{1.29}$$
$$\vec{E}_y = \psi_l(r, \phi)\ \hat{y} \tag{1.30}$$

where the spatial mode $\psi_l(r, \phi)$ is a function of spatial coordinates. And the unit vectors $\hat{x}$ and $\hat{y}$ determine the two polarization directions (x and y) that define the linearly polarized modes.

Due to circular symmetry around the optical axis. These modes must be invariant for a rotation of 2π, and their equations have the following solutions:

$$E_{x,y} = \psi_l(r, \theta) = \psi(r) \begin{cases} \cos(l\ \theta) \\ \sin(l\ \theta) \end{cases} \tag{1.31}$$

where l (integer) is the azimuthal modal number. The cosine solutions correspond to LP "even" modes and the sine solutions correspond to the LP "odd"

modes. The difference between even and odd modes is a $\pi/2$ rotation of the fields around the propagation axis.

The basic wave equation for step-index fibers is given in term of the transverse field function ψ which satisfies Bessel's differential equation:

$$\frac{\partial^2\psi_l(r)}{\partial r^2} + \frac{1}{r}\frac{\partial\psi_l(r)}{\partial r} + (k_0^2 n^2 - \beta^2 - \frac{l^2}{r^2})\psi_l(r) = 0 \tag{1.32}$$

Equation (1.32) is a scalar wave equation which determines the propagation constants β of the LP scalar modes. This equation must be satisfied at the different interfaces between the media constituting the fiber. Thus $\psi_l(r)$ and its derivatives are continuous at each interface in the fiber, for example at the core/cladding interface (where $r = a$).

Equation (1.32) is the differential equation of the Bessel J_l and Y_l or the modified Bessel functions I_l and K_l according to the sign of $k_0^2 a^2(n^2 - n_{\text{eff}}^2)$. To find the solutions of this equation, we will only keep the solutions that don't diverge for $r = 0$ and $r \to \infty$ and as we are dealing with guided modes then we have $n_{\text{clad}} < n_{\text{eff}} < n_{\text{co}}$. Thus the possible solutions of Equation (1.32) are as follows

- In the core, $r \leq a$ and $n_{\text{clad}} \leq n_{\text{eff}} \leq n_{\text{co}}$, then $k_0^2 a^2(n_{\text{co}}^2 - n_{\text{eff}}^2) \geq 0$, and thus the solution is the Bessel function J_l, because Bessel function Y_l diverges at $r = 0$. Therefore, $U^2 = k_0^2 a^2(n_{\text{co}}^2 - n_{\text{eff}}^2) > 0$ and the solution of $\psi_l(r)$ is

$$\psi_l(r) = J_l(Ur/a)/J_l(U) \tag{1.33}$$

- In the cladding, $r > a$ and $n_{\text{eff}} > n_{\text{clad}}$, then $k_0^2 a^2(n_{\text{clad}}^2 - n_{\text{eff}}^2) < 0$, and thus the solution is the Bessel function K_l, because Bessel function I_l diverges when r tends to ∞. Therefore, $W^2 = k_0^2 a^2(n_{\text{eff}}^2 - n_{\text{clad}}^2) > 0$ and the solution of $\psi_l(r)$ is

$$\psi_l(r) = K_l(Wr/a)/K_l(W) \tag{1.34}$$

The denominators $J_l(U)$ and $K_l(W)$ of Equations (1.33) and (1.34) respectively, ensure the continuity of $\psi_l(r)$ at $r = a$. Then, to establish the eigenvalue equation, it is necessary to express the continuity of the derivative of $\psi_l(r)$ at $r = a$:

$$U\frac{J_l'(U)}{J_l(U)} = W\frac{K_l'(W)}{K_l(W)} \tag{1.35}$$

Where the derivatives of the functions J_l and K_l are

$$J_l'(U) = \frac{l}{U} J_l(U) - J_{l+1}(U) \tag{1.36}$$

$$K_l'(W) = \frac{l}{W} K_l(W) - K_{l+1}(W) \tag{1.37}$$

Substituting Equations (1.36) and (1.37) in Equation (1.35), we obtain the eigenvalues equation for LP modes

$$U \frac{J_{l+1}(U)}{J_l(U)} = W \frac{K_{l+1}(W)}{K_l(W)} \tag{1.38}$$

Equation (1.38) can be written in another useful form as

$$U \frac{J_{l-1}(U)}{J_l(U)} = -W \frac{K_{l-1}(W)}{K_l(W)} \tag{1.39}$$

using the second form of derivatives of J_l and K_l as

$$J_l'(U) = -\frac{l}{U} J_l(U) + J_{l-1}(U) \tag{1.40}$$

$$K_l'(W) = -\frac{l}{W} K_l(W) - K_{l-1}(W) \tag{1.41}$$

Equations (1.38) and (1.39) are equivalent, and both represent the eigenvalue equation of LP modes. Solving these eigenvalue equations for each value of l gives several solutions. These solutions are series of discrete U_{lm} values where l is the azimuthal number which determines the order of the Bessel functions J_l and K_l, and m is an integer that represents the order of the solution of the eigenvalue equation. U_{lm} is a function of the effective indices n_{eff}, which in its term allows us to determine the value of the propagation constants β of the guided modes. Therefore, each U_{lm} solution represents a guided mode and any modal solution U_{lm} of a linearly polarized guided mode LP_{lm} is comprised between a cutoff value U_c determined by the condition $U \to V$) and a value U_∞ far from the cutoff ($V \to \infty$).

As mentioned in the above paragraph, U_{lm} is a function of the effective indices n_{eff}, thus we can also represent the solutions of the eigenvalue equations by

$$n_{\text{eff}}(V) = \frac{\beta}{k_0} = n_{\text{co}} \sqrt{1 - \frac{(n_{\text{co}}^2 - n_{\text{clad}}^2)\, U^2}{n_{\text{co}}^2\, V^2}} \tag{1.42}$$

Figure 1.3 represents the solutions $n_{\text{eff}}(V)$ (also called the dispersion curves) of the first fifteen LP modes ($0 < \text{V} < 10$) in a step-index fiber, showing their cut-off normalized frequencies (black circles). Noting that each mode has a specific cut-off V-value V_c, by which higher-order modes are cutoff.

As shown by Figure 1.3, the first mode or fundamental mode LP_{01} always exists, since its cutoff frequency is zero. And to be in a single mode region, it is necessary to have V less than the cut-off frequency of the second mode (LP_{11}). In order to obtain higher-order guided modes, the value of the normalized frequency V must exceed the cut-off value V_c of each mode for it to exist. Then, the number of guided modes is the number of lines (that are presented in the figure) which intersect with a vertical line at a given V-value. Moreover, we can see from Figure 1.3 that for a given mode n_{eff} increases as V-value increases. Also, $n_{\text{eff}} \to n_{\text{clad}}$ when $V \to V_c$. On the other hand, $n_{\text{eff}} \to n_{\text{co}}$ when $V \to \infty$.

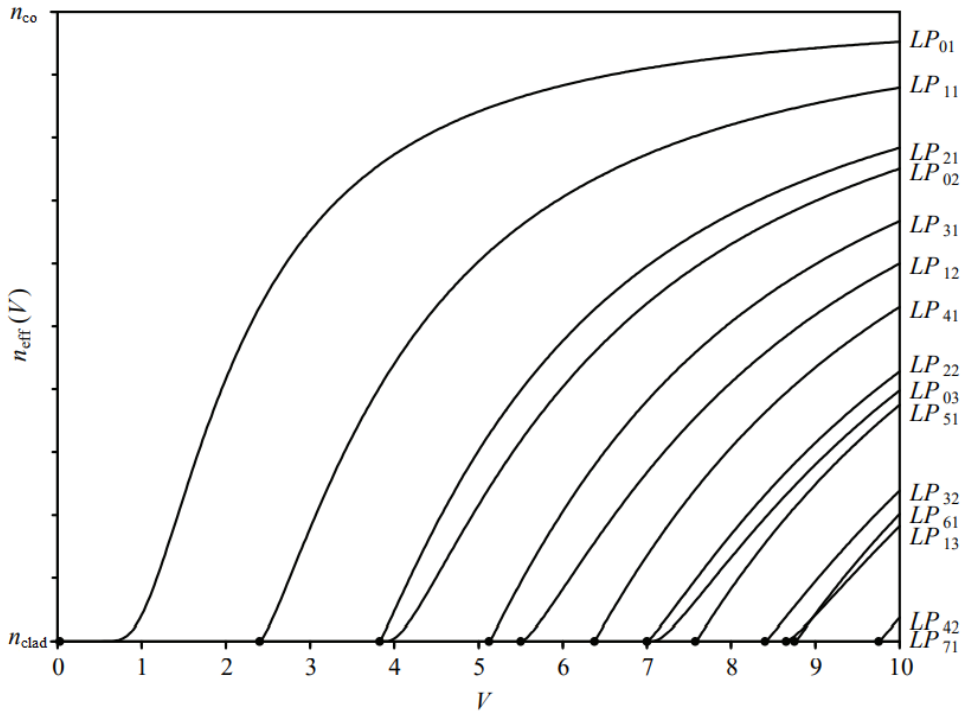

FIGURE 1.3: neff values for the first 15 guided LP modes for a fiber with $\Delta n = 5 \cdot 10^{-3}$ [4]. The black dots show the cut-off frequency of each mode.

The LP_{lm} modes have two different degeneracy types: (i) the spatial degeneracy between even and odd modes (as shown by Equation (1.31) and (ii) the polarization degeneracy, x and y, depending on the polarization state of the mode's electric field. In general:

- For $l = 0$, the LP_{0m} modes are degenerated twice (x and y polarization).
- For $l > 0$, the LP_{lm} modes are degenerated four times (x and y polarization, even in $\cos l\theta$ and odd in $\sin l\theta$).

The degeneracy states of the first four combination of LP modes is shown in Table 1.1.

Figure 1.4 show the field intensity distribution of the first four LP modes. And Figure 1.5 show the two states of polarizations of the electric field of the first four LP modes. The x and y polarizations of the modes with $l = 0$

(LP_{01} and LP_{02}) are identical and can be deduced from each other by a $\pi/2$ rotation. However, this is not the case for $l > 0$, because these modes have different symmetries. Note that, since the wave is quasi transverse electromagnetic (quasi-TEM) in weak guidance, the polarization of the magnetic field is perpendicular to that of the electric field.

LP mode	Spatial degeneracy	Polarization degeneracy
LP_{01}	LP_{01}	LP^{x}_{01}, LP^{y}_{01}
LP_{11}	$LP^{(e)}_{11}$ $LP^{(o)}_{11}$	$LP^{(e),x}_{11}$, $LP^{(e),y}_{11}$, $LP^{(o),x}_{11}$, $LP^{(o),y}_{11}$
LP_{21}	$LP^{(e)}_{21}$ $LP^{(o)}_{21}$	$LP^{(e),x}_{21}$, $LP^{(e),y}_{21}$, $LP^{(o),x}_{21}$, $LP^{(o),y}_{21}$
LP_{02}	LP_{02}	LP^{x}_{02}, LP^{y}_{02}

TABLE 1.1: The degeneracy states of the first four combination of LP mode

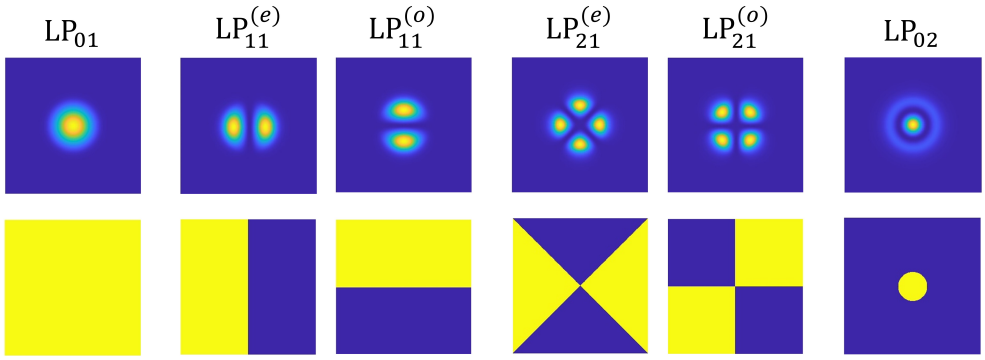

FIGURE 1.4: Amplitude (upper line) and phase (lower line) profiles of the first four LP modes with their even (e) and odd (o) degeneracy.

Example: Propagation of two modes

Assume two modes p and q being launched into a waveguide. These two guided modes superpose as they propagate through the waveguide along its optical axis. Due to slightly different in propagation constants, there will be beats between the two modes. Therefore, we define a beat length L_{beat}, which is the distance after which there is total transfer of power from one mode to another and back again, and thus:

$$L_{\text{beat}} = \frac{2\pi}{|\beta_p - \beta_q|} \tag{1.43}$$

As an example, we consider a weakly guiding step-index fiber with core radius $a = 1.5$ μm and refractive index step $\Delta n = 0.01$. We study the superposition of the LP_{01} and $LP^{(e)}_{11}$ modes while propagating through the fiber at wavelength $\lambda = 700$ nm with $\Delta n_{\text{eff}} = n_{\text{eff}}(LP_{01}) - n_{\text{eff}}(LP_{11}) = 0.0053$. The total

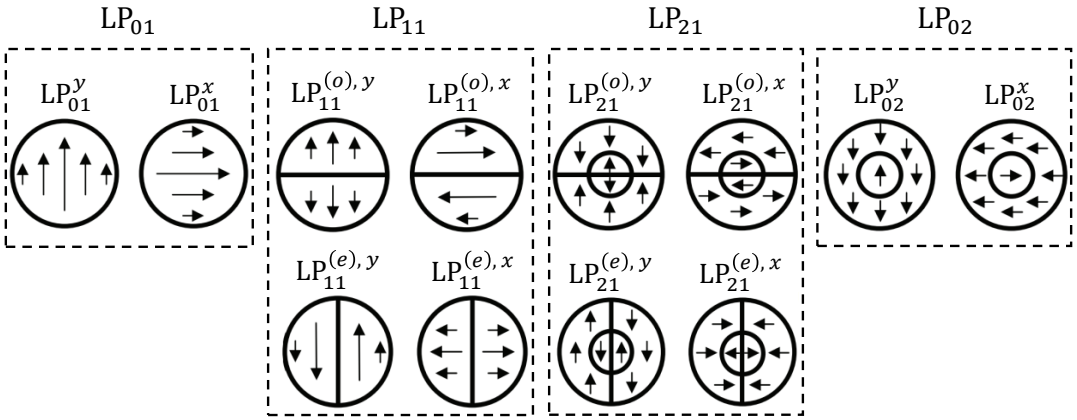

FIGURE 1.5: The two states of polarizations x and y of the electric fields for the first four LP modes. The large circles represent the core/cladding interface. The small circles indicate the zeros of the field.

field is the result of the superposition of the amplitudes of the two modes and its evolution along z will translate the beat between them. Figure 1.6 presents the superposition of the two modes at several z positions along its optical axis, related to the beat length of the modes.

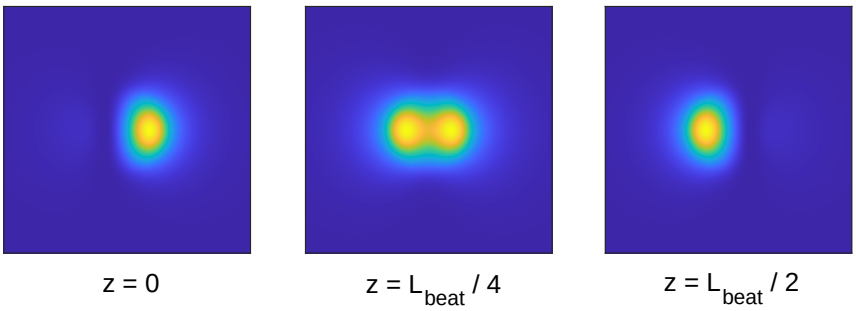

FIGURE 1.6: Superposition of LP_{01} and $\mathrm{LP}_{11}^{(e)}$ at different z positions while propagating along the fiber.

1.4.2 Wave theory in graded-index fiber

A graded index optical fibre contains, as the name suggests, a core of varying refractive index profile. Typically, a refractive index that decreases with increasing radial distance from the optical axis of the fiber. The refractive index profile of the graded-index fiber is defined by

$$n(r) = \begin{cases} n_{\mathrm{co}} \left(1 - 2\Delta \left(\frac{r}{a}\right)^{\alpha}\right)^{1/2} & \text{for } \; 0 < r < a \\ n_{\mathrm{clad}} & \text{for } \; r > a \end{cases} \tag{1.44}$$

where Δ is the maximum refractive index difference, r is the radial distance from the centre of the fibre, a is core radius, and α is the grade profile parameter. The

grade profile parameter describes the shape of the graded index and is assumed to range between 1 and ∞. For example, α= 2 represents the parabolic-index profile and $\alpha = \infty$ corresponds to the step-index profile.

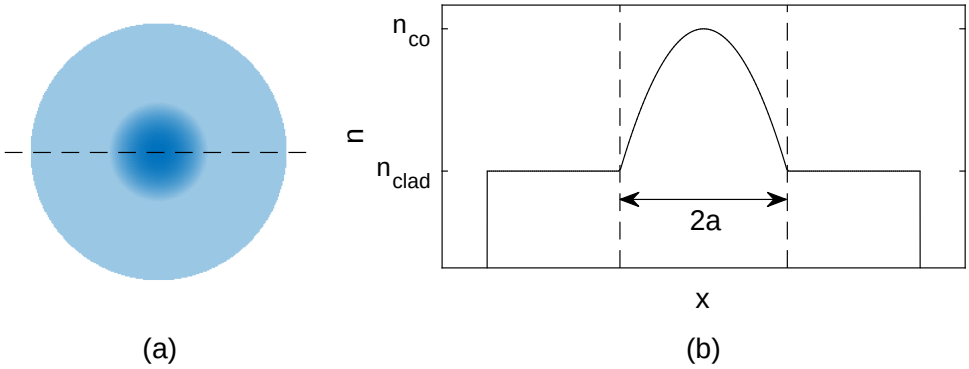

FIGURE 1.7: (a) Structure of gradient-index MMF. (b) Refractive index profile along the dashed line in (a).

For linearly polarized waves in graded-index fibers the wave equation is given by:

$$\vec{\nabla}\vec{E}(\vec{r}) + k_0^2 n(r)^2 \vec{E}(\vec{r}) = \vec{0} \tag{1.45}$$

In contrast to step-index fibers, the refractive index $n(r)$ is now dependent on the radial coordinate r. Therefore the scalar wave equation for $\psi(r, \theta)$ results in:

$$\vec{\nabla}_t^2 \psi + \left(k_0^2 n(r)^2 - \beta^2\right)\psi = \vec{0} \tag{1.46}$$

The basic wave equation for graded-index fibers in cylindrical coordinates is represented as:

$$\frac{1}{r}\frac{\partial}{\partial r}(r\frac{\partial \psi(r)}{\partial r}) + \frac{1}{r^2}\frac{\partial^2}{\partial \theta^2} + \left(k_0^2 n(r)^2 - \beta^2\right)\psi(r) = 0 \tag{1.47}$$

For the same condition presented above for step-index fibers about the invariant for a rotation of 2π, and the solutions given by Equation (1.31), the wave equation for graded-index fibers is given in term of the radial field function $\psi_l(r)$ as:

$$\frac{\partial^2 \psi_l(r)}{\partial r^2} + \frac{1}{r}\frac{\partial \psi_l(r)}{\partial r} + \underbrace{\left(k_0^2 n(r)^2 - \beta^2 - \frac{l^2}{r^2}\right)}_{k_r^2}\psi_l(r) = 0 \tag{1.48}$$

where k_r can be interpreted as wave number in radial direction.

Equation (1.48) is a second order differential equation which can be reduced to two coupled first order differential equations to be solved numerically by the Runge-Kutta method of the fourth order.

1.4.3 Mode solver

The LP modes presented by Figure 1.4 are calculated using a scalar mode solver developed by our team. The mode solver determines the guided modes of an optical waveguide using the finite difference method.

The mode solver calculate the guided modes and its corresponding effective refractive indices of the optical fiber using its optogeometric parameters (and other parameters related to guided modes and finite difference method) as inputs. The input and output arguments of the basic configuration of the mode solver function are detailed in Appendix A Table A.1.

1.5 Multi-core fibers

Multi-core fiber (MCF) is a fiber with multiple cores contained within a single cladding. The number of cores N inside cladding can be adjusted to be suited for the fiber's application.

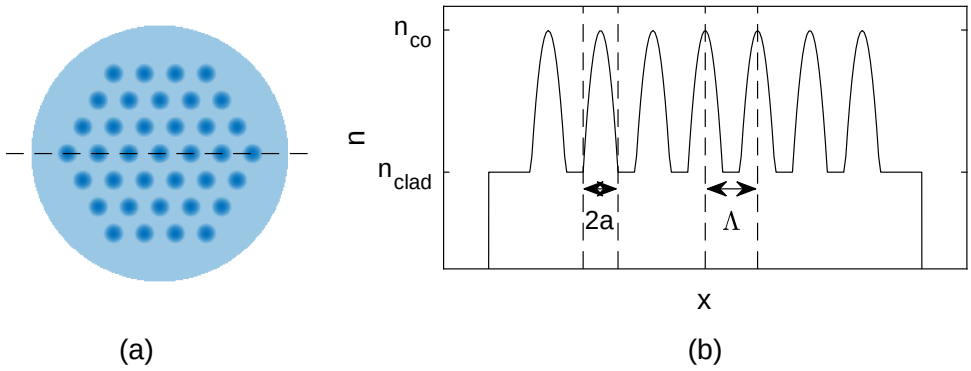

FIGURE 1.8: (a) Structure of MCF with triangular core layout.
(b) Refractive index profile along the dashed line in (a).

The optogeometric parameters of the multi-core fiber are presented by Figure 1.8. It shows a multi-core fiber with N cores arranged in a multi-ring hexagonal lattice within a fiber diameter D. a is the radius of each core, Λ is the distance between two neighboring cores, it is also called the core pitch or simply the pitch. A MCF can have any combination of pitch and core radius and refractive index step.

If we restrict ourselves to the case of the combinations that satisfy the cut-off conditions for single-mode guidance, then each core will guides only the fundamental mode, and thus we refer to it as single-mode multi-core fiber (SM-MCF). A multi-core fiber with N cores guides N polarization-degenerate modes, where each mode has two polarization directions, so the number of modes in a multi-core fiber M_{MCF} is:

$$M_{\mathrm{MCF}} = 2N \tag{1.49}$$

The mode density of a multi-core fiber is defined as the total area of the cores divided by the total area of the multi-core fiber. The mode density with pitch Λ and cores on a hexagonal lattice is then:

$$\sigma_{\mathrm{MCF}} = \frac{4}{\sqrt{3}\Lambda^2} \tag{1.50}$$

A very important characteristic in multi-core fibers is the inter-core cross-talk or simply the cross-talk. The cross-talk phenomenon is the transfer of light from one core to another during propagation through the fiber, and is a consequence of overlap between the modal evanescent fields. Therefore, cross-talk is defined as a measure of the energy exchanged among the cores of the multi-core fiber. The existence of cross-talk between cores is disadvantageous, since it leads to "scrambling" of the information transmitted through the fiber. Therefore, we aim to fibers with low cross-talk, and this can be achieved by several ways such as using heterogeneous cores in the multi-core fiber.

In an idealized multi-core fiber, where all cores are exactly the same, the group delay spread per unit fiber length equals to zero. However, real fibers experience tiny inhomogeneities between cores during fabrication process, which leads to a non-zero group delay spread. This will be discussed in detail later in section 4.4.1.

1.6 Transmission matrix

The transmission matrix (TM) of an optical fiber is defined as the linear mapping of the electric field from the input (proximal end) to the output (distal end) of an optical fiber with spatial degrees of freedom.

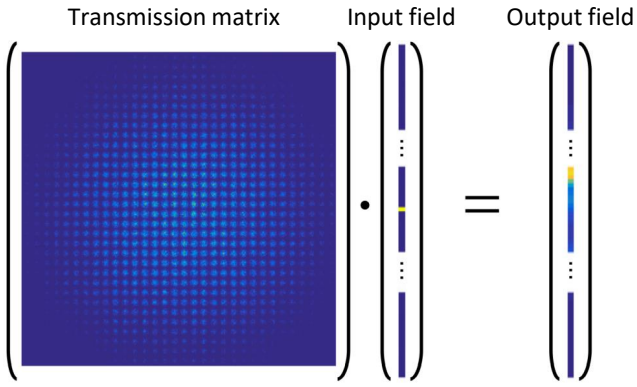

FIGURE 1.9: Visualization of the transmission matrix. The figure only shows the norm of both fields and TM.

Figure 1.9 represents a visualization of the transmission matrix. The input and output fields are expressed as 1D vector. The transmission matrix is in general complex as it is connecting the optical fields in amplitude and phase. Additionally, the transmission matrix is a unitary matrix if fiber losses are zero and if expressed in an orthogonal basis. The Transmission matrix can be expressed in several basis, such as fiber mode basis and pixel basis.

1.6.1 Mode basis

A field propagating in a waveguide can be described in terms of a sum of eigenmodes, forming a basis called "mode basis". The mode basis is composed of all the solutions to the Maxwell equations of the idealized fiber, and can be written as:

$$\{\psi_k\} \quad \text{where} \quad 1 \leq k \leq M \tag{1.51}$$

where M is the number of modes in the fiber.

Using bra-ket notation, we can define a scalar product:

$$\langle \psi | \Phi \rangle = \iint_{S_\infty} \psi^*(x,y)\Phi(x,y)\ \mathrm{d}S \tag{1.52}$$

The mode basis is orthogonal, normalized, and complete, thus:

$$\langle \psi_k | \psi'_k \rangle = \delta_{kk'} \tag{1.53}$$

$$\sum_k |\psi_k\rangle \langle \psi_k| = 1 \tag{1.54}$$

1.6.2 Pixel basis

The transmission matrix is commonly measured experimentally in the pixel basis, which is also known as a localized mode basis. The input pixel basis is defined in a plane that is at certain distance from the proximal end of the optical fiber under study, and not in the plane of the fiber end face. For example, in the plane of the spatial light modulator (SLM). In a similar way, the output pixel basis is defined in a plane that is at certain distance from the distal end of the optical fiber, and not in the plane of the fiber end face. For example, in the plane of the camera.

An overview of measuring the transmission matrix in pixel basis (localized mode basis) is as follows. One localized mode is injected into the fiber under test. Then the resulting field at the distal end is imaged onto a camera where is it mixed with a reference plane wave so as to detect the field by off-axis holography. This 2-D field rearranged into a 1-D vector and gives one line of the transmission matrix. Subsequently, the preceding steps are repeated for all localized input modes so as to construct the full transmission matrix.

We assume a one-to-one correspondence between the plane of the fiber end face and the plane defined at specific distance from fiber end for pixel basis

(either plane of SLM for input basis or plane of camera in the output basis), so the two planes can be taken to be identical.

We can define an input mode basis $\{{p_i}^{\text{prox}}\}$ and output mode basis $\{{p_j}^{\text{dist}}\}$ of localized modes as

$$\{{p_i}^{\text{prox}}\} \quad \text{where} \quad 1 \leq i \leq N_{\text{pix}}^{\text{prox}} \tag{1.55}$$

$$\{{p_j}^{\text{dist}}\} \quad \text{where} \quad 1 \leq j \leq N_{\text{pix}}^{\text{dist}} \tag{1.56}$$

Where ${p_i}^{(\text{prox})}$ and ${p_j}^{(\text{dist})}$ are associated to the i^{th} pixel and j^{th} pixel (or group of pixels, i.e. superpixel) of the SLM and camera respectively:

$${p_i}^{\text{prox}}(x,y) = \frac{1}{\Delta_{\text{SLM}}^2}\, \Pi_{\Delta_{\text{SLM}}}(x - x_i)\, \Pi_{\Delta_{\text{SLM}}}(y - y_i) \tag{1.57}$$

$${p_j}^{\text{dist}}(x,y) = \frac{1}{\Delta_{\text{cam}}^2}\, \Pi_{\Delta_{\text{cam}}}(x - x_j)\, \Pi_{\Delta_{\text{cam}}}(y - y_j) \tag{1.58}$$

where Δ_{SLM} is the pixel size on the SLM and Δ_{cam} is the pixel size on the camera. (x_i, y_i) the position of the pixel number i on the SLM with x_i and y_i being multiples of Δ_{SLM}. (x_j, y_j) the position of the pixel number j on the camera with x_j and y_j being multiples of Δ_{cam}. $\Pi_{\Delta_{\text{SLM}}}$ and $\Pi_{\Delta_{\text{cam}}}$ are a port functions defined as

$$\Pi_{\Delta_{\text{SLM,cam}}}(x,y) = \begin{cases} 1 & \text{for } |x|, |y| \leq \Delta_{\text{SLM,cam}}/2 \\ 0 & \text{otherwise} \end{cases} \tag{1.59}$$

These basis are both orthogonal and normalized

$$\langle {p_i}^{\text{prox}} | {p'_i}^{\text{prox}} \rangle = \delta_{ii'} \tag{1.60}$$

$$\langle {p_j}^{\text{dist}} | {p'_j}^{\text{dist}} \rangle = \delta_{jj'} \tag{1.61}$$

The completeness of the pixel basis depends on the size of the basis ($N_{\text{pix}}^{\text{prox}}$, $N_{\text{pix}}^{\text{dist}}$) compared to the number of modes M guided by the fiber under test. Here, by completeness we refer to the pixel basis ability to span the same mode space spanned by the fiber modes. Quite generally, if one chooses a sufficient oversampling (i.e. $N_{\text{pix}}^{\text{prox}} >> M$ and $N_{\text{pix}}^{\text{dist}} >> M$) the basis is complete:

$$\sum_{i=1}^{N_{\text{pix}}^{\text{prox}}} |{p_i}^{\text{prox}}\rangle\langle {p_i}^{\text{prox}}| = 1 \quad \text{for} \quad N_{\text{pix}}^{\text{prox}} >> M \tag{1.62}$$

$$\sum_{j=1}^{N_{\text{pix}}^{\text{dist}}} |{p_j}^{\text{dist}}\rangle\langle {p_j}^{\text{dist}}| = 1 \quad \text{for} \quad N_{\text{pix}}^{\text{dist}} >> M \tag{1.63}$$

1.6.3 Transmission matrix in mode basis

Let $\left|e^{(\text{prox})}\right\rangle$ be the electric field that enters the fiber from its proximal end, then:

$$\left|e^{(\text{prox})}\right\rangle = \sum_k |\psi_k\rangle \langle\psi_k| \, e^{(\text{prox})}\rangle \tag{1.64}$$

$\left|e^{(\text{prox})}\right\rangle$ can be written as a column vector in the mode basis:

$$\mathbf{e}^{(\text{prox,mode})} = \langle\psi_k|e^{(\text{prox})}\rangle_{1\leq k\leq M} = \begin{bmatrix} \langle\psi_1|e^{(\text{prox})}\rangle \\ \langle\psi_2|e^{(\text{prox})}\rangle \\ \vdots \\ \langle\psi_M|e^{(\text{prox})}\rangle \end{bmatrix} \tag{1.65}$$

with $\mathbf{e}^{(\text{prox,mode})} \in \mathbb{C}^{[M\times 1]}$.

After propagating in the fiber, each field accumulates a phase shift of $\exp(i\beta_k z)$, and the field going out from the distal end of the fiber is representing the propagation equation:

$$\left|e^{(\text{dist})}\right\rangle = \sum_k \exp(i\beta_k z) \, |\psi_k\rangle \langle\psi_k| \, e^{(\text{prox})}\rangle \tag{1.66}$$

$\left|e^{(\text{dist})}\right\rangle$ can be also written as a vector in the mode basis:

$$\mathbf{e}^{(\text{dist,mode})} = \exp(i\beta_k z) \langle\psi_k|e^{(\text{prox})}\rangle_{1\leq k\leq M} = \begin{bmatrix} \exp(i\beta_1 z) \langle\psi_1|e^{(\text{prox})}\rangle \\ \exp(i\beta_2 z) \langle\psi_2|e^{(\text{prox})}\rangle \\ \vdots \\ \exp(i\beta_M z) \langle\psi_M|e^{(\text{prox})}\rangle \end{bmatrix} \tag{1.67}$$

with $\mathbf{e}^{(\text{dist,mode})} \in \mathbb{C}^{[M\times 1]}$.

Thus, we can represent the propagation of fields in matricial formalism as:

$$\mathbf{e}^{(\text{dist,mode})} = \mathbf{H}^{(\text{mode})} \, \mathbf{e}^{(\text{prox,mode})} \tag{1.68}$$

Where $\mathbf{H}^{(\text{mode})}$ is the transmission matrix in input mode basis and output mode basis. $\mathbf{H}^{(\text{mode})}$ without coupling is written in the following matricial form:

$$\mathbf{H}^{(\text{mode})} = \begin{bmatrix} \exp(i\beta_1 z) & 0 & \dots & 0 \\ 0 & \exp(i\beta_2 z) & \dots & \vdots \\ \vdots & 0 & \ddots & 0 \\ 0 & \dots & 0 & \exp(i\beta_M z) \end{bmatrix} \tag{1.69}$$

with $\mathbf{H}^{(\text{mode})} \in \mathbb{C}^{[M\times M]}$.

1.6.4 Transmission matrix in pixel basis

The input electric field $\left|e^{(\text{prox})}\right\rangle$ at the proximal end of an optical fiber is written here as:

$$\left|e^{(\text{prox})}\right\rangle = \sum_i |p_i\rangle \langle p_i| \, e^{(\text{prox})}\rangle \tag{1.70}$$

which can be written as a column vector in pixel basis as:

$$\mathbf{e}^{(\text{prox,pix})} = \langle p_i|e^{(\text{prox})}\rangle_{1\leq i\leq N_{\text{pix}}^{\text{prox}}} = \begin{bmatrix} \langle p_1|e^{(\text{prox})}\rangle \\ \langle p_2|e^{(\text{prox})}\rangle \\ \vdots \\ \langle p_N|e^{(\text{prox})}\rangle \end{bmatrix} \tag{1.71}$$

with $\mathbf{e}^{(\text{prox,pix})} \in \mathbb{C}^{[N_{\text{pix}}^{\text{prox}}\times 1]}$. Similarly, the distal field represented by $\left|e^{(\text{dist})}\right\rangle is$

$$\left|e^{(\text{dist})}\right\rangle = \sum_j |p_j\rangle \langle p_j| \, e^{(\text{dist})}\rangle \tag{1.72}$$

To get the the transmission matrix in pixel basis as input and output basis, we should change the basis of the input and output fields from mode basis into pixel basis.

Basis conversion

The conversion of mode basis into pixel basis can be accomplished by the basis change operators $\langle p_i^{(\text{prox})}|\psi_k\rangle$ and $\langle p_j^{(\text{dist})}|\psi'_k\rangle$ respectively.

Thus, the input field and output field in pixel basis are written as:

$$\mathbf{e}^{(\text{prox,pix})} = \mathbf{U}^{(\text{prox})}_{(\text{mode}\to\text{pix})}\mathbf{e}^{(\text{prox,mode})} \tag{1.73}$$

$$\mathbf{e}^{(\text{dist,pix})} = \mathbf{U}^{(\text{dist})}_{(\text{mode}\to\text{pix})}\mathbf{e}^{(\text{dist,mode})} \tag{1.74}$$

where $\mathbf{U}^{(\text{prox})}_{(\text{mode}\to\text{pix})}$ and $\mathbf{U}^{(\text{dist})}_{(\text{mode}\to\text{pix})}$ are the base-change matrices converting the mode basis to pixel basis at proximal end and distal end respectively. Considering the base-change matrix applied for input field at proximal end:

$$\mathbf{U}^{(\text{prox})}_{(\text{mode}\to\text{pix})} = \begin{bmatrix} \langle p_1^{(\text{prox})}|\psi_1\rangle & \langle p_1^{(\text{prox})}|\psi_2\rangle & \cdots & \langle p_1^{(\text{prox})}|\psi_M\rangle \\ \langle p_2^{(\text{prox})}|\psi_1\rangle & \langle p_2^{(\text{prox})}|\psi_2\rangle & \cdots & \vdots \\ \vdots & \cdots & \ddots & \langle p_{N-1}^{(\text{prox})}|\psi_M\rangle \\ \langle p_N^{(\text{prox})}|\psi_1\rangle & \cdots & \langle p_N^{(\text{prox})}|\psi_{M-1}\rangle & \langle p_N^{(\text{prox})}|\psi_M\rangle \end{bmatrix} \tag{1.75}$$

with $\mathbf{U}^{(\text{prox})}_{(\text{mode}\to\text{pix})} \in \mathbb{C}^{[N_{\text{pix}}^{\text{prox}}\times M]}$.

To get the transmission matrix in pixel basis, we start from the propagation equation (Equation (1.68)) and multiply it with the base-change matrix then:

$$\mathbf{U}^{(\text{dist})}_{(\text{mode}\to\text{pix})}\ \mathbf{e}^{(\text{dist,mode})} = \mathbf{U}^{(\text{dist})}_{(\text{mode}\to\text{pix})}\ \mathbf{H}^{(\text{mode})}\ \mathbf{U}^{(\text{prox})^\dagger}_{(\text{mode}\to\text{pix})}\ \mathbf{U}^{(\text{prox})}_{(\text{mode}\to\text{pix})}\ \mathbf{e}^{(\text{prox,mode})} \tag{1.76}$$

Substituting Equations (1.73) and (1.74) we get,

$$\mathbf{e}^{(\text{dist,pix})} = \mathbf{H}^{(\text{pix})}\ \mathbf{e}^{(\text{prox,pix})} \tag{1.77}$$

Therefore, the transmission matrix $\mathbf{H}^{(\text{pix})}$ in input pixel basis and output pixel basis is

$$\mathbf{H}^{(\text{pix})} = \mathbf{U}^{(\text{dist})}_{(\text{mode}\to\text{pix})}\ \mathbf{H}^{(\text{mode})}\ \mathbf{U}^{(\text{prox})^\dagger}_{(\text{mode}\to\text{pix})} \tag{1.78}$$

where $\mathbf{H}^{(\text{pix})} \in \mathbb{C}^{[N^{\text{dist}}_{\text{pix}} \times N^{\text{prox}}_{\text{pix}}]}$.

In a similar way, we can convert the fields from pixel basis into fiber mode basis:

$$\mathbf{e}^{(\text{prox,mode})} = \mathbf{U}^{(\text{prox})}_{(\text{pix}\to\text{mode})}\ \mathbf{e}^{(\text{prox,pix})} \tag{1.79}$$

$$\mathbf{e}^{(\text{dist,mode})} = \mathbf{U}^{(\text{dist})}_{(\text{pix}\to\text{mode})}\ \mathbf{e}^{(\text{dist,pix})} \tag{1.80}$$

where $\mathbf{U}^{(\text{prox})}_{(\text{pixel}\to\text{mode})} \in \mathbb{C}^{[M \times N^{\text{prox}}_{\text{pix}}]}$, consists of the basis change operators $\langle\psi_k|p_i^{(\text{prox})}\rangle$:

$$\mathbf{U}^{(\text{prox})}_{(\text{pix}\to\text{mode})} = \begin{bmatrix} \langle\psi_1|p_1^{(\text{prox})}\rangle & \langle\psi_1|p_2^{(\text{prox})}\rangle & \dots & \langle\psi_1|p_N^{(\text{prox})}\rangle \\ \langle\psi_2|p_1^{(\text{prox})}\rangle & \langle\psi_2|p_2^{(\text{prox})}\rangle & \dots & \vdots \\ \vdots & \dots & \ddots & \langle\psi_{M-1}|p_N^{(\text{prox})}\rangle \\ \langle\psi_M|p_1^{(\text{prox})}\rangle & \dots & \langle\psi_M|p_{N-1}^{(\text{prox})}\rangle & \langle\psi_M|p_N^{(\text{prox})}\rangle \end{bmatrix} \tag{1.81}$$

$\mathbf{U}^{(\text{prox})}_{(\text{pix}\to\text{mode})}$ is a unitary matrix and so $\mathbf{U}^{(\text{prox})}_{(\text{pix}\to\text{mode})}\ \mathbf{U}^{(\text{prox})^\dagger}_{(\text{pix}\to\text{mode})} = \mathbf{I}$.

Transmission matrix with input mode basis and output pixel basis

There is no restriction on expressing and measuring the transmission matrix using the same basis at the input and output. For example, we can express the transmission matrix with input mode basis and output pixel basis, and this can be achieved by the following basis:

$$\mathbf{H}^{(\text{pix,mode})} = \mathbf{U}^{(\text{dist})^\dagger}_{(\text{mode}\to\text{pix})}\mathbf{H}^{(\text{mode})} \tag{1.82}$$

where $\mathbf{H}^{(\text{pix,mode})} \in \mathbb{C}^{[N^{\text{dist}}_{\text{pix}} \times M]}$. And thus, the output field is:

$$\mathbf{e}^{(\text{dist,pix})} = \mathbf{U}^{(\text{dist})^\dagger}_{(\text{mode}\to\text{pix})}\mathbf{H}^{(\text{mode})}\mathbf{e}^{(\text{prox,mode})} \tag{1.83}$$

1.7 Coupled mode theory

The concept of coupled modes in electromagnetism was discovered by Pierce [5] and Miller [6] in the early 1950's. The rigorous formulations of the coupled-mode equations were later established by Schelkunoff [7] and Haus [8], who used a mode expansion and a variational principle, respectively. The initial applications of the coupled mode theory (CMT) were to microwave oscillation and propagation. However, in the early 1970's CMT was introduced to guided-wave optics by Snyder[9, 10], Marcuse [11, 12], Yariv [13], and Kogelnik [14].

CMT has been successfully applied to the modeling and analysis of various guided-wave opto-electronic and fiber optical devices, such as optical directional couplers [15, 16] and optical fibers [17, 18, 19], nonparallel and tapered wave-guiding structures [20]. It has also been used to study the wave coupling phenomena in nonlinear media such as nonlinear pulse or soliton propagation [21, 22] and the modulation instability [23] in optical fibers, and nonlinear coherent couplers [24, 25]. Many of these applications are well documented and summarized in [26, 27, 28, 29].

1.7.1 Perturbation theory

The actual waveguides are very rarely ideal. Usually fabrication process induces imperfections in the waveguides in the form of refractive index inhomogeneities or slight changes in core diameters. The discrepancy between the ideal and actual waveguide model, can be accurately accounted for first-order perturbation theory. In first-order perturbation theory, the mode space spread over the modes of the fiber is assumed to be unaltered by a weak perturbation. However, a slight perturbation can have effect on the distribution of the power of modes, and thus causes an exchange of power between the modes of the fiber. Here, we assume the perturbation in the refractive index profile. This perturbation is weak, which means that refractive-index profiles of the perturbed and unperturbed fibers differ slightly, and is purely transverse, i.e., it is constant along the length of the fiber. This perturbation can be written as

$$\Delta\epsilon(x,y) = \epsilon_{\text{pert}}(x,y) - \epsilon(x,y) = n^2_{\text{pert}}(x,y) - n^2(x,y) \tag{1.84}$$

where $\epsilon_{\text{pert}(x,y)}$ and $n_{\text{pert}}(x,y)$ are the permittivity and refractive index of perturbed fiber, and $\epsilon(x,y)$ and $n(x,y)$ are those of the unperturbed fiber.

Weakly guiding perturbed fibers

For weakly guiding (perturbed and unperturbed) fibers, the variation in both profiles n and n_{pert} is small. Therefore, modal fields can be constructed from solutions of the scalar wave equations. Hence, the modal field of unperturbed and unperturbed fibers is expressed in terms of a scalar functions ψ and ψ_{pert}, and its propagation constant β and β_{pert} respectively, satisfy

$$\nabla^2\psi + (k_0 n^2(x,y) - \beta)\psi = 0 \tag{1.85}$$
$$\nabla^2\psi_{\text{pert}} + (k_0 n^2_{\text{pert}}(x,y) - \beta_{\text{pert}})\psi_{\text{pert}} = 0 \tag{1.86}$$

In order to express ψ and β in terms of ψ_{pert} and β_{pert}, we use a reciprocal relationship derived directly from Equation (1.85) and Equation (1.86), and is expressed by:

$$\beta^2_{\text{pert}} - \beta^2 = k_0^2 \cdot \int_{S_\infty} [n^2_{\text{pert}}(x,y) - n^2(x,y)]\ \psi_{\text{pert}}(x,y)\ \psi(x,y)\ \mathrm{d}S \tag{1.87}$$

where ψ and ψ_{pert} are normalized modal fields, and S_∞ is the infinite cross-section.

1.7.2 Coupled mode equations

For simplicity, we will start the analysis of coupled-mode theory in case of two identical (or almost identical) waveguides which, in isolation from one another, are single moded.

The amplitudes of modes p and q are denoted by A_p and A_q respectively. When the two waveguides are infinitely far apart, the modes do not couple however propagate independently with propagation constants β_p and β_q respectively, and their amplitudes will obey the equations

$$\frac{\mathrm{d}A_p}{\mathrm{d}z} = i\beta_p A_p \tag{1.88}$$
$$\frac{\mathrm{d}A_q}{\mathrm{d}z} = i\beta_q A_q \tag{1.89}$$

However, when waveguides are brought into close proximity, the modes will couple to each other as a result of the overlap of the evanescent fields. In this case, the spatial dependence of one mode amplitude will be modified by the existence of the other. In the case of weak coupling, the complex amplitudes of modes p and q will obey the following coupled mode equations:

$$\frac{\mathrm{d}A_p}{\mathrm{d}z} = i\beta_p A_p + i\sum_{q=1}^{N} C_{pq} A_q \tag{1.90}$$

where C_{pq} is the coupling coefficient between modes p and q and which can be obtained using coupled-mode theory [30]

$$C_{pq} = \frac{k_0}{2n_1} \int_{S_\infty} [n^2_{\text{pert}}(x,y) - n^2(x,y)]\ \psi_p\ \psi_q\ \mathrm{d}S \tag{1.91}$$

We assume that an unperturbed fiber has a refractive index $n(x, y)$ as an isolated core. And the perturbed refractive index $n_{\text{pert}}(x, y)$ is the sum of the refractive indices of cores p and q. And $n^2_{\text{pert}}(x, y) - n^2(x, y)$ is the perturbation. Therefore, as shown by Equation (1.91), the coupling between the two fibers is computed from the overlap between their fields, considering the perturbation in the index profile.

Assuming that the mode propagation equation in Equation (1.90) has the a solution of the form

$$A_p = A_{p0} \exp(i\beta_p z) \tag{1.92}$$

whereA_{p0} is slowly varying with z, we get a slowly varying function with the derivative of the perturbation function, obtaining a propagation equation in the form of an eigenvalue problem,

$$\Delta\beta A_p = \sum_q C_{pq} A_q. \tag{1.93}$$

From this eigenvalue equation we will be able to determine the eigenvalues that are represented by the difference of the perturbed and non-perturbed propagation constants $\Delta\beta$.

As we consider the coupling of a system supporting only two modes, the coupling coefficient can be represented in matricial form as

$$\mathbf{C} = \begin{bmatrix} 0 & C_{pq} \\ C_{pq} & 0 \end{bmatrix}$$

where $C_{pq} = C_{qp}$ and self-coupling C_{pp} and C_{qq} are negligible.

Power transfer and beat length

The power flow $P_p(z)$ and $P_q(z)$ in the two fibers p and q, is obtained by integrating the intensity over the infinite cross-section, and given by the following equations

$$P_p(z) = |A_p(z)|^2 \tag{1.94}$$
$$P_p(z) = |A_p(z)|^2 \tag{1.95}$$

which are related in lossless system where power is conserved by

$$P_p(z) = 1 - P_q(z) \tag{1.96}$$
$$P_q(z) = F_{pq} \sin(\beta_b z)^2 \tag{1.97}$$

where F_{pq} is the maximum power transfer from one mode to the another is defined as

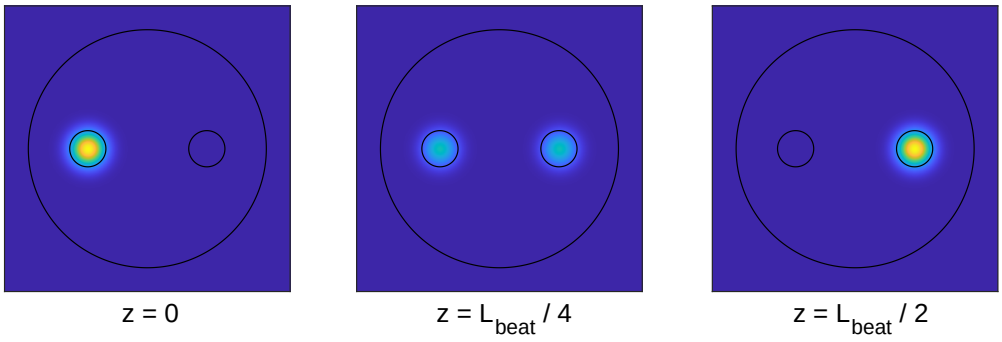

FIGURE 1.10: The mode profile of two identical fibers (a = 1.5 µm, Δn= 0.01) separated by 10 µm distance.

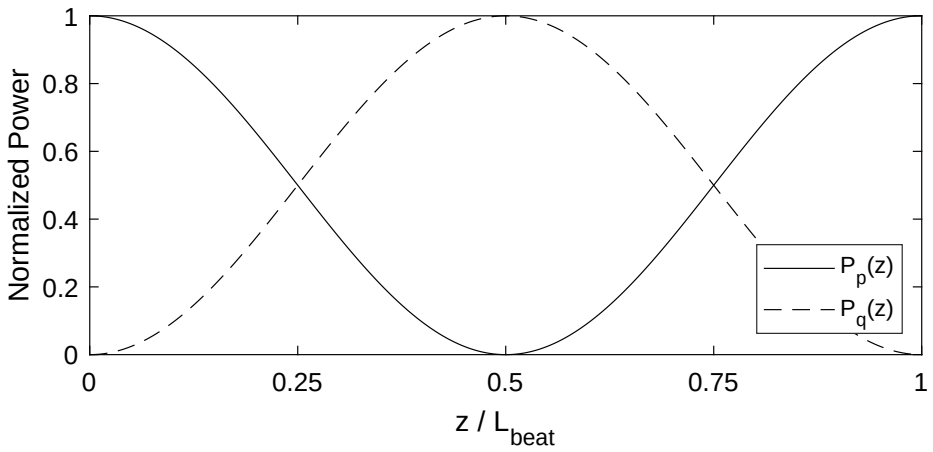

FIGURE 1.11: Power transfer between two identical fibers (a = 1.5 µm, Δn= 0.01) having equal propagation constants ($\beta_p = \beta_q$) and separated by 10 µm distance.

$$F_{pq} = \left\{1 + \left(\frac{\beta_p - \beta_q}{2|C_{pq}|}\right)^2\right\}^{-1} \tag{1.98}$$

The transfer of power is a consequence of interference, or "beating" between the perturbed eigenmodes of the two fibers, and it depends only on the difference between the scalar propagation constants.

As an intuitive example, we assume that only one of the fibers is excited with normalized power. Thus setting the initial light launching conditions to $A_p(0) = 1$ and $A_q(0) = 0$. Here we have two cases to study, which are

- For $\beta_p = \beta_q$ (degenerate modes), Figure 1.11 represents the power transfer between the two fibers along optical axis. We relate the optical axis to the beat length L_{beat} which is the distance along the waveguide in which there is total transfer of power from one fiber to the other fiber and back again. Figure 1.11 show the transfer of half the power from fiber p to fiber q at $z = L_{\text{beat}}/4$, and the total power transfer at $z = L_{\text{beat}}/2$, then the total power is transferred back to fiber p at $z = L_{\text{beat}}$. Similarly, Figure 1.10

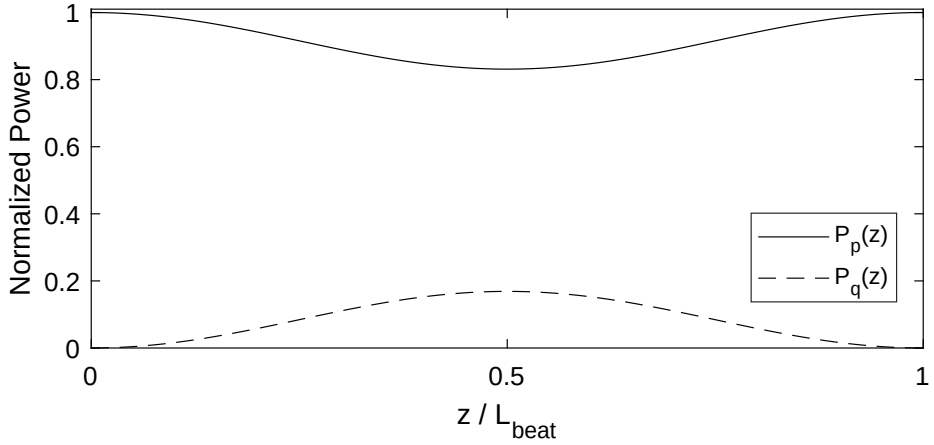

FIGURE 1.12: Power transfer between two slightly not identical fibers ($a = 1.5$ µm, $\Delta n = 0.01$) having slightly different propagation constants ($\beta_p \neq \beta_q$) where effective index difference ($\Delta n_{\text{eff}} = \frac{2\pi}{\lambda}\Delta\beta_{pq} = 4 \cdot 10^{-8}$) and separated by 10 µm distance.

represent the mode profile of the two fibers in the waveguide at different position along the optical axis.

- For $\beta_p \neq \beta_q$ (non-degenerate modes), as shown by Figure 1.12 the power transfer is not complete in this case. Only few percents of power initially launched in fiber p is transferred to the second fiber.

1.7.3 Generalisation to N modes

In the previous section, we study the coupled-mode theory in case of two coupled modes. However, in this section, we will generalize it to N modes to apply the coupled-mode theory on a uniform multi-core fiber. we start out with a multi-core fiber containing N cores arranged in a multi-ring hexagonal lattice with pitch Λ within a diameter D. We begin our analysis by assuming that each core is cylindrical with radius a, and single moded, i.e. it only supports the LP_{01} mode with a propagation constant β_0.

As we are studying the coupling between N cores in a multi-core fiber, we represent the coupling equation in matricial form. Thus the coupling coefficients matrix is:

$$\mathbf{C} = \begin{bmatrix} 0 & C_{12} & \dots & C_{1N} \\ C_{12} & 0 & \dots & C_{2N} \\ \vdots & \dots & \ddots & C_{(N-1)N} \\ C_{1N} & \dots & C_{(N-1)N} & 0 \end{bmatrix}$$

$\mathbf{C}$ is an off diagonal matrix with zeros in the diagonal and coupling coefficient between each pair of cores in the off-diagonal elements.

By diagonalizing the coupling matrix,

$$\mathbf{C} = \mathbf{V}\mathbf{B}\mathbf{V}^T \tag{1.99}$$

a new set of modes is defined which is the supermodes i.e the perturbed eigenmodes, $\mathbf{V}$, with their propagation constants $\Delta\beta^{(j)}$ given as the eigenvalues i.e. the diagonal elements of $\mathbf{B}$. The effective indices can be found as:

$$n_{\text{eff}}^{(j)} = n_{\text{eff},0} + \frac{\lambda}{2\pi}\Delta\beta^{(j)} \tag{1.100}$$

with $n_{\text{eff},0}$ the effective index of the unperturbed fundamental mode. Consequently, we are able to compute the transmission matrix $\mathbf{H}$ of the fiber in supermode basis with the element-wise exponential $\exp(i\mathbf{B}L)$ where L is the Length of the multi-core fiber. We can finally transform this supermode transmission matrix into the basis of core modes as

$$\mathbf{H} = \mathbf{V}\mathrm{e}^{i\mathbf{B}L}\mathbf{V}^T. \tag{1.101}$$

$\mathbf{H}$ is an $N \times N$ matrix i.e. expressed in the core basis which means basis of fiber modes, columns contains the modes going into the fiber and the rows contains the modes going out of the fiber. Generally speaking the modes that have close propagation constants are likely to exchange energy during propagation. Conversely, if the difference in propagation constant of modes is large, the likelihood of energy exchange is reduced. It was established that the transmission matrix of a multi-core fiber with uncoupled cores is a diagonal matrix. Inter-core coupling in multi-core fiber results in the appearance of off-diagonal elements in the transmission matrix.

Cross-talk

The principal property that can be derived from $\mathbf{H}$ alone is the cross-talk (XT). Generally, the cross-talk is defined as the relative amount of energy exchanged between cores. In our model, we would like to define the cross-talk matrix $\mathbf{X}$ as the average of the norm-square of the $\mathbf{H}$ generated with different wavelengths λ, and so the average over λ is the average over a sufficiently large number of calculated transmission matrices for different wavelengths. Consequently, we obtain a $N \times N$ "cross-talk matrix" represented by the following equation:

$$\mathbf{X} = \langle|\mathbf{H}|^2\rangle_\lambda \tag{1.102}$$

where the average, denoted by angle brackets, is done over the transmission matrices generated with different wavelength, denoted by λ in subscript.

In case of uncoupled cores, $\mathbf{X}$ is a diagonal matrix with $X_{ii} = 0$ dB. This means that beam of light injected into a single core i in the proximal end remains guided by core i during propagation. However, when inter-core coupling exist, $\mathbf{X}$ becomes an off-diagonal matrix with diagonal elements X_{ii} representing the amount of energy remaining in the excited core i, and the off-diagonal elements X_{ij} representing the amount of energy transferred from excited core i to coupling core j during propagation. Therefore, the average amount of coupling between

multi-core fiber cores is represented by the scalar "average total cross-talk" X_{ave} which is calculated, if N is sufficiently large, by the following equation:

$$X_{\text{ave}} = \frac{1}{N} \sum_i (\sum_{j \neq i} X_{ij}) \tag{1.103}$$

Distal field

The mode solver (Section 1.4.3) returns the field of the fundamental core mode vs the radial coordinate; it can be interpolated on the cartesian "distal pixel basis" $\{x_j^{(\text{dist})}, y_j^{(\text{dist})}\}, 1 \leq j \leq N_{\text{pix}}$; centering N copies on the core positions $(x_j^{(\text{co})}, y_j^{(\text{co})}), 1 \leq j \leq N$; each of these can be numerically propagated to the far-field by a two-dimensional discrete Fourier transform, the resulting fields are expressed in the (angular) "far-field pixel basis" $\{f_{x,j}^{(\text{FF})}, f_{y,j}^{(\text{FF})}\}, 1 \leq j \leq N_{\text{pix}}$; and finally re-arranged to a mode-to-far-field pixel basis change matrix $\mathbf{U}^{(\text{FF})}$ of dimensions $N \times N_{\text{pix}}$. $\mathbf{U}^{(\text{FF})}$ together with $\mathbf{H}$ permit to calculate the field in the far-field of the multi-core fiber distal end face.

$$\mathbf{e}^{(\text{FF,pix})} = \mathbf{U}^{(\text{FF})^\dagger} \mathbf{H} \mathbf{e}^{(\text{prox,mode})} \tag{1.104}$$

where $\mathbf{e}^{(\text{prox,mode})}$ is $N \times 1$ and contains elements representing the complex modal field amplitudes injected into the proximal end of the multi-core fiber.

$\mathbf{e}^{(\text{FF,pix})}$ can also be numerically propagated to any intermediate plane with an angular spectrum propagator if required. The elements of the $N \times 1$ vector $\mathbf{e}^{(\text{prox,mode},j_0)}$ are the optimal input modal amplitudes to obtain an optimal focus on far-field pixel j_0:

$$\mathbf{e}^{(\text{prox,mode},j_0)} : e_k^{(\text{prox,mode},j_0)} = (A_{jk})^*, j = j_0, 1 \leq k \leq N \tag{1.105}$$

with

$$\mathbf{A} = \mathbf{U}^{(\text{FF})^\dagger} \mathbf{H}. \tag{1.106}$$

$\mathbf{e}^{(\text{FF,pix,j}_0)}$ is the resulting complex field optimally focused on far-field pixel j_0:

$$\mathbf{e}^{(\text{FF,pix,j}_0)} = \mathbf{U}^{(\text{FF})^\dagger} \mathbf{H} \mathbf{e}^{(\text{prox,mode},j_0)}. \tag{1.107}$$

We will present in the coming chapters the use of this output focus in calculating the imaging properties of an imaging fiber.

1.8 Conclusion

This chapter provides the fundamental notions of the work presented in the next chapters of this manuscript. Starting from the simple guiding mechanism inside a conventional optical fiber, to the solutions of the wave equations evolved from the Maxwell equations. Then, we demonstrated the analysis of optical fibers based on the weakly guiding approximation, and focus on its scalar LP modes. And we present the propagation of fields in an optical fiber in matrix notation, by defining the transmission matrix. We displayed the transmission matrix in

two different basis (fiber mode basis and pixel basis), and showed the relation between the two basis. In the last section of this chapter, we demonstrated the coupled-mode theory and perturbation theory. We start by the analysis of coupled-mode theory for two coupled modes showing its coupled mode equations and its solutions. Then, we generalized the coupled-mode theory to N modes to analyze the coupling in N waveguides, and thus we were able to model a uniform multi-core fiber.

Chapter 2

Literature review: Miniaturized imaging tools

2.1 Optical fibers in imaging

Before describing the way that fiber imaging is performed through multi-core fibers, which is the major theme of the present work, it is crucial to highlight some of the fundamental concepts for the formation of an image through a linear optical system.

2.1.1 Formation of image

The performance of a linear optical system can be evaluated using Fourier optics [31]. Fourier analysis is commonly employed in signal processing for analyzing the information content of a digital signal. The fundamental notion behind Fourier analysis is that any signal may be represented as a superposition of harmonic functions that are characterized by different frequencies. The same principle applies for images, which are basically a 2D signals that can be decomposed and studied using the 2D Fourier transform [32]. The output of the transformation represents the image in the Fourier or frequency domain, while the input image is the spatial domain equivalent. In the Fourier domain image, each point represents a particular frequency contained in the spatial domain image.

The equations of plane waves propagating at different angles describe the corresponding 2D harmonic functions to which an image can be decomposed using Fourier analysis. In this case, the propagation angles are referred to as spatial frequencies. Therefore, an ideal optical system does not introduce any frequency components loss and thus forms an exact image of the object. However, due to the finite apertures of the optical systems, a limited bandwidth of frequencies can be transmitted through and contribute to the final image formation. And if the object is also described by frequencies outside this bandwidth, then final image misses this part of information and thus its quality will not be the optimal.

We consider the 4f imaging system as being a basic imaging configuration. The 4f setup is presented in Figure 2.1. The first lens (L_1) performs a physical Fourier transform of the object, and the second lens (L_2) performs the inverse Fourier transform, which reconstitutes the image of the object. In the image

plane, the 2D complex amplitude distribution of the image is represented by $A(x, y)$. The intermediate plane is the Fourier plane.

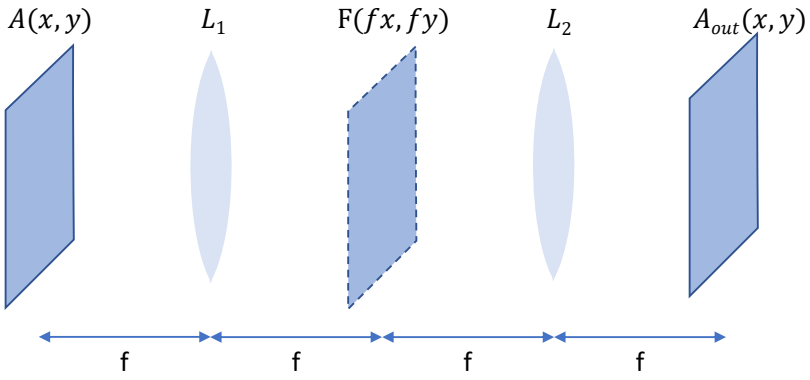

FIGURE 2.1: Scheme of 4f configuration setup.

The Fourier Transform (FT) of the image $A(x, y)$ is performed by lens L_1 is given by the following equation

$$\mathcal{F}\{A(x,y)\} = F(f_x, f_y) = \int_{-\infty}^{+\infty}\int_{-\infty}^{+\infty} A(x,y)e^{-j2\pi(f_x x + f_y y)}\,\mathrm{d}x\,\mathrm{d}y \qquad (2.1)$$

where the Fourier coordinates (f_x, f_y) have units of inverse length and are called spatial frequencies. Note that, in the Fourier plane the spatial frequency (f_x, f_y) is located at the point $(\lambda f f_x, \lambda f f_y)$. Then, the spatial distribution in the Fourier plane is $F(\frac{x}{\lambda f}, \frac{y}{\lambda f})$.

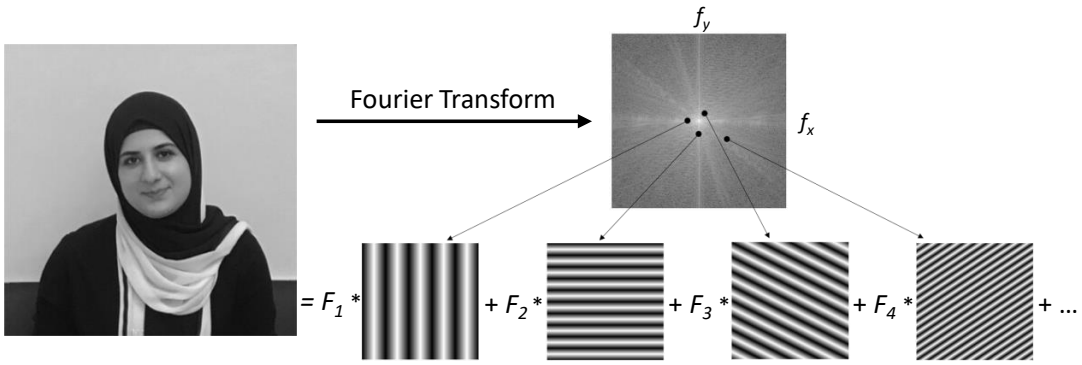

FIGURE 2.2: Optical Fourier transform of a complex image analyzed as sum of harmonic functions of different spatial frequencies and complex amplitudes.

The Fourier transform gives information about the frequency content of the image. Figure 2.2 shows an image of "Me" and its 2D Fourier transform. The norm-square of the amplitude of Fourier image represents the distribution of energy in the frequency plane. The lower line in Figure 2.2 shows how the image is a superposition of spatial frequencies with varying orientations, and each one with a particular amplitude (F_1, F_2, F_3, F_4, ...). By selecting several

frequencies in the Fourier domain (f_x, f_y) (the dots in Figure 2.2) and setting the rest to zero each time, and then performing inverse Fourier transform (IFT) through lens L_2 by the following equation

$$\mathcal{F}^{-1}\{F(f_x, f_y)\} = A_{out}(x, y) = \int_{-\infty}^{+\infty} \int_{-\infty}^{+\infty} F(f_x, f_y) e^{j2\pi(f_x x + f_y y)}\, df_x\, df_y \quad (2.2)$$

we get a field with a phase linear in the spatial domain (x, y). These fields correspond to plane waves propagating at certain angles. Therefore, it can be seen how an image is a superposition of 2D harmonic functions that correspond to a plane waves.

In the Fourier image (Figure 2.3(a) (right)), the low frequency information are located near the center of the image while the high frequencies near the edges. In the image (Figure 2.3(a)(left)), the gray background behind "Me" is a low frequency area, because the intensities of the pixels slowly evolve from one pixel to another. On the contrary, my features and cloth are a high frequency area because the pixel intensity shows a rapid alternation between them and the background.

Spatial filtering

By making a Fourier transform of an image using a lens, it is possible to alter the image content by placing filters (masks) in the Fourier plane for selectively removing certain spatial frequencies. Therefore, this process is called spatial filtering. One kind of filter is the low pass filter. It allows low spatial frequencies to pass through the system while blocking components associated with higher spatial frequencies. This filter can be applied by a finite aperture in Fourier space (Figure 2.3(b)left). High frequency components are necessary to convey sharpness. Therefore, zeroing the high frequency components in the Fourier image and performing an inverse Fourier transform will result in a loss of resolution and generate a blurred image Figure 2.3(b)right.

Another kind of filter is the high pass filter. A high pass filter consists of a dark spot in the center of the Fourier plane (Figure 2.3(c)(left)). Thus, it tends to retain the high frequency components within an image which correspond to its finest details (small features) in the real space, while reducing the low frequency components. Consequently, it emphasize fine details in the image (Figure 2.3(c)(right)).

Based on the above brief Fourier analysis, it is obvious that to obtain an image correctly propagated through an optical system we should be able to preserve all of the spatial frequencies that make up the image. However, due to the non-ideal nature of the optical system, losses in the spatial frequency transmission of an image can be induced, resulting in "band-passing" of the frequency spectrum of the recorded object leading to degradation in the final image.

The numerical aperture of lens L_1 is a measure of its ability to gather light from object and is equals to

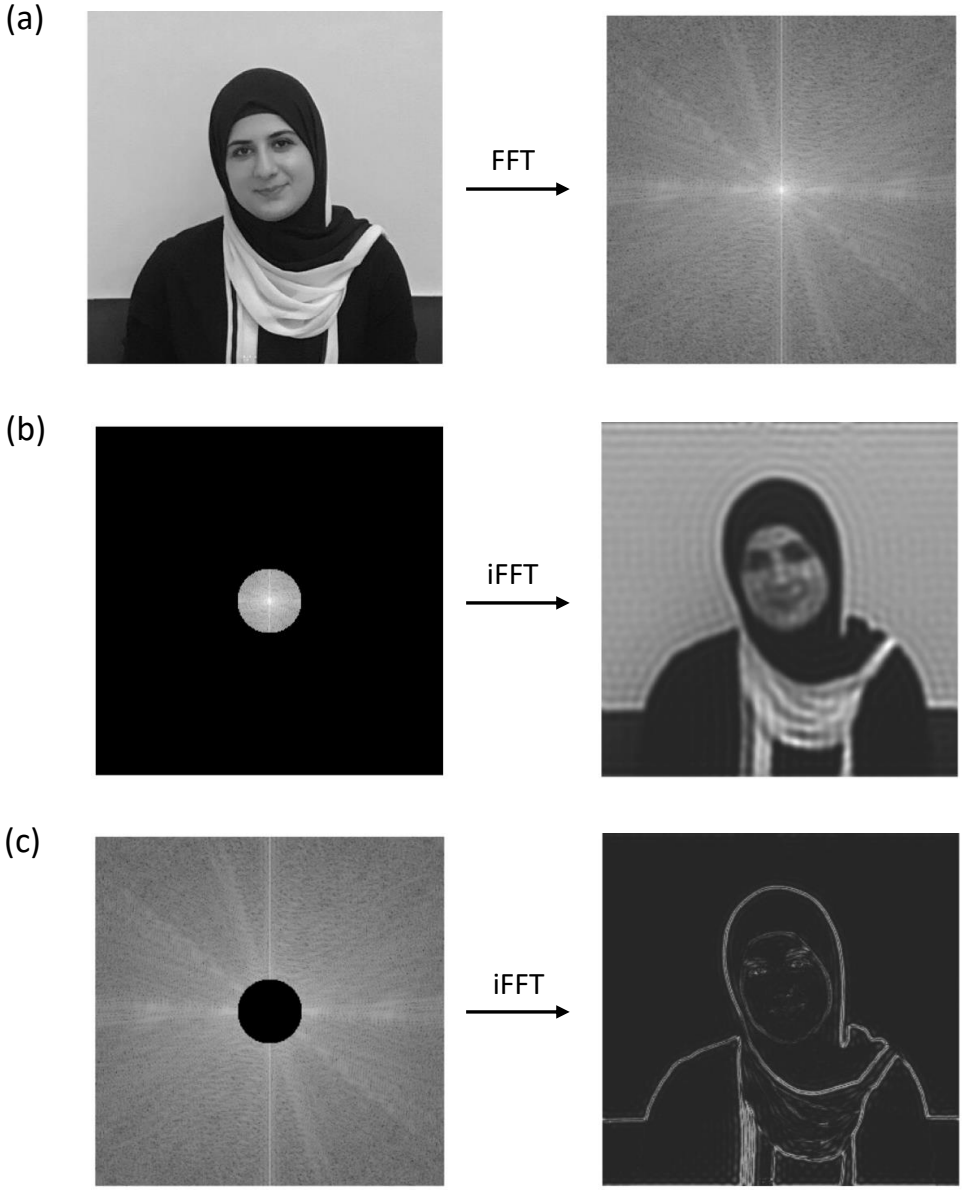

FIGURE 2.3: Optical Fourier transform of a complex image. (a) A photograph is subjected to a fast Fourier transform (FFT).(b) Image result when limiting high frequency components, (c) Image result when preserving high frequency components but zeroing low frequency components of the Fourier image.

$$NA = n_0 \sin\theta_{\max} = \sin\theta_{\max} \tag{2.3}$$

where $n_0 = 1$ is the refractive index of air (medium between object and lens) and $\theta_{\max}$ is the maximal half-angle of the cone of light that can be accepted by the lens.

Then radius of the aperture in Fourier space which is denoted as the maximum observable spatial frequency $f_{x,\max}$, is related to the numerical aperture NA and illumination wavelength λ by

$$f_{x,\max} = \frac{NA}{\lambda} \tag{2.4}$$

Therefore, as the fine details of an image are encoded on the edges of the Fourier image, a larger aperture in Fourier space and so using a lens with high numerical aperture, results in the conservation of more high frequency information.

Resolution

Indeed, every imaging system has a specific NA that allows only a portion of the spatial frequencies to pass through. And as shown in Figure 2.3(b), it is clear that the resolution of the image is lower and blurring of the image is induced by cutting off part of its high-frequency components, which represent the same concept of propagating the image through a system that limits its spatial frequency content. Consequently, it is evident that the NA of an imaging system is a crucial parameter for the final resolution. And based on Abbe's criterion, the lateral resolution (i.e, the resolution in the plane of focus (x,y)) and axial resolution (i.e, the resolution along the optical axis of the microscope (z-axis)) of imagining system can be determined by the following formulas respectively:

$$\text{resolution}_{\text{lateral}} = \frac{\lambda}{2\ NA} \tag{2.5}$$

$$\text{resolution}_{\text{axial}} = \frac{2\lambda}{NA^2} \tag{2.6}$$

Spatial light modulator

Spatial light modulator (SLM) is a wavefront shaper that can be located in the Fourier plane of a 4f-setup as an arbitrary amplitude and/or phase mask. Placing an SLM in the Fourier plane gives a direct access to the spatial frequencies, and thus act as spatial Fourier filters in the imaging path. In this case, SLM can influence the image contrast by manipulating the Fourier components of the light coming from the sample.

Figure 2.4 presents the conceptually simplest case, assuming a transmissive SLM at the center of the $4f$ setup. However, in practice a reflective SLM is often used, due to its better light efficiency. In this case the incident light beam is imaged by an additional relay system (typically a telescope) at the SLM surface, which then imprints the displayed phase onto the image wave and reflects it to the imaging system (Figure 2.5). Furthermore, a blazed grating can be added to

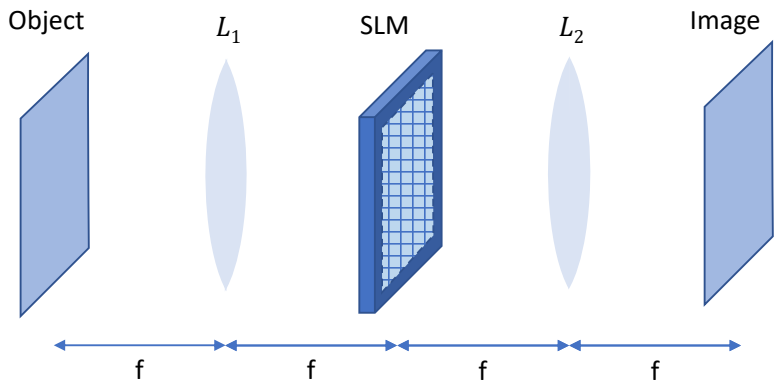

FIGURE 2.4: Schematic setup of Fourier filtering with a trans missive SLM.

the phase mask on the SLM, resulting in the so-called off-axis configuration. The blazed grating diffracts the incoming wave to the image plane. Normally only the first order diffracted light is used for imaging, whereas the other diffraction orders of the SLM are blocked. This typically leads to a better control of both the spatial phase and amplitude modulation of the diffracted beam.

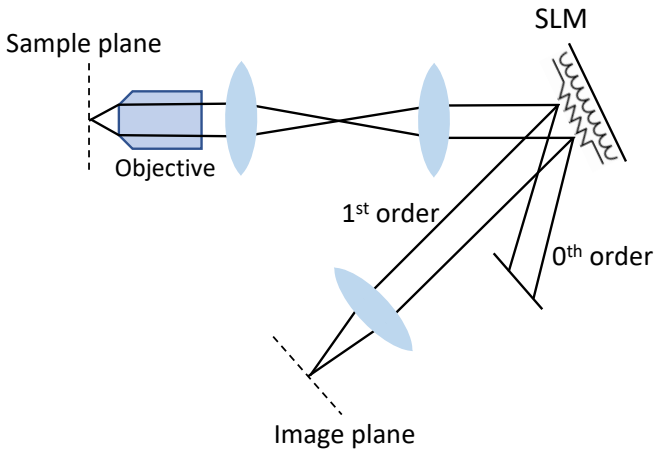

FIGURE 2.5: Schematic setup of Fourier filtering with a reflective SLM.

Liquid-crystal spatial light modulator is a beam shaping device which is used for a large panel of applications. Spatial light modulator is composed of mask with a few hundred thousand to a few million individually addressable pixels. This large number of pixels thus gives the capacity to perform extremely fine modifications of the wavefront which can reach very high spatial frequencies. The most common popular type of two-dimensional liquid crystal spatial light modulators are phase-only devices [33]

Spatial light modulator has some disadvantages, such as the need to calibrate the device for each wavelength used. Another disadvantage associated with this technology lies in the low refresh rate of these systems, i.e. the number of independent phase masks that can be displayed per second of liquid-crystal spatial light modulators to 10-200 Hz. This low activation speed represents a

real limitation for applications requiring rapid modifications of the wavefront, such as in scanning microscopy.

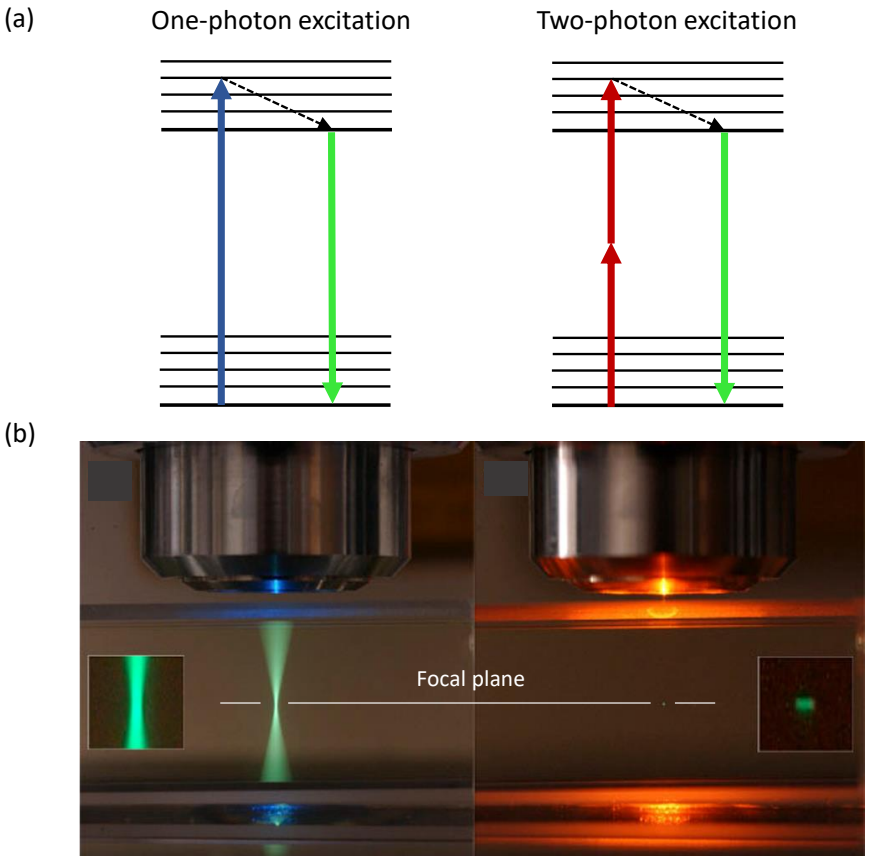

FIGURE 2.6: (a) Comparison of one-photon and two-photon absorption process. (b) Comparison of one-photon vs two-photon fluorophore excitation (magnification in the insets) [Image by Steven E. Ruzin and Holly Aaron at University of California at Berkeley].

2.1.2 Wide-field imaging

Wide-field microscopy is a basic fluorescence microscope that is commonly used to image specific features of specimens under study [34]. The underlying key principle is the use of fluorescent molecules —the so-called fluorophores— for the labeling of defined cellular structures. Then these fluorescent molecules, such as green fluorescent protein (GFP), absorb light at a certain wavelength (excitation) and emit light at a certain higher wavelength (emission), this process is known as one-photon fluorescence excitation (Figure 2.6(a)(left)).

The basic concept of Wide-field microscopy is illustrated in Figure 2.7. The light source falls into excitation filter which only transmits the light of a particular wavelength that can excite the fluorescent molecules tagging the specimen. The excitation light will then fall onto the dichroic mirror which reflects this excitation light (blue) towards the objective lens and then onto the specimen.

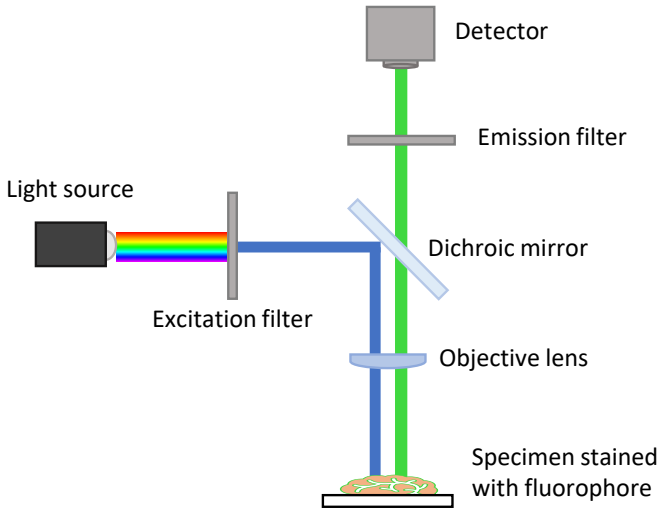

FIGURE 2.7: scheme of wide-field microscope setup.

The whole specimen is exposed to the light, and as it is stained with a fluorescent dye, the fluorescent molecules absorb photons from the "excitation" light and emits a fluorescent light (green) with longer wavelength compared to the corresponding excitation light. The emitted fluorescent light will then be transmitted through the dichroic mirror towards the emission filter which allows only the emitted fluorescent signal with green wavelength to pass through which is then detected by the detector (CCD camera). Indeed, fluorescent labels attached to the structures of interest will be visible as bright point emitters against a dark background, drastically improving contrast.

In wide-field microscopy, the fluorescence signals from all focal planes are detected , which leads to low contrast in thick samples like spheroids and tissue. Therefore, wide-field microscopy is best applied with thin specimens with low background auto-fluorescence, like adherent cells. The wide-field illumination not only focus information from the corresponding section of the specimen but also allows out-of-focus light to arrive camera, leading to low contrast and spatial resolution

2.1.3 Confocal imaging

Confocal microscopy [35] is an important innovation in fluorescence microscopy which aims to overcome some limitations of wide-field fluorescence microscopes. Confocal microscopy has the ability to increase optical resolution and contrast of an image by means of using a spatial pinhole to block out-of-focus light in image formation and therefore brings in the concept of point-by-point scanning of the specimen [36].

Confocal microscopy, as wide-field microscopy, is a one-photon fluorescence excitation microscopy. Since one-photon fluorescence excitation is a linear mechanism, the signal has linear dependence on the excitation light intensity (Signal $\propto I$). Therefore, absorption occurs within the entire excitation light cone and

so fluorescence green emission is observed along the full length of the beam path as shown in Figure 2.6(b)(left).

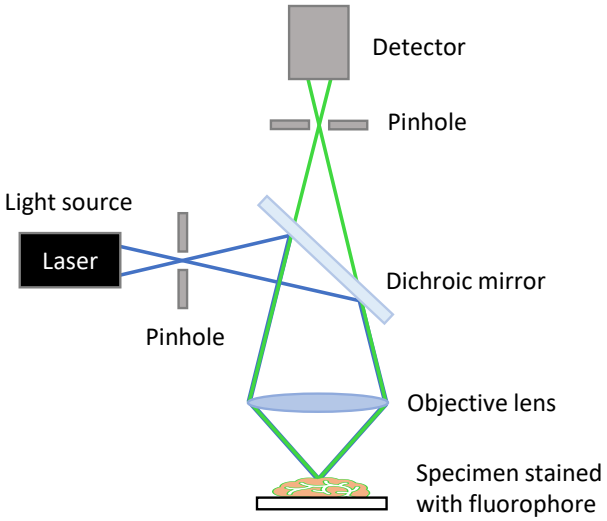

FIGURE 2.8: scheme of Confocal microscope setup.

The confocal principle in epi-fluorescence laser scanning microscopy is presented in Figure 2.8. The laser beam is focused onto a defined spot at a specific depth within the specimen by passing through a pinhole placed in front the excitation source. The focused point is defined by the size of the pinhole aperture. The focused laser beam is reflected by a dichromatic mirror and scanned across the specimen, as function of mirror angle, in a defined focal plane. Then the fluorescent light emitted from focused points on the specimen pass back through the dichromatic mirror and are focused as a confocal point at second pinhole aperture. The second pinhole is placed in an optically conjugate plane in front of the detector to eliminate the out-of-focus signals. Thus only fluorescence generated from focal plane is collected by a light sensitive point detector such as a photo-multiplier tube (PMT). The PMT converts the incident photons into an electrical signal then a computer collects the detector signal through-out the scanning procedure and digitally reconstructs an image from the recorded information. Confocal laser scanning microscopes can use x-y scanning mirrors to scan the laser across the sample and descan the image across a fixed pinhole and detector, or by moving the specimen over short distances in a raster pattern.

Thanks to pinhole, confocal microscopy can provides more resolution in depth (axial resolution) than conventional wide-field microscopy. And the selection of optimum pinhole size is essential, as the size of the pinhole will dictate the intensity (brightness) and thickness of the slice observed [37].

2.1.4 Point-scanning imaging

Point-scanning imaging is typically done with two-photon excitation fluorescence microscopy. Two-photon excited fluorescence laser-scanning microscopy [38], combined with in-vivo fluorescence labeling techniques, has opened a rapidly

expanding field of imaging studies in intact tissues and living animals. In particular, its capability of optical sectioning, allowing to produce 3-dimensional images of the sample.

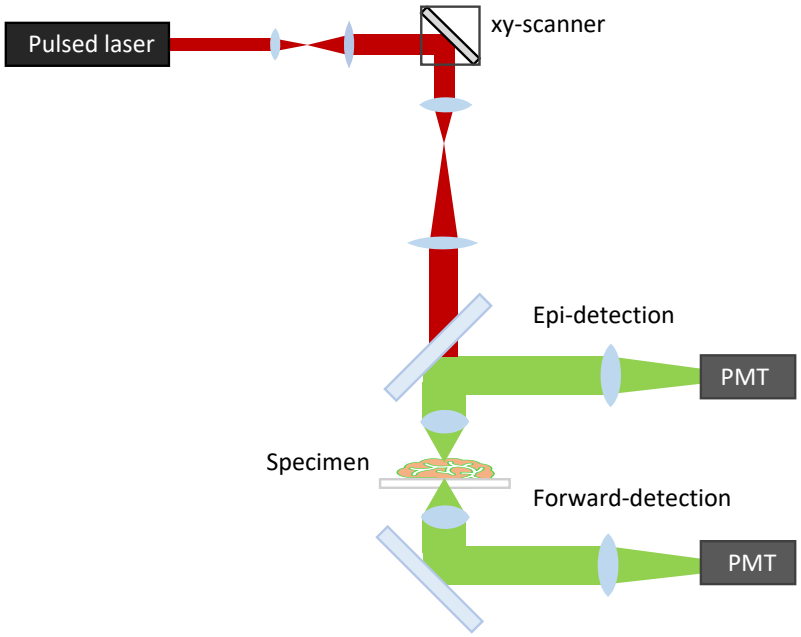

FIGURE 2.9: Scheme of point-scanning imaging setup.

In two-photon excitation microscopy the fluorophore is excited by absorbing simultaneously two photons of a long wavelength (near-infrared spectral range) which results in the emission of fluorescence photon with a shorter wavelength (visible spectral range) (Figure 2.6(a)(right)). To generate sufficient signal, excitation light has to be concentrated in space and time. High spatial densities are generated by focusing a laser beam through a high numerical aperture (NA) objective. And concentration in the time domain requires the use of lasers that emit ultrashort pulses (hundreds femtoseconds long) with correspondingly high peak intensities.

Two-photon absorption is a nonlinear contrast mechanisms, thus the signal has quadratic dependence on the density of photons, i.e, the excitation light intensity (Signal $\propto I^2$). As a consequence, two-photon fluorescence excitation occurs only in a tiny diffraction-limited focal volume (Figure 2.6(b) right). Localization of excitation provides excitation based three-dimensional resolution with no need for spatial filters in the detection path, for example, the detector pinhole in the confocal microscope (as shown in section 2.1.3). This enhances the collection efficiency and increases penetration depth (up to 1 mm depths [39]). Then the lack of out-of focus excitation reduces photo-damage [40] and thus increases tissue viability, which is crucial for long-term imaging [41] . Moreover, exciting tissue with lower energy photons (long wavelengths) results in substantially less phototoxicity, photobleaching [42], and scattering.

Figure 2.9 presents a generic point-scanning microscope. A laser source provides near-infrared ultrashort pulses. Two-photon excited fluorescence (TPEF),

can be collected in epi-collection and/or forward-collection mode, using detection by photo-multiplier tubes (PMTs). To generate an image, the laser is raster-scanned across the specimen using xy-scanner. And since the excitation occurs only in the focal volume, all fluorescence photons captured by the microscope objective constitute useful signal.

Point-spread function

In scanning microscopy, the spatial resolution of the optical system can be equated to the point-spread function (PSF). We can define the point-spread function here as the image obtained by scanning a very small object that is a Dirac δ-function. Thus PSF is the image of a focused point source. Consequently, the resolution of such a system is defined by the size of the PSF.

Indeed, the image of a fluorescent object through a microscope objective corresponds to the convolution of the object with the point-spread function. The image intensity distribution $I(x, y)$ of an object $O(x, y)$ is then given by the relation:

$$I(x, y) = O(x, y) * PSF(x, y) \tag{2.7}$$

where $*$ corresponds to the convolution operation.

2.1.5 Fiber imaging

The concept of fiber optic imaging uses the optical transmission properties of fiber to transmit an image from end to end. In this section, we will present the imaging analysis in multi-mode fibers and multi-core fibers as being the most widely useful fibers for imaging.

Lens-less multi-mode fiber imaging

In multi-mode fibers, the image is not simply transferred along the fiber length. However, the input image distributes among the supported spatial modes in the optical fiber. The coupling of the image with fiber modes is determined by the overlap integral between the image and the modes fields. At the proximal end of the multi-mode fiber, where $z = 0$, then the expansion coefficients of an input image $A(x, y)$ to the fiber mode p with field E_p can be calculated as:

$$c_p(z = 0) = \int_{-\infty}^{\infty} \int_{-\infty}^{\infty} A(x, y)\ E_p^*(x, y)\, \mathrm{d}x\, \mathrm{d}y \tag{2.8}$$

Then, the image at a distance z along the fiber will be given as a linear combination of the supported fiber modes. The image $I(x, y)$ at a point z along the fiber is:

$$A_z(x, y) = \sum_p c_p(z = 0)\ E_p^*(x, y)\ e^{-i\beta_p z} \tag{2.9}$$

As each mode has a unique propagation constant, the modes in a multi-mode fiber accumulate phase at different rates. Therefore, the local information of the input beam of light decorrelate after few hundreds of micrometers after propagation in the multi-mode fiber, forming at the distal end of the fiber a structured pattern that has a random intensity distribution. This structured pattern is called speckle and is resulted from the interference between the fiber modes emerging from the distal end of the multi-mode fiber. Therefore, this shows how a multi-mode fiber completely scrambles the input image. In spite of that, multi-mode fibers are linear optical systems and the coupled information is not lost along propagation, and in fact the fine structure of this speckle contains all the information about the image. Then the image can be reconstructed if one has sufficient knowledge about the propagation of light through the multi-mode fiber.

Several optical techniques have been proposed to reconstruct the information through multi-mode fibers. Such as transmission matrix approach which was first explored by Popoff et al. [43] and phase conjugation approach [44]. These methods are based on detecting the output field by off-axis holography [45], and so recover the phase and amplitude of the field aiming to calculate the required wavefront to control the light through the multi-mode fiber.

To clarify, we will present how image can be reconstructed from the transmission matrix in wide-field multi-mode fiber lens-less endoscope and in point-scanning multi-mode fiber lens-less endoscope.

Wide-field multi-mode fiber lens-less endoscope

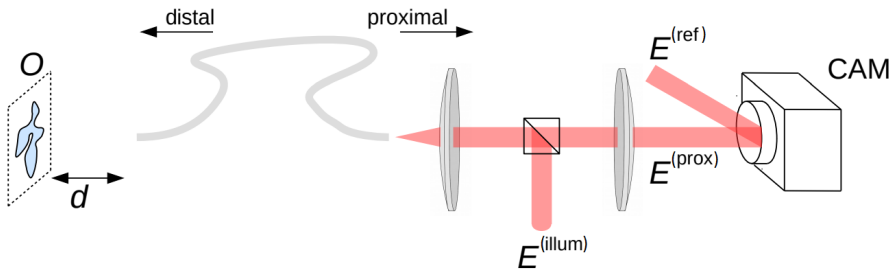

FIGURE 2.10: Sketch of an experimental realization of a wide-field MMF lens-less endoscope.

Figure 2.10 represents a scheme of the experimental realization of a wide-field lens-less endoscope. A coherent light source is injected into the multi-mode fiber at the proximal end (represented by field $E^{(\mathrm{illum})}$), is transmitted through the fiber to illuminate the object O at the distal end, and relayed back through the multi-mode fiber (represented by field $E^{(\mathrm{prox})}$) and detected on the proximal end through an off-axis holography by mixing with reference beam (represented by field $E^{(\mathrm{ref})}$) on the image sensor CAM. Then the image of the object can be found by numerically multiplying the detected field by the inverse of the pre-measured transmission matrix.

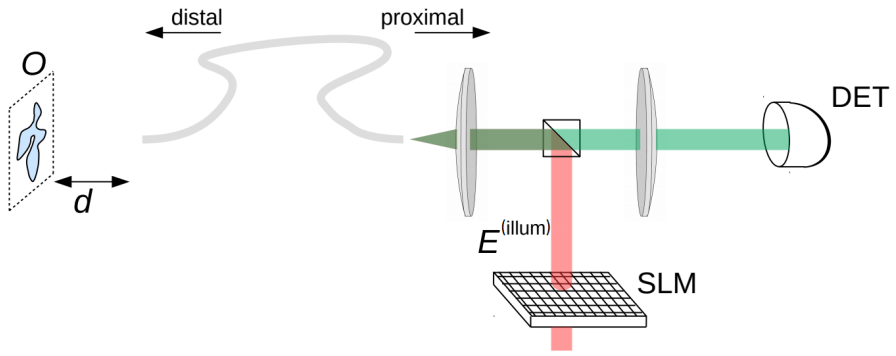

FIGURE 2.11: Sketch of an experimental realization of a point-scanning MMF lens-less endoscope.

Point-scanning multi-mode fiber lens-less endoscope

The lens-less endoscope is most commonly implemented with image acquisition by point-scanning, since in biological imaging we almost always have fluorescent samples.

Point-scanning imaging actually amounts (approximately) to physical inversion of the transmission matrix by using a wavefront shaper, typically a spatial light modulator. The idea is to illuminate the object sequentially by maximally focused distal illumination fields. Figure 2.11 represents a scheme of the experimental realization of a point-scanning lens-less endoscope. As a preliminary step, the transmission matrix of the fiber is measured in pixel basis (cf Section 1.6.4). The lines of the transmission matrix are identified as the input fields that give rise to focused output fields. The phase masks that convert the laser beam into said input fields are calculated. Then these phase masks are displayed sequentially on a spatial light modulator (SLM) resulting in a two-dimensional scan of the output focus across the object (O). Then fluorescence signal generated from each focused point on the object, is collected by the fiber and transported back to the proximal end where it is filtered and detected by a single point detector (DET) as in a point-scanning microscope (cf Section 2.1.4).

The quality of image using multi-mode fiber endoscope is mainly defined by two parameters. The numerical aperture (NA) of the fiber which depends only on the refractive index difference between core and cladding (Equation (1.4)) and thus it can be properly tuned to improve the resolution while maintaining the size of the fiber core constant. And the number of spatial modes supported by the multi-mode fiber is an important parameter for the quality of the formed image. Since the fiber modes can be seen as the available degrees of freedom of the system that will contribute to the image formation [46, 47, 48].

Multi-core fiber imaging

Multi-core fibers can directly transfer the image of an object illuminated with an incoherent light source without further processing. The cores of multi-core fibers are often designed to support a single mode, and the location of each core remains the same along the fibre. Then each core carries one pixel, which is a picture element that has to remain at the same location within the image, and

delivers it to the far end of the fiber, thus fiber bundle transmits a pixelated image composed of an array of light intensities (as shown by Figure 2.12). Imaging in this way is performed only if the object is positioned immediately adjacent to the multi-core fiber facet. Describing this image formation by Fourier optics (2.1.1), the multi-core fiber (or fiber bundle) is represented as a mask with apertures at the positions of the cores with the plane of object, and thus the image of the object will be kind of masked (or pixelated) by the bundle of cores.

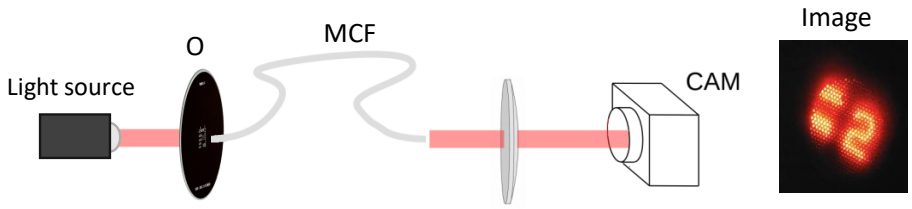

FIGURE 2.12: Sketch of an experimental realization of imaging with MCF as image relay.

Therefore, multi-core fiber should carry large number of cores to be able to obtain large number of independent pixels in the image. And the resolution of images using multi-core fiber is defined by core spacing, or what we call the core pitch, so image resolution can be enhanced using a multi-core fiber with a small core spacing or dense cores. However, reduction of the core spacing may increase cross-talk between cores, which if exist causes image blurring. Even so, cross-talk between cores can be reduced by having heterogeneous cores. Moreover, enhancing imaging resolution can be achieved by magnifying the object on the fiber facet by means of lenses attached to the fiber end. But this ultimately leads to a decrease in the field of view of the imaging fiber, and increases the size of the imaging probe.

Lens-less multi-core fiber imaging

Knowing the transmission matrix of the multi-core fiber, we are able to do endoscopic point-scanning imaging [49, 50]. This method is another way to improve the resolution of the multi-core fiber imaging system without increasing the size of imaging probe by any element attached to the fiber tip. The point-scanning multi-core fiber lens-less endoscope works in the same way as described in Section 2.1.5. Here, the resolution will be defined by the numerical aperture of each individual core in the multi-core fiber.

2.2 Literature review

2.2.1 Video endoscope

In recent years numerous efforts have been made to miniaturize imaging instruments. A recent example that has been already commercialized by the

neurotechnology company Inscopix is the head-mounted miniaturized microscope for fluorescence imaging [51, 52]. This approach uses the concepts of wide-field imaging presented in Section 2.1.2, and has all optical and opto-electronic elements integrated into a small lightweight (2 g) device that is easily head-mounted and carried by mice (Figure 2.13).

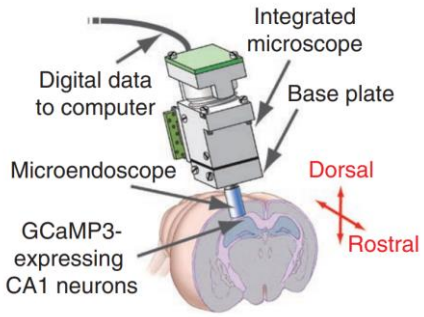

FIGURE 2.13: Head-mounted video endoscope [51].

2.2.2 Lens-less fiber endoscopes

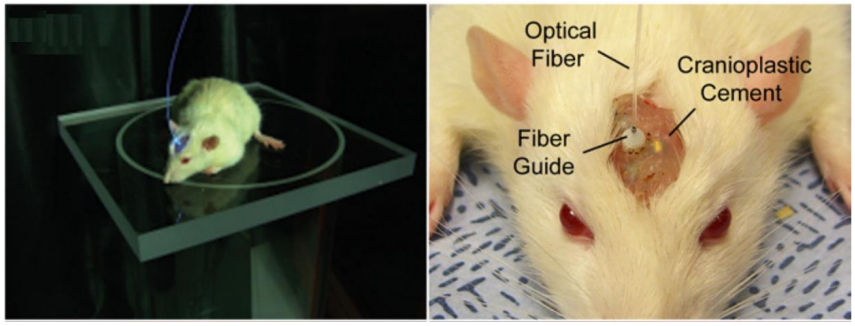

FIGURE 2.14: Optical neural interface [53].

For deep brain structures and for awake behaving animals the miniaturized microscopes (cf Section 2.2.1) are still too bulky and not suitable. Therefore, we will present the work of Ref. [53] from 2007 as an example to overcome these challenges. The authors in this paper developed an optical neural interface consisted of an optical fiber guide stereotaxically mounted on the skull with an optical fiber inserted through the guide (Figure 2.14). The fiber used in this paper was a 200 µm multi-mode fiber with a numerical aperture of 0.37. The objective of their work was just to transport light to a certain brain region, specifically to the vibrissal motor cortex and functionally activate ChR2 in an intact animal. So in this paper, the authors show how to fix a multi-mode fiber into an intact mouse allowing it to move freely, and deliver light by the multi-mode fiber to a specific brain region about a cubic millimeter in volume. However, if we can also control the light going out from this multi-mode fiber by wave front shaping at the proximal side (farthest from the sample), we could be able to make an imaging device based on optical fibers without any elements attached to its distal end, thus we refer to it as lens-less endoscope.

The first demonstrations of microscopic imaging of objects through multi-mode fiber which did not require any elements between the fiber and the object were published in 2011 [54, 55, 44, 56]. We will present in the coming sections the state-of-the-art of lens-less endoscopes based on multi-mode fibers and multi-core fibers and applied with different types of microscopic imaging.

2.2.3 Wide-field imaging endoscopes

Imaging fiber bundle

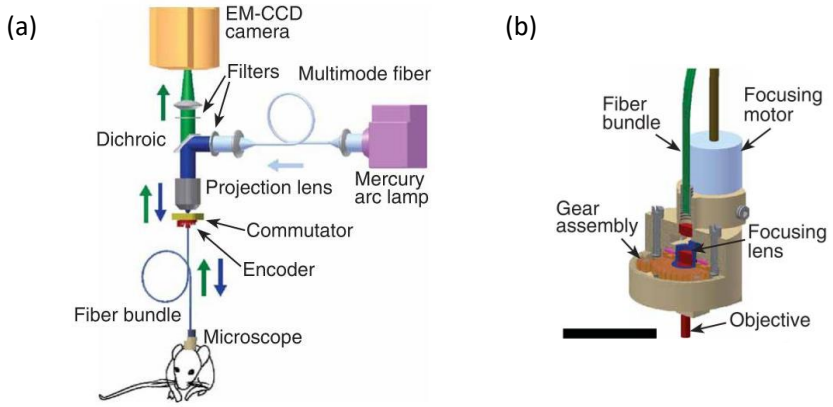

FIGURE 2.15: Miniaturized fluorescence microscopy [57] (a) Imaging setup and (b) scheme of the microscope. Scale bar, 1cm.

In 2008, Flusberg et al. demonstrated a miniaturized (1.1 g mass) epifluorescence microscope based on fiber bundle (⌀ 240–370 mm) and micro-optics (Figure 2.15) for cellular-level brain imaging in freely moving mice [57]. The fiber bundle in this microscope rotates freely within a commutator to reduce torsional strain as the mouse moves. This microscope used the concept of wide-field imaging (cf Section 2.1.2) and was able to perform high-speed cellular imaging ($\leq$ 100 Hz) with broad field of view in a freely behaving mice.

Multi-mode fiber wide-field imaging endoscopes

In 2012, Choi et al. demonstrated the first wide-field endoscopic imaging (cf Section 2.1.2) by using a single multi-mode fiber at a relatively high speed imaging (1 frame/s for 3D imaging) with a high spatial resolution (1.8 µm) [56]. The authors of this paper converted a 1 meter-long multi-mode fiber into a self-contained 3D imaging device that doesn't require a scanner or a lens. Thus the diameter of the endoscope is the diameter of the single fiber itself (⌀230 µm). They used a pre-measured transmission matrix of the multi-mode optical fiber to reconstruct an object image at the object plane from a distorted image recorded at the image plane by off-axis digital holography (Figure 2.16). Then employed the speckle imaging method [58] to eliminate the distortion of input illuminating light, and acquire a clean object image by averaging sufficient numbers of images recorded at different speckle illuminations.

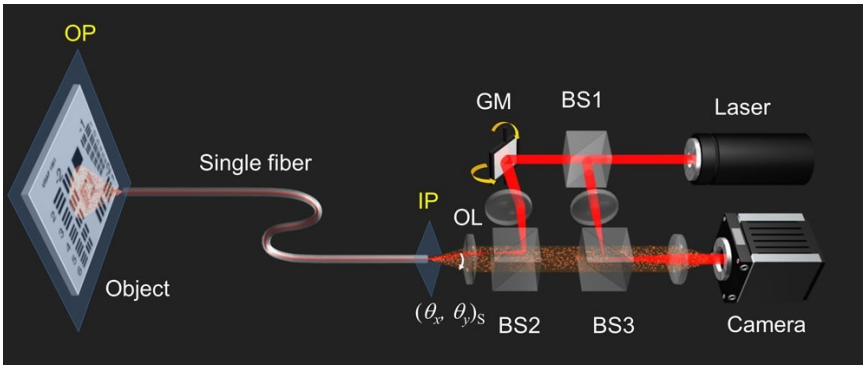

FIGURE 2.16: Experimental scheme of lens-less microendoscopy by a single fiber 2.16

Multi-core fiber wide-field imaging endoscopes

In 2016, Tsvirkun et al. reported a wide-field lens-less endoscopy using multi-core fiber [59]. The authors in this paper demonstrated real-time pixelation-free wide-field imaging (cf Section 2.1.2) through an aperiodic multi-core fiber without any distal opto-mechanical elements or proximal scanners. Thus the outer diameter of the probe is the diameter of the fiber itself (about 360 µm). Taking the advantage of the memory effect in multi-core fibers, the images in this system are directly obtained without any post-processing using a static wavefront correction obtained from a single calibration procedure. This approach allows for video-rate imaging with imaging speed not limited by the wavefront-shaping device refresh rate. Moreover, authors showed that their system is capable of optical sectioning, by wavefront control (using spatial light modulator) at the fiber proximal end.

2.2.4 Confocal imaging endoscopes

Another approach in fiber endoscopes is the confocal endoscope. An example which is commercialized by the company Mauna Kea Technologies (https://www.maunakeatech.com/en/) is shown in Figure 2.17 [60]. This type of endoscope is based on an imaging fiber bundle, made up of typically 10000 tightly-packed cores, that can transfer an intensity image from one end to the other with each core representing one pixel of the image, thus a core in the fiber bundle work as a confocal pinhole (as illustrated in Section 2.1.3). And the imaging system becomes confocal due to the presence of the imaging fiber bundle. The confocal endoscope can then be thought of as a table-top point-scanning microscope with one end of the imaging fiber bundle in the object plane and the other end in proximity with the sample, relaying the image between the two planes. In consequence, confocal endoscope has no active elements on the tip of the fiber on the sample side, reducing the probe size to the fiber bundle diameter.

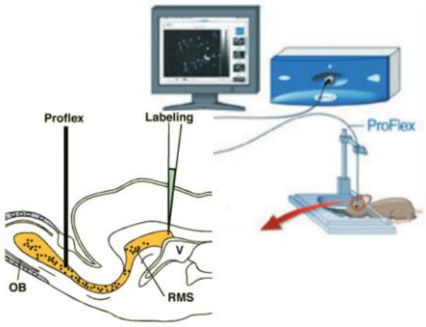

FIGURE 2.17: Schematic representation of a part of the brain showing the site of labeling and site of imaging with the endoscope probe [60].

2.2.5 Point-scanning imaging endoscopes

Fiber-scanning endoscope

Another approach to fiber endoscope is the fiber-scanning endoscope. This type of endoscope uses a fiber with single core. The use of this kind of fibers brings the advantage of the possibility of two-photon imaging, since the fiber can be optimized to transport ultra short-pulses. However, in this method an active device is required on the fiber tip on the sample side to can scan the beam across the sample in order to generate spatially resolved images by point-scanning (cf Section 2.1.4). Fiber-scanning endoscopes typically use a piezo-electric actuator as the active element.

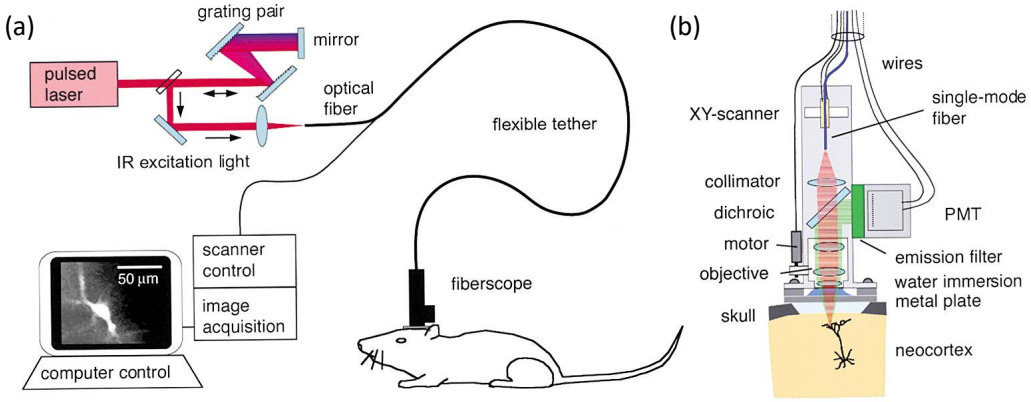

FIGURE 2.18: (a) Fiberscope setup (b) Microscope design [61].

The first two-photon fiber-scanning endoscope is introduced by Helmchen et al. [61] in 2001. The authors demonstrated a fiber-scanning endoscope that is small and light enough to be carried by a rat. The resolution of this fiberscope was sufficient to resolve dendritic morphology and Ca2+ dynamics in cortical layer 2/3.

Another examples of fiber-scanning endoscopes that use a piezo-electric actuator as the active element are demonstrated in Ref. [62] (few grammes, ∅4.2 mm × 71 mm) and Ref. [63] (5.5 grammes, 10 × 10 × 40 mm), and shown in Figure 2.19(a).

A very similar approach is to use a micro-electromechanical systems (MEMS) mirror at the fiber tip as the active element. Such as the fiber MEMS-scanning endoscope demonstrated in Ref. [64] (2.15 grammes, ∅10 × 40 mm) is shown in Figure 2.19(b).

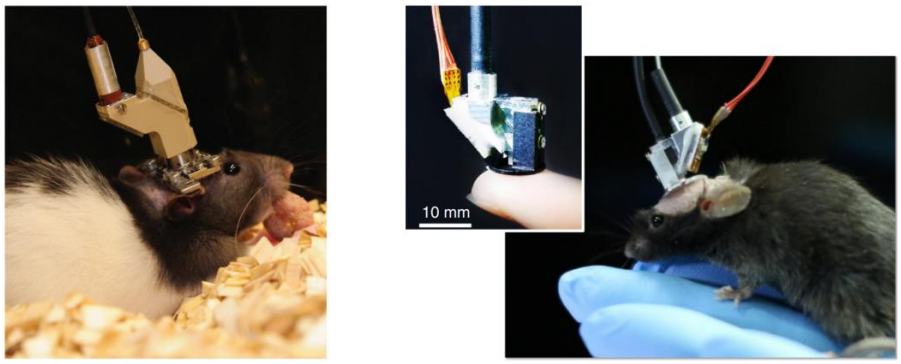

FIGURE 2.19: (a) Fiber-scanning endoscope [63]. (b) Fiber MEMS scanning endoscope [64].

Other systems of fiber-scanning endoscopes comprise compact needle probes with graded-index fiber lenses (∅350 µm) housed in hypodermic needles (22-gauge, ∅718 µm) have been demonstrated in Ref. [65]. In this reference, Scanning the beam was achieved by mounting the lensed fiber end on a two-axis translation stage consisting of a motorized stage and a piezoelectric stage which acted as the slow and fast scanning axes.

The fiber-scanning endoscopes presented in this section are still bulky, since the size of the probe is defined by the size of the active element placed at the fiber tip, which is in the order of several millimeters. However, with the emergence of wavefront shaping techniques (such as the spatial light modulator presented in Section 2.1.1), this issue has been overcome. Moreover, the ability to control the wavefront at the tip of the optical fiber offers new features such as axial sectioning. We will present in the coming sections, fiber-scanning endoscopes without any scanner attached to the fiber tip, however scanning by the use of a wavefront shaper at the proximal end of the fiber.

Multi-mode fiber point-scanning imaging endoscopes

Sivankutty et al. demonstrated two-photon endoscopic point-scanning imaging through an ultra-thin rigid endoscope consisting of a few centimeters long graded-index multi-mode fiber with a diameter of only 125 µm [66]. The authors of this paper displayed that the ultra-thin rigid endoscope retains the optical sectioning capability in two-photon imaging expected from an objective lens with the same numerical aperture as the multi-mode fiber.

Figure 2.20 shows the setup used for the two-photon imaging experiments. Laser light from the fs-laser (920 nm wavelength) is incident on a two-dimensional spatial light modulator (2D-SLM). In order to facilitate imaging at a speeds higher than the update rate of the 2D-SLM, a piston-tip-tilt deformable mirror (DM) with an update rate in excess of 1 kHz is employed. As the transmission

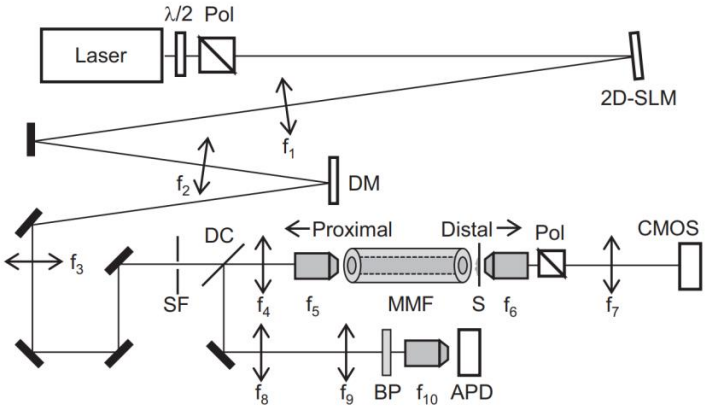

FIGURE 2.20: Experimental setup of two-photon endoscopic imaging [66]

matrix of the multi-mode fiber is known, an input coefficients defined in specific rows of the transmission matrix are sequentially sent to the wave front shaper (2D-SLM). These input coefficients maximize injection into specific output focus on the sample. Then the two-photon fluorescence generated in the sample is back-collected through the multi-mode fiber, split off by a dichroic mirror, and detected by a single-point detector (avalanche photodiode (APD)) located at the proximal end of the multi-mode fiber.

Multi-core fiber point-scanning imaging endoscopes

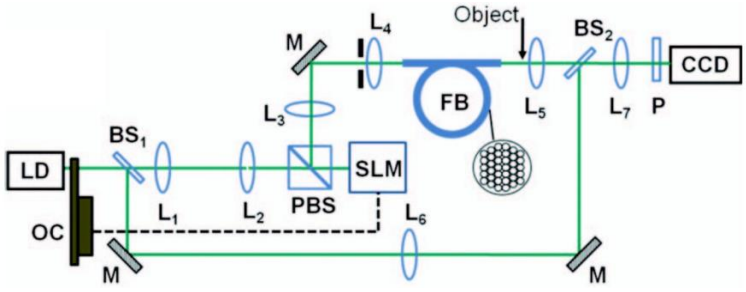

FIGURE 2.21: Experimental setup [55]

Thompson et al. [55] were the first to report imaging with a lens-less endoscope based on a waveguide with multiple cores. The waveguide that was employed was an "imaging fiber bundle," which is a class of multi-core fiber which is available commercially. The authors used a single-SLM approach (Figure 2.21) to control the phase of light propagating in a 500-core subset of a waveguide containing a total of 30,000 cores. The authors were able to acquire transmission images of a USAF test chart over an 80 μm field-of-view and could also demonstrate three dimensional control of the focal spot.

Andresen et al. realized a lens-less endoscope employing a custom designed multi-core fiber that they had optimized for application in lens-less endoscopy [49]. The authors in this paper demonstrated how to achieve video-rate imaging

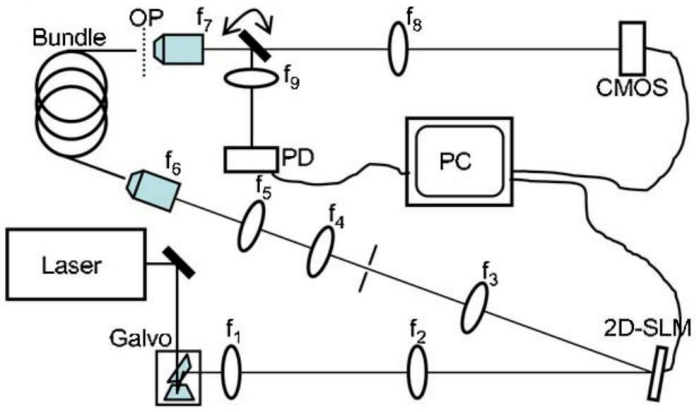

FIGURE 2.22: Experimental setup [49]

in one-photon lens-less endoscopy. The authors used the system of galvanometric scan mirrors in conjunction with an SLM to interface the multi-core fiber with the excitation laser (as shown in Figure 2.22). Using a subset of 91 cores out of the 475 cores of the multi-core fiber, the authors demonstrated transmission images of a USAF test chart as well as 3D control over the focal spot. The multi-core fiber in this paper was designed with extremely low cross talk between cores, which gave the advantage of a very large memory effect The authors exploit the memory effect in the multi-core fiber to use galvanometric scan mirrors located at the proximal end of the multi-core fiber to scan the focal point across the sample located at the distal end of the multi-core fiber. Consequently, the authors in this paper were able to acquire transmission images of a USAF test chart at a frame rate up to 12 Hz, limited only by the resonance frequency of the galvanometric scan mirrors. This paper demonstrated that arbitrary scan rates and also arbitrary scan patterns can be achieved in lens-less endoscopes without resorting to complex calculations of the phase mask on the SLM, using instead the memory effect together with scan mirrors.

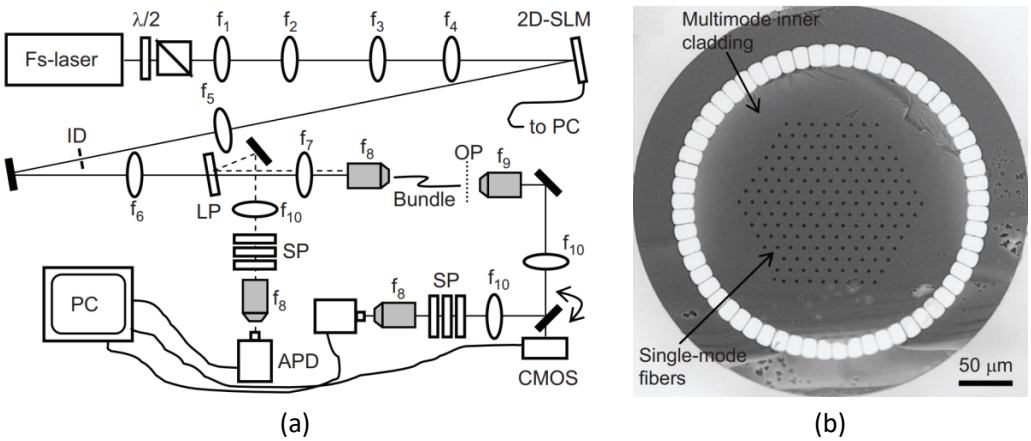

FIGURE 2.23: (a) Experimental setup (b) MCF with single-mode cores and a multi-mode inner cladding [67].

In 2013, Andresen et al. demonstrated for the first time two-photon imaging acquired with true endoscopic detection [67]. The endoscope probe was a

double-cladding bundle of 169 single-mode fibers, with a 360 µm total outer diameter. And the double-cladding was a ring of air holes around the cores (Figure 2.23(b)). The authors were able to acquire two-photon images of a test sample (a sample of rhodamine 6G crystals). Image formation proceeds by point-scanning of the distal focus using a two-dimensional SLM (Figure 2.23(a)). Point excitation and scanning was achieved by coherent combining of femtosecond light pulses propagating in the single-mode fibers. And back-scattered two-photon fluorescent signal was collected and transported through the multi-mode inner cladding back to a detector located at the proximal side. The authors demonstrate the effectiveness of the double-clad bundle at collecting back-scattered signal by comparing distal and proximal signal detection, where quantitatively similar results appear.

2.2.6 Transmission matrix measurements

The Transmission matrix measurement can be done in several basis, for instance, in localized mode basis [68, 69], fiber mode basis [70], and in the basis of plane waves [71, 72]. There is no restriction on expressing and measuring the transmission matrix using the same basis at the input and output, since changing basis can be performed (as shown in Chapter 1.Section 1.6). In the following section we will point out some of the transmission matrix measurement methods reported in the literature in the field of imaging through optical fibers.

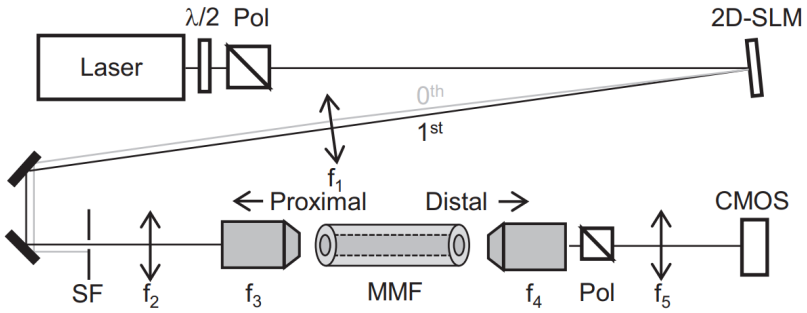

FIGURE 2.24: Scheme of experimental setup [66].

Sivankutty et al. [66] reported the use of transmission matrix approach to do two-photon endoscopic point-scanning imaging through a graded-index multi-mode fiber (detailed in Sectioc 2.2.5). The authors of this paper use a simplified single-polarization phase-only transmission matrix approach.

Figure 2.24 shows a sketch of the experimental setup of the TM measurement. A laser beam is incident into a 2D spatial light modulator (SLM) on which a phase mask of hexagonal segments on a triangular grid is displayed. The segment with index i diffracts light into the 1^{st} order in order to project the incident light onto input mode i with a controllable phase ϕ_i from 0 to 2π. To measure the transmission matrix, authors used the phase-retrieval method, where they measure the phase of every output mode for every input mode. The measurement algorithm is as follows. Two modes sent into the multi-mode fiber

by a certain phase mask, the reference mode 0 with phase 0 and the mode under test i with phase ϕ_j. The input basis is the basis of quasi-plane waves (characterized by their wave vectors) and are generated by wave front shaping methods with controllable phases. And the output basis are the localized modes (characterized by their location) whose locations are conjugated to the pixels of a CMOS camera. Then the intensity in all pixels is recorded for 8 equidistant values of ϕ_j between 0 and 2π. Accordingly, they measured the complex part of the transmission matrix relative to the complex part of the first row.

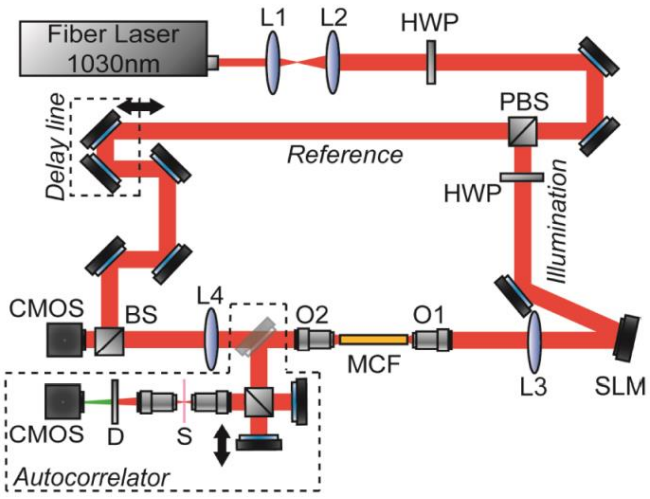

FIGURE 2.25: The optical setup for measuring the transmission matrix through the multi-core fiber [73].

In 2017, Conkey et al. demonstrate the use of transmission matrix approach for controlling the propagation of light through a multi-core fiber which is used for delivery and control of high peak power (more than 1012 W/cm^2) ultrashort pulses for ablation [73].

The transmission matrix is measured by capturing the output fields of orthogonal input modes after propagation through the multi-core fiber. The input field is described by the fiber modes (fundamental modes of the individual cores) at the fiber facet (cf Section 1.6.3) and output field is described spatially as pixels defined in a certain plane at a distance from the distal facet of the fiber (cf Section 1.6.4). Therefore, transmission matrix is expressed in fiber mode basis as the input basis and localized mode basis as the output basis.

Figure 2.25 shows the experimental setup used to measure the TM. An ultra-fast laser source is split into reference and illumination paths. The illumination path images a spatial light modulator (SLM) onto the proximal facet of a multi-core fiber. the transmission matrix is measured by applying a series of plane waves with varying spatial frequencies to the input of the multi-core fiber. For each such input, the output field of the multi-core fiber is recorded holographically, by mixing with reference beam on the CMOS camera. Then, the set of all these input-output measurements forms the transmission matrix.

Kim et al. make use of the binary control of a digital micromirror device (DMD) to measure the transmission matrix of a fiber bundle [74]. The authors measure the full transmission matrix using an external reference. Then, from

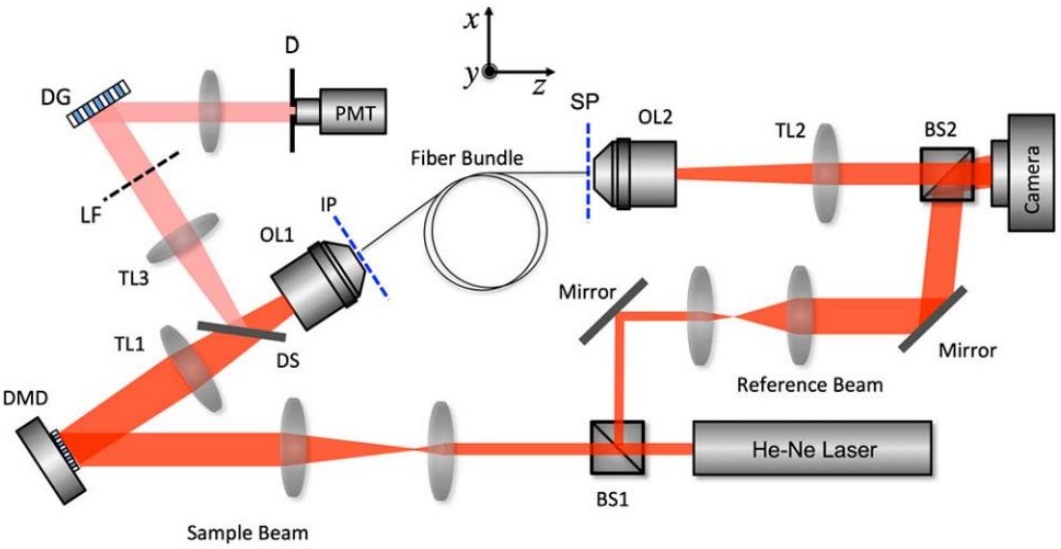

FIGURE 2.26: Scheme of experimental setup for recording a transmission matrix [74].

the measured transmission matrix, they identified a specific binary pattern of the DMD that would generate a focus at sample plane. By scanning the focus across the sample, they achieved a fluorescence endoscope imaging with near video-rate acquisition.

The experimental setup is schematically described in Figure 2.26. He–Ne laser was divided into sample and reference beams using a beam splitter. The DMD with a 1024×768 micro-mirror array was positioned at the conjugate plane to the input plane (IP) of the fiber bundle through the 4f configuration. The transmission matrix is measured in the basis of spatial coordinates at the input plane and sample plane as input and output bases, respectively.

The transmission matrix is measured as follows. First measuring the superposed response of the fiber to a randomly chosen large pixel in the input basis, and then unfolded it to the response for each large pixel by means of a matrix inversion. Then a generated random patterns (speckles) were uploaded to the onboard memory of the DMD and displayed sequentially at the input plane. The output complex field is recorded at a sample plane located 350 µm away from the bundle as an interference between reference plane wave and wave going out of the fiber bundle. Then, a complex field map is generated at the sample plane for the series of speckle basis at the input plane. Then, using the measured output field and predetermined (input) speckle sequences, they computed the transmission matrix.

2.2.7 Applications

The current state-of-the-art in fiber endoscopes is concentrating on imaging neuronal activity in living animals. We will present in the following section a representative selection of the current state-of-the-art in fiber endoscopes.

Ohayon et al., present a micro-endoscope design to image neural activity at arbitrary depths through an ultra-thin multi-mode optical fiber probe (120

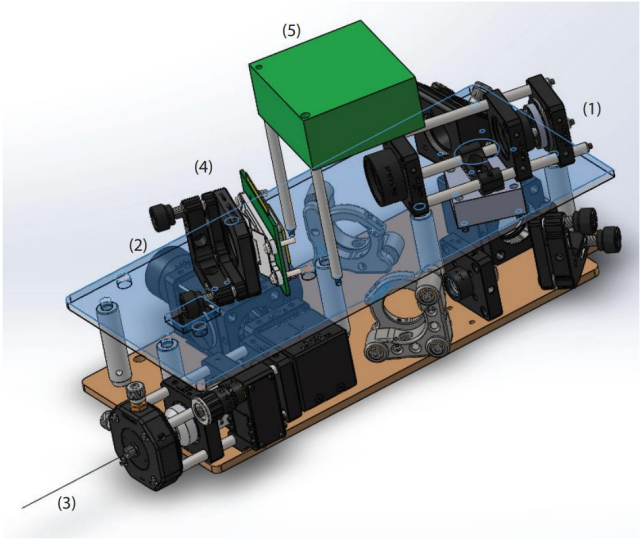

FIGURE 2.27: Mechanical system design. (1) SMF entry port for a illumination light, (2) exit port for fluorescence emissions (large diameter multi-mode fiber), (3) Imaging multi-mode fiber (120 µm), (4) DMD, (5) DMD PCB controller [75].

µm) [75]. The authors uses single-mode fiber to transport two wave-length illumination light into a wavefront shaper (digital mirror device (DMD)) to control light in a multi-mode fiber that goes into the brain of a mouse. Then fluorescent emissions are collected with the same fiber, relayed back and focused on a large diameter multi-mode fiber, which transports fluorescence emissions to the detectors. The two wave-length illumination is used to allow multi-spectral imaging. Figure 2.27 represents the mechanical design of the imaging system highlighting the main components for the imaging process. The authors tested their imaging system by imaging dynamic neuronal activity in-vivo in rodents expressing a genetically encoded calcium indicator. The system was able to achieve micron-scale resolution with acquisition speed that is sufficient to capture rapid neuronal dynamics in-vivo.

Turtaev et al., designed a compact and high-speed imaging device capable of resolving micron-sized subcellular neural structures [76]. The authors demonstrate fluorescent imaging at the tip of a multi-mode fibre, achieving a resolution of 1.18 ± 0.04 µm across a 50 µm field of view, yielding 7-kilopixel images at a rate of 3.5 frames/s. The authors used standard commercially available multi-mode fiber with 50 µm core diameter, as the endoscopic probe. Then they polished the terminal end of the fiber in flat-top cone shape to reduce the external diameter (cladding) from 125 µm to 60 µm (Figure 2.28(b)).

Figure 2.28(a) show the scheme of the imaging setup. Fluorescence signals are recorded from deep brain regions of anaesthetised mice on a detector located at the proximal end to construct the point-scanning image, using digital micro mirror devices (DMD) as scanning element.

Vasquez-Lopez et al. demonstrated high-resolution fluorescence imaging of subcellular neuronal structures, in deep-brain regions of living mice, as well as monitored stimulus-driven functional Ca2+ responses [77]. The imaging system

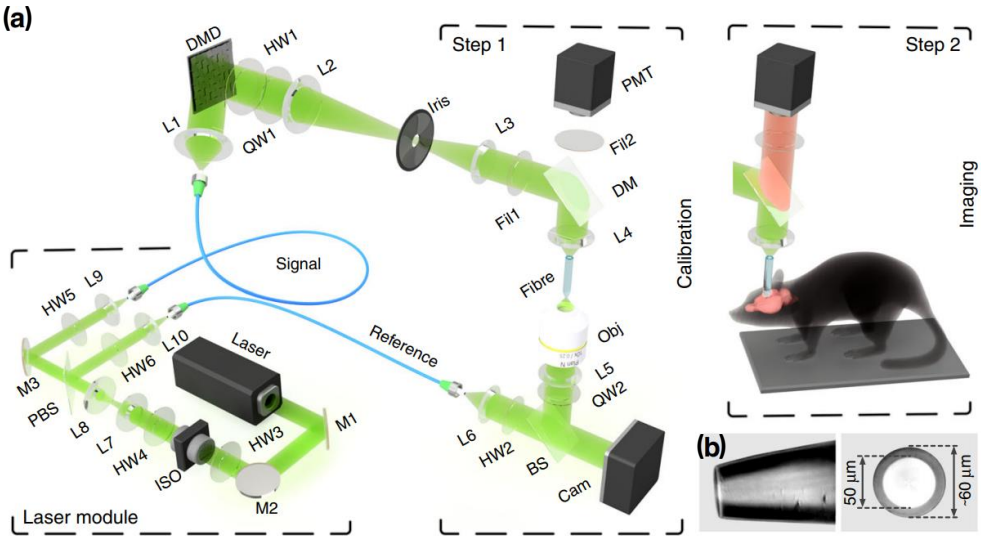

FIGURE 2.28: (a) Scheme of the imaging setup (b) Flat-top cone termination of the multi-mode fiber probe [76].

here achieve diffraction-limited imaging performance using wavefront control of light propagation through a single multi-mode fiber with 50 µm core diameter (125 µm external diameter including the cladding). The wavefront shaper used in this system was a spatial light modulator (SLM).

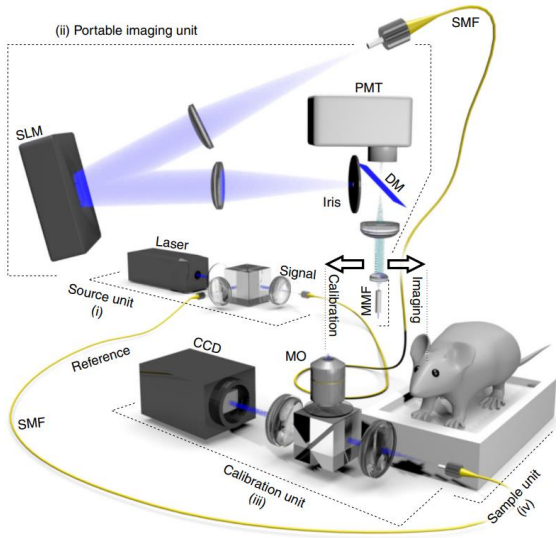

FIGURE 2.29: Schematic of the experimental system [77].

The authors were able to acquire in-vivo minimally-invasive fluorescent imaging of neurons after lowering the fiber 1.8 mm into the brain of an anesthetized mouse. Also, they show that their imaging system can operate at a scan rate of 10 ms per pixel (frame rate = 2.4 s per 120 × 120-pixel frame).

The three references above, demonstrate the feasibility of cellular-level imaging deep inside living mouse brain tissue through optical fiber by point-scanning endoscopy with fluorescence contrast. The current state-of-the-art show the

superiority of point-scanning imaging on other types of imagining mentioned through the chapter.

2.3 Position of the work

The work of thesis is focused on designing a specialty optical fiber destined for integration into lens-less endoscope, as being the most promising ultra-miniaturized imaging tool for application in minimally-invasive imaging in living mice.

The initial reports of lens-less endoscopy based on a bundle of single-mode fibers published in Ref. [55], and the first demonstrations of microscopic imaging of objects through multi-mode fiber which did not require any optical elements between the fiber and the object were published in Refs. [54, 56, 44]. However, also multi-core fiber presents great potential as imaging wave guides due to its particular merits [50]. In this thesis work, we focus on multi-core fiber because it is more readily compatible with two-photon imaging modalities [67, 50, 78] widely used in bio-medical microscopy.

First, we numerically investigate a potential solution for ameliorating spatial resolution in lens-less endoscopes. Our approach was similar to the idea of Ref .[79], where authors placed a highly scattering medium in front of the distal tip of a multi-mode fiber to increase the effective numerical aperture of the system. That approach gains resolution, but at the cost of losing power. Our approach is to fix a short segment of multi-mode fiber with micro-structured refractive index profile to the tip of a multi-core fiber. We model this structure numerically and we show that this approach gains in resolution as well as in power.

Then, we realized a lens-less endoscope employing a custom designed multi-core that we had optimized for application in two-photon lens-less endoscopy. The approach here is to taper the optimized multi-core fiber with the aim of simultaneously optimizing it for transport and imaging. First, we develop and validate a fast numerical model capable of predicting the essential properties of any multi-core fiber from its structural parameters, and so one can use this model to compute the properties of any multi-core fiber with any parameters or any core layout within few seconds and without the need to do all experiments. Then, we show that tailoring of the taper profile is a degree of freedom that can be efficiently exploited for ameliorating multi-core fiber based lens-less endoscopes and we have shown that tapering multi-core fiber contributes to address the major power delivery issue that has faced multi-core fiber based lens-less endoscopes [80]. Moreover, we coated the tapered multi-core fiber with a low index polymer to act as a double-clad, and show its efficiency in collecting the backscattered fluorescence.

We have gone further, and we apply tapering on a Fermat's golden spiral multi-core fiber reported by Ref. [81] to get rid of replica images that is always present when using hexagonal multi-core fibers and maximizing the field of view of imaging. Tapering a Fermat multi-core fiber add to the fiber the advantage of increasing the collection of two-photon signal.

Chapter 3

NA-increasing multi-mode fiber

In a lens-less endoscope, the exact choice of fiber has two important impacts: (i) the resilience to bending; (ii) the imaging resolution. A given fiber is not assured to be optimized for (i) and (ii) simultaneously. It can be realized that the resilience to bending (i) depends on the fiber parameters over the major part of its length; while the imaging properties (ii) only depend on the fiber parameters in the last centimeter or so, specifically its modal content.

In this work, we will investigate a potential approach to decouple the two. Our hypothesis is that the fiber itself could be optimized for bend resilience. As an example, in Ref. [82] it was demonstrated that a helically-twisted multi-core fiber is resilient to bends with constant bend radius of curvature, ie the transmission matrix of the multi-core fiber is invariant to bends. And the fiber mode space could be modified over the last few centimeters to better fit image resolution requirements by a small, specific wave guiding structure fixed to the main fiber. Specifically, the following sections explores several ways to achieve such a structure. We will limit ourselves to a structure which effects a "mode densification", ie mapping all fiber modes to scaled down versions of the same modes, improving image resolution by the same scaling factor. To this end we have made a model based on radial scaling of the refractive index profile as a function of the longitudinal coordinate. We consider first a step-wise scaling by concatenating a multi-mode fiber (Section 3.1) and then a smooth scaling through a process of dopant diffusion (Section 3.2).

3.1 Concatenation of multi-mode fibers

The first approach is concatenating multi-mode fiber sections with decreasing core radius but with increasing refractive index difference Δn under the constraint that the integral of the two-dimensional refractive index profile be constant. Consequently, the number of guided modes is conserved from the input to the output of the structure, and thus all sections guide the same number of modes.

Figure 3.1 is a schematic illustration of the concatenation, the first section is a step-index multi-mode fiber of core radius R_1, the core radius decreases from one section to another with step Δr to end up with fiber of core radius R_n smaller than R_1. All the sections are of the same length l.

Our model is based on scalar mode solver (cf Section 1.4.3) in order to calculate the mode profiles and effective indices of the guided modes in each

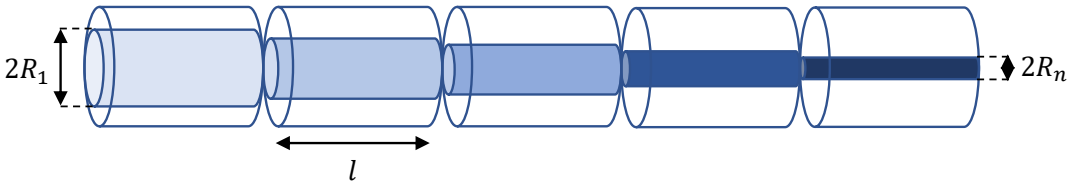

FIGURE 3.1: Concatenation of multi-mode fiber sections.

individual section c ($1 \leq c \leq n$), as a function of wavelength λ and core radius R_c ($R_1 \leq R_c \leq R_n$). The refractive index difference of the first section ($c = 1$), is $\Delta n^{(1)} = n_{\text{co}} - n_{\text{clad}}$. Then the refractive index difference $\Delta n^{(c)}$ ($1 < c \leq n$), decreasing from one section to another under the following constraint:

$$\Delta n^{(c)} = \Delta n^{(c-1)} \frac{R_{c-1}^2}{R_c^2} \tag{3.1}$$

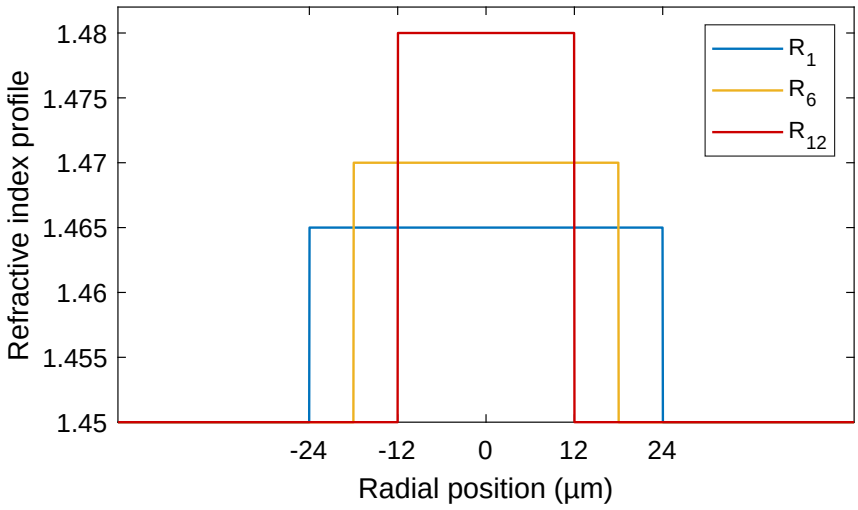

FIGURE 3.2: Refractive index profile for three sections of different radii $R_1 = 24$ µm, $R_6 = 18$ µm, $R_{12} = 12$ µm. Where $\Delta n^{(1)} = 15 \cdot 10^{-3}$ and $\Delta n^{(6)}, \Delta n^{(12)}$ are calculated using Equation (3.1).

Then, we can compute the transmission matrix of each section as a diagonal matrix expressed in the fiber mode basis with M modes (cf Section 1.6.3), and is of dimension $M \times M$. The diagonal elements of the transmission matrix $\mathbf{H}^{(c)}$ of section number (c) is:

$$h_{ii}^{(c)} = e^{i\beta_i^{(c)} l} \tag{3.2}$$

with $1 \leq i \leq M$ and l the length of the considered multi-mode fiber section.

The structure is made up of a concatenation of multi-mode fiber sections, thus it is formed of spliced sections of multi-mode fibers of different core radii with descending order, but having the same outer diameter. Consequently, at each splice the modes of one segment are projected onto the modes of the next

segment. This projection is studied by computing the overlap integral between the LP modes of each two consecutive sections. Therefore, the overlap between the LP modes ($LP_{l'm'}^{(c-1)}$) of section $(c-1)$ and LP modes ($LP_{lm}^{(c)}$) of section (c) build up a projection matrix $\mathbf{P}^{(c-1,c)}$ of in the fiber mode basis with $M \times M$ dimensions, where M is the number of fiber modes. The projection matrix of the first section ($c = 1$) is a unitary matrix. Then for the rest sections ($1 < c \leq n$), the elements of the projection matrices are computed by the following overlap integrals:

$$p_{ij}^{(c-1,c)} = \langle \psi_{l'm'}^{(c-1)} | \psi_{lm}^{(c)} \rangle = \int_0^{2\pi} \int_0^{\infty} \left[\psi_{l'm'}^{(c-1)}(r,\theta) \right]^* \psi_{lm}^{(c)}(r,\theta)\ r \mathrm{d}r \mathrm{d}\theta \tag{3.3}$$

Where $l(l')$ are the azimuthal modal number (≥ 0), and $m(m')$ are the radial number (≥ 1). As mentioned in Equation (1.31), $\psi_{lm}^{(c)}(r,\theta)$ has two solutions, the cosine solutions correspond to LP "even" modes and the sine solutions correspond to the LP "odd" modes. Thus we will obtain four forms of solution:

$$p_{ij}^{(c-1,c)} = \int_0^{\infty} \left[\psi_{l'm'}^{(c-1)}(r) \right]^* \psi_{lm}^{(c)}(r)\ r \mathrm{d}r \cdot \begin{cases} \int_0^{2\pi} \cos(l'\theta) \cos(l\theta)\ \mathrm{d}\theta & \text{for e-e modes} \\ \int_0^{2\pi} \sin(l'\theta) \sin(l\theta)\ \mathrm{d}\theta & \text{for o-o modes} \\ \int_0^{2\pi} \cos(l'\theta) \sin(l\theta)\ \mathrm{d}\theta & \text{for e-o modes} \\ \int_0^{2\pi} \sin(l'\theta) \cos(l\theta)\ \mathrm{d}\theta & \text{for o-e modes} \end{cases} \tag{3.4}$$

Where e-e means even-even modes, o-o means odd-odd modes, e-o means even-odd modes, and o-e means odd-even modes.

The overlap integral of e-o modes and o-e modes is null. However, the overlap integral of e-e modes and o-o modes have three solutions depending on the value of azimuthal modal number $l(l')$. Therefore, Equation (3.4) becomes:

$$\text{For e-e modes: } p_{ij}^{(c-1,c)} = \int_0^{\infty} \left[\psi_{l'm'}^{(c-1)}(r) \right]^* \psi_{lm}^{(c)}(r)\ r \mathrm{d}r \cdot \begin{cases} 2\pi & \text{for } l = l' = 0 \\ \pi & \text{for } l = l' \neq 0 \\ 0 & \text{for } l \neq l' \end{cases} \tag{3.5}$$

$$\text{For o-o modes: } p_{ij}^{(c-1,c)} = \int_0^{\infty} \left[\psi_{l'm'}^{(c-1)}(r) \right]^* \psi_{lm}^{(c)}(r)\ r \mathrm{d}r \cdot \begin{cases} 0 & \text{for } l = l' = 0 \\ \pi & \text{for } l = l' \neq 0 \\ 0 & \text{for } l \neq l' \end{cases} \tag{3.6}$$

Our model computes the total transmission matrix in the fiber mode basis of the structure as the product of all the (diagonal) transmission matrices of

individual sections and the projection matrices between consecutive sections:

$$\mathbf{H} = \prod_{c=n}^{2} \left(\mathbf{P}^{(c-1,c)}\, \mathbf{H}^{(c)}\right) \mathbf{H}^{(1)} \tag{3.7}$$

Then We can be able to calculate the losses of the structure from the computed total transmission matrix $\mathbf{H}$ by the following expression:

$$\text{Losses} = 1 - \frac{\sum_{i,j}^{M} |h_{ij}|^2}{M} \tag{3.8}$$

Where M is the number of fiber modes that defines the size of the transmission matrix $\mathbf{H}$.

We start the structure with a step-index multi-mode fiber with the following parameters: fiber core size 24 µm, $\Delta n^{(1)} = 15 \cdot 10^{-3}$. Then at 700 nm wavelength, we obtain a multi-mode fiber with 515 modes. We choose the length of each individual section to be $l = 1$ µm. We found that with $R_1 = 24$ µm and $R_{12} = 12$ µm, with 12 segments, i.e. $\Delta r = 1$ µm, the structure has a total loss 61.59 %, calculated from the computed transmission matrix as shown in Equation (3.8). However, when we increase the number of segments ten-fold, i.e. $\Delta r = 0.1$ µm, the total loss decreases to 22.57 %. Evidently, losses are higher the fewer the number of segments.

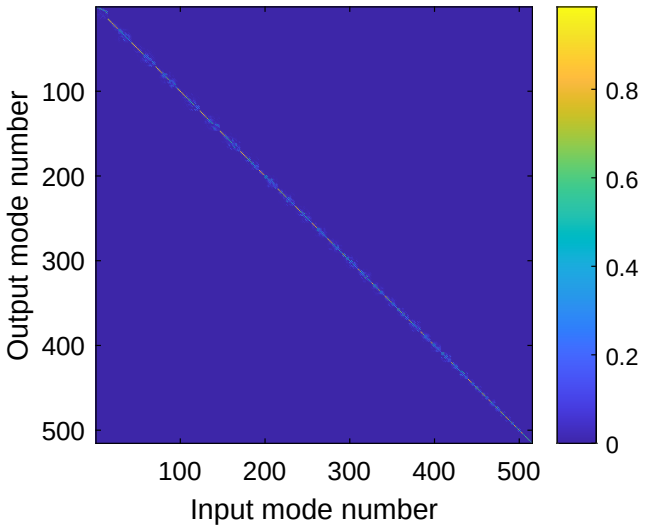

FIGURE 3.3: Transmission matrix total for structure made up of 1200 sections ($R_1 = 24$ µm, $R_{1200} = 12$ µm) each of them guide 515 modes.

We proceed then to the smoothly-varying counterpart which we model by letting $\Delta r \to 0$ in the previous model. The total loss decreases to 12.1 % when the number of segments is increased hundred-fold, ie when $\Delta r = 0.01$ µm. We conclude that, as we let $\Delta r \to 0$, the total loss tends to zero, and thus the propagation becomes adiabatic.

Figure 3.3 presents the transmission matrix of this structure which is a nearly diagonal matrix in the fiber mode basis. From the transmission matrix, we are able to generate the input and output focus presented in Figure 3.4(a) and Figure 3.4(b), i.e the foci that can be generated from coherent superposition of the modes guided in the input and output ends of the structure respectively. To do so, we perform a base change operation on the transmission matrix (which is in modal basis) in order to express it in the input modal, output pixel basis (cf Section 1.6.4). Then we take one line of the transmission matrix corresponding to the central pixel, and we multiply the complex transpose of this line by the transmission matrix and this gives the output focus (cf Section 1.7.3).

The input focus presented in Figure 3.4(a) is generated from the first (input) segment of the concatenation, with $R_1 = 24$ µm. And output focus presented in Figure 3.4(b) is generated at the output of the structured multi-mode fiber, with $R_{1200} = 12$ µm. As shown by the figures, the output focus is smaller than the input focus by a factor 2 and its focus intensity is larger than that of input focus by a factor 4. Thus, by structuring the multi-mode fiber we can generate a smaller output focus with higher intensity.

In the context of lens-less endoscope these foci can be identified as point-spread functions, their widths representing the attainable image resolution. It is clear that image resolution is better with the point-spread function corresponding to the, smaller, output focus. Considering also that the structure conserves the number of guided modes from input to output, these results reveal the ability of this fiber with three-dimensionally structured refractive index to perform mode densification.

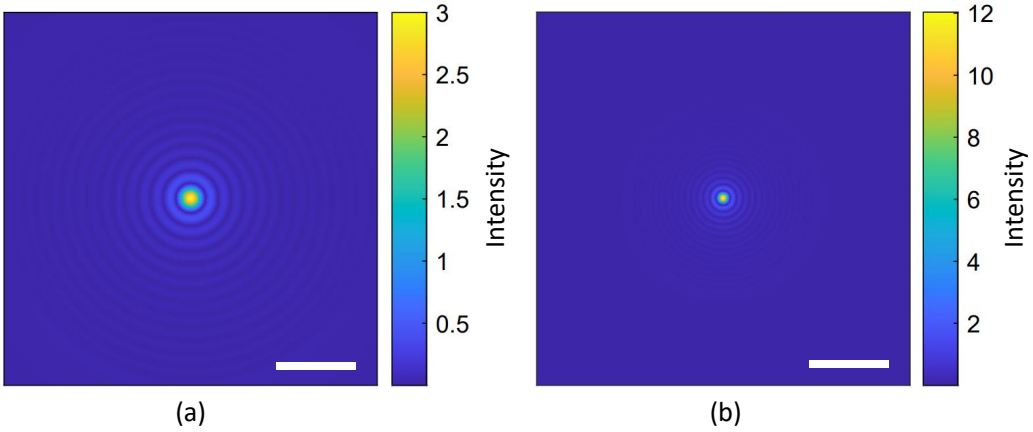

FIGURE 3.4: (a) Input focus, (b) output focus. Scale bar 10 µm

From the above results, we conclude that the concatenation approach to the targeted structure works as a numerical model. Especially that as we let $\Delta r \to 0$, the total loss tends to zero. However, this is not as easy as it appears. Since attaining low losses acquire huge number of fiber sections to be spliced and this would largely be offset by inevitable losses due to splice imperfections. Therefore, the aim now is if we can find a physical mechanism that produce the kind of index profile shown above to achieve targeted structure.

3.2 Multi-mode fiber with structured index profile

We hypothesize that a refractive profile likes the one in Figure. 3.1 could be experimentally generated through a process of dopant diffusion [83]. Such a process would result in a continuous fiber, avoiding the splice losses that were found to limit the concatenation approach (Sec. 3.1).

Our idea is to apply a gradient temperature longitudinally along the axis of a small core homogeneous step-index multi-mode fiber. Thus obtaining a fiber with diffused profile, where the diffusion of the core dopant could produce the refractive index profile.

3.2.1 Theory of dopant diffusion

When an optical fiber is subjected to a high temperature, dopant materials in the optical fiber spread out from areas of high concentration to the areas of low concentration. Then this phenomenon is called optical fiber thermal diffusion or dopant diffusion. The thermal diffusion process can manipulate the dopant concentration distribution and modify the refractive index distribution in the fiber, while the size and shape of the fiber cladding remain almost unchanged.

In the thermal diffusion process, the local dopant concentration C should be described by Fick's second law of diffusion [84] which predicts how diffusion causes the concentration C to change with respect to time. Then, the dopant diffusion equation is a partial differential equation relating the local dopant concentration gradients to the time-dependent dopant concentration and represented by:

$$\frac{\partial C}{\partial t} = \nabla(D\nabla C) \tag{3.9}$$

Where C is the local dopant concentration in $\mathrm{mol/m^3}$, D is the dopant diffusion coefficient in units of $\mathrm{m^2/s}$, and t is the heating time.

Equation (3.9) describes the general case of dopant diffusion for an arbitrary geometry. The dopant diffusion coefficient D is not constant, but depends on the dopant species, the host material, and the local temperature. The temperature of a heated fiber is almost uniform with regard to radial position r, thus it is reasonable to assume that the diffusion coefficient D is constant over the radial position r.

Since the diffusion length is typically much smaller than the fiber diameter, the boundary impacts can be neglected. The diffusion along the z-axis (axial direction) is also negligible since the concentration gradient is much more gradual along the z-axis than that along the r-axis (axial temperature gradients occur over many hundreds of micrometers and the axial concentration gradients within a fiber are very small).

If we neglect the axial and azimuthal diffusion, then Equation (3.9) yields a simplified dopant diffusion equation in radial coordinates

$$\frac{\partial C(r,t)}{\partial t} = D\frac{1}{r}\frac{\partial}{\partial r}\left(r\frac{\partial C(r,t)}{\partial r}\right) \tag{3.10}$$

where the dopant concentration C of the diffusion material is a function of the radial distance r and the heating time t. Note that the dopant concentration in the fiber keeps the conservation of mass during the whole diffusion process.

Various investigations have shown that diffusion coefficients in silica obey an Arrhenius relation, meaning that the diffusion coefficient scales with the exponential of the inverse temperature. This relationship can be expressed as:

$$D(T) = D_0 \exp(-\frac{E_{\text{act}}}{RT}) \tag{3.11}$$

where D_0 is the self-diffusion coefficient prefactor [m^2/s], E_{act} is the diffusion activation energy [J/mole], T is the heating temperature [K], and R is the ideal gas constant or universal gas constant, which can be expressed as 8.3145 [J/mol·K].

The diffusion of a dopant in a fiber containing a single chemical species, and the resulting refractive index profile, can be readily modeled. In such a case, either longer heating times or higher temperatures can be used to increase the amount of diffusion to achieve a target refractive index profile.

Given an arbitrary initial dopant concentration $C_0(r)$ at time $t = 0$. Green's functions yield a particularly convenient and efficient way to numerically solve Equation (3.10) for dopant concentration $C(r,t)$ at any radius r and time t [85]

$$C(r,t) = \frac{1}{2D(T)t}\int_{r'=0}^{r'=\infty} C_0(r')\ I_0(\frac{rr'}{2D(T)t})\ \exp(-\frac{r^2+r'^2}{4D(T)t})\ r'dr' \tag{3.12}$$

where I_0 is the zero-order modified Bessel function of the first kind, and r' is a variable of integration suffices. A single numerical integration of Equation (3.12) rapidly yields the dopant distribution given any initial dopant concentration.

In a step-index fiber whose core is comprised of a single dopant, the initial concentration distribution, $C_0(r)$, is a uniform C_0 from r=0 to $r = R_{\text{core}}$. So we can simplify Equation (3.12) for the dopant concentration for a step-index fiber $C_{si}(r,t)$ as

$$C_{\text{si}}(r,t) = \frac{1}{2D(T)t}\int_{r'=0}^{r'=R_{\text{core}}} C_0 \cdot I_0(\frac{rr'}{2D(T)t})\ \exp(-\frac{r^2+r'^2}{4D(T)t})r'dr' \tag{3.13}$$

As shown in preceding equations, D always appears with t. Thus we conclude that the heating time t can be increased or decreased to compensate for a slow or fast diffusion coefficient, respectively. Furthermore, a dimensional analysis of Equation (3.9) reveals a non-dimensional parameter τ_D which characterizes the extent of dopant diffusion and expressed as

$$\tau_D = \frac{Dt}{\delta_D^2} \tag{3.14}$$

where δ_D is a characteristic length scale for the diffusion. If we assume that δ_D equals to core radius R_{core} in a step-index fiber, and we let $\hat{r}$ denote the normalized radial position such that $\hat{r} = \frac{r}{R_{core}}$, we can express Equation (3.13) in a non-dimensional form

$$C_{si}(\hat{r}, \tau) = \frac{C_0}{2\tau_D} \int_{r'=0}^{r'=1} I_0(\frac{\hat{r}r'}{2\tau_D})\ exp(-\frac{\hat{r}^2 + r'^2}{4\tau_D})\ r'dr' \tag{3.15}$$

By setting τ_D of Equation (3.14) equal to unity we can obtain an equation which relates the characteristic diffusion length δ_D to the diffusion coefficient D and the time interval for the diffusion t_D

$$t_D = \frac{\delta_D^2}{D} \tag{3.16}$$

Equation (3.16) shows that the time required for a dopant to diffuse scales with the square of the characteristic length. This means that the diffusion proceeds more rapidly in a small core fiber than in a larger core fiber. Furthermore, as a dopant diffuses, its characteristic length scale (i.e core radius) increases and so the rate of diffusion decreases. Thus, when held at a fixed temperature, a dopant distribution changes most rapidly at the beginning of the heating, and more slowly as time goes on.

3.2.2 Structured multi-mode fiber

This section present a numerical study to simulate thermal diffusion of dopant in a standard multi-mode fiber with single dopant (germanium) and evaluate whether it is possible to produce a 3-dimensional refractive index profiles similar to the one presented in section 3.1.

First, we study the dependence of temperature on the dopant diffusion process, by studying the evolution of the diffusion coefficient with respect to temperature. As shown by Figure 3.5, the diffusion coefficient grow exponentially as temperature increases, and the diffusion process needs very high temperature to be significant. In the same context, for lower temperature, the evolution of the diffusion process becomes slower, and so need more heating time. And this is quite evident from the formula (Equation 3.12), where heating time and the temperature always appear together as factor $D(T)t$, which means that increasing temperature has the same effect as increasing the heating time.

Additionally, as a dopant diffuses, its characteristic length scale (i.e core radius) increases and so the rate of diffusion decreases. Therefore, we choose to do our simulations at fixed heat temperature, however increase heating time as we move along the fiber. To clarify more, at each length along the fiber, we are

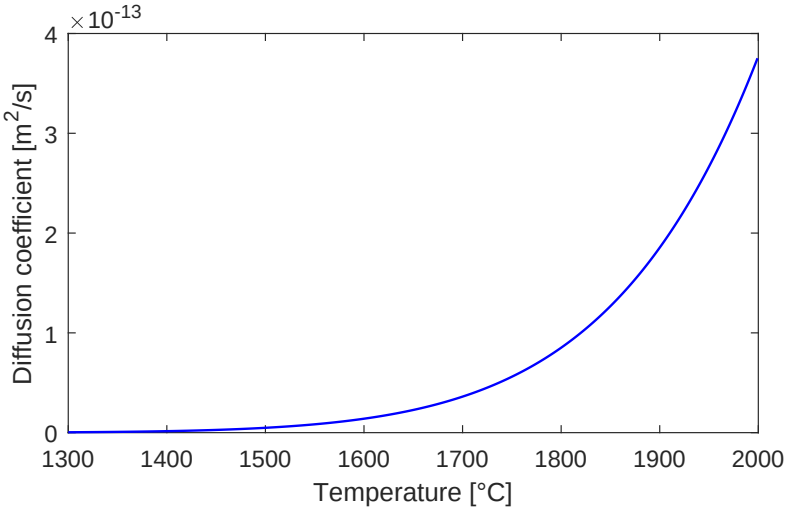

FIGURE 3.5: The evolution of the dopant diffusion coefficient with respect to temperature.

heating for a certain time, and as we move step along the fiber the heating time is increased. Therefore, as we fix the applied heating temperature, the diffusion of the dopant can only be controlled by controlling the time of exposure.

In our simulation, an initially step-index multi-mode fiber with 24 μm core radius and refractive step index $\Delta n = 30{\cdot}10^{-3}$ is subjected to 2000 °C temperature longitudinally with different heating time at different positions along its axis. And we study the evolution of the refractive index profile as function of heating time.

In thermal diffusion, the evolution of the fiber refractive index profile is largely predetermined by the initial dopant distribution. For germanium-doped core fiber, the refractive index is a linear function of the doping concentration [86]. Therefore, We assume that the refractive index profile of the fiber in the whole thermal diffusion region is proportional to the dopant distribution and is expressed as [87]:

$$n^2(r) = n_{\text{cl}}^2 + (n_{\text{co}}^2 - n_{\text{clad}}^2)\ C(r,t) \tag{3.17}$$

where $n_{\text{clad}} = 1.45$ and $n_{\text{co}} = 1.48$. And $C(r,t)$ is the germanium dopant concentration as a function of the radial distance r and heating time t, computed using Equation 3.13 and substituting D(T) by Equation 3.11. The parameters $D_0 = 1.9 \times 10^{-6}$ m^2/s and $E_{\text{act}} = 2.9 \times 10^5$ J/mol are obtained from the experimental data [88].

Figure 3.6 presents an illustration of this structured fiber and shows how the diffusion of the core dopant produces the refractive index profile and enlarge the core diameter of the fiber. Figure 3.7 presents the evolution of the refractive index profile as function of heating time (t). It shows the refractive index profiles of the step-index multi-mode fiber is varying to the quasi-Gaussian shape after one minutes of thermal diffusion. And as heating time increases the refractive index profile goes more near Gaussian shape, with very slight change in number of modes.

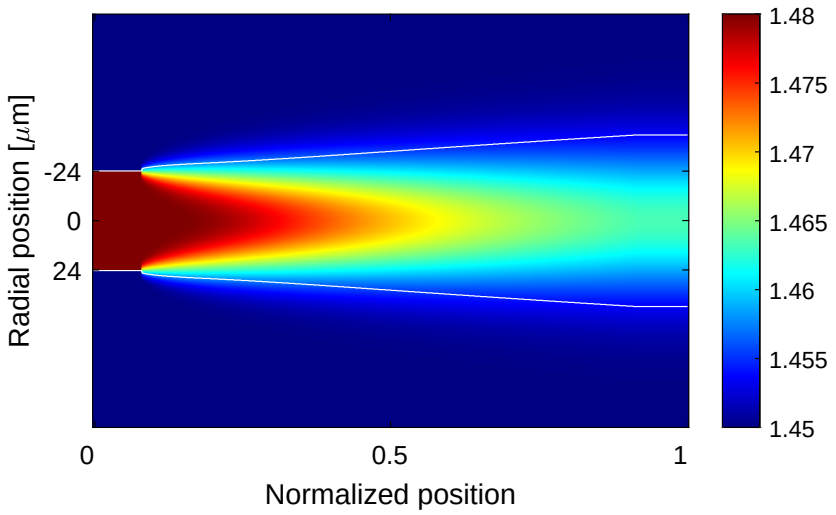

FIGURE 3.6: Schematic illustration of longitudinally dopant diffusion dependent structured fiber.

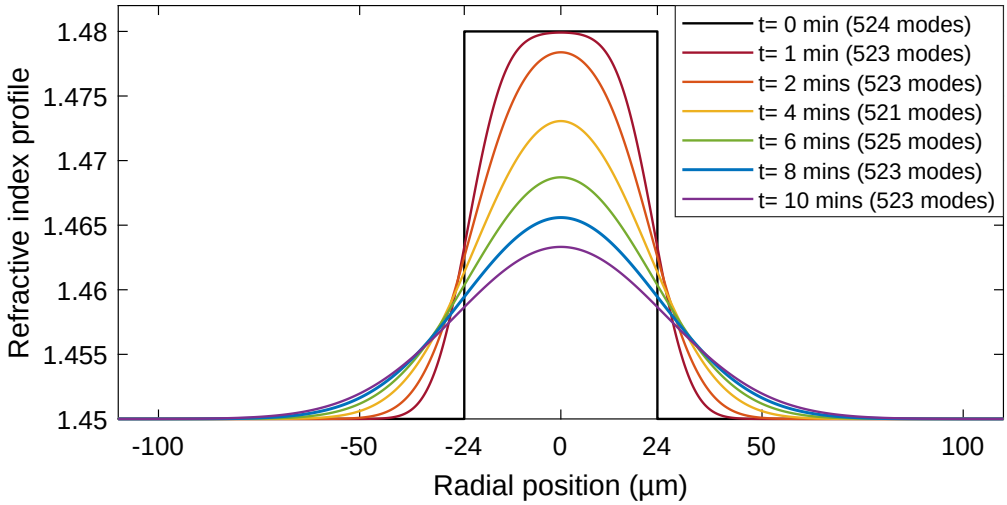

FIGURE 3.7: Refractive index profile as function of radial position for different heating times. R=24 μm ; $\Delta n = 0.03$; $T_{\mathrm{d}} = 2000$ °C.

As shown in Figure 3.7, the multi-mode fiber needs a very high temperature (2000°C) for several minutes to obtain clear evolution in its refractive index profile. In fact, if the fiber doesn't melt, we can keep it subjected to temperature as long as possible. However, in our case this is not practical, because we are not subjecting the whole length of the fiber to a uniform heating temperature at the same time. But, heating the fiber unevenly, and so we are heating for a certain time at each length along the fiber. And thus heating many points on the fiber can't be workable when each point needs a long time. Moreover, an excessive temperature may aggravates the deformation of optical fibers and makes their physical properties worse. Therefore, although structuring the refractive index profile by dopant diffusion process is theoretically feasible, experimentally, this still remains challenging.

3.3 Conclusion

This chapter has reviewed a numerical work for modeling a structured multi-mode fiber where we can bring modes closer together and increase the numerical aperture of the fiber. This structured fiber will be of great interest, for instance, it could act in a similar way as a grin lens that could work in lens-less endoscopes.

In fact, the approach of this structure is similar to the idea of Ref. [79] where authors placed a highly scattering medium in front of the distal tip of a multi-mode fiber to enable the formation of smaller sized foci by increasing the effective numerical aperture of the system. Authors were able to gain in lateral resolution, however the smaller foci were less intense, and thus they were losing in power. However as we have shown, in our approach, we were able to gain in resolution as well as in power.

We investigated two approaches to realize this structured fiber. The first one is concatenating multi-mode fibers of decreasing core diameter but constant surface area under the refractive index curve, and we found that in order to minimize the total losses in this concatenated fibers we need a very big number of sections, which is impractical. And the second approach is a fiber with longitudinally dependent refractive index profile obtained by dopant diffusion. And we found out that the diffusion times and temperatures are necessary to make such profile. The future might permit new ways of experimentally realizing the kind of wave guiding structures considered here.

Chapter 4

Tapered MCF: Design, fabrication, characterization and Application

4.1 Introduction

In a two-photon lens-less endoscope, the multi-core fiber must perform two tasks: (i) Imaging; and (ii) transport. For the imaging task (i) the modes at the distal end face (closest to the sample) of the multi-core fiber must lend themselves to coherent combination to intense foci for point-scanning imaging, and thus favors a multi-core fiber with a dense core layout; while for the transport, the main section of the multi-core fiber must be able to transport an ultra-short pulse distributed over all cores without deforming it through dispersion or changes induced by twists and bends, thus it favors a multi-core fiber with a sparse core layout. Therefore, to harmonize the conflicting demands for both dense and sparse core layout, we think of tapering the multi-core fiber, and thus decouple the end face dimensions from the dimensions of the main segment with the aim of simultaneously optimizing the multi-core fiber for transport and imaging.

This Chapter is organized as follows. First, in Section 4.2, we present the notion of tapering a multi-core fiber. In Section 4.3 we present a fast numerical model based on coupled-mode theory capable of predicting the essential properties of an arbitrarily tapered multi-core fiber from its structural parameters. In Section 4.4 we use this model to identify the design parameters that result in a chosen set of target properties. In Section 4.5 we report the fabrication and post-processing of the target designs. In Section 4.6 we present the optical characterization and validation of the fabricated designs. In Section 4.7 we present the implementation of the fabricated designs in the optical setup showing its experimentally measured imaging properties. Finally, in Section 4.8 we demonstrate the application of the fabricated tapered multi-core fibers in a two-photon lens-less endoscope system and quantify the gains in imaging performance.

This chapter is based on our publication [89].

4.2 Notion: Tapering multi-core fiber

Tapered optical fiber is the fiber whose diameter varies longitudinally along its optical axis. In general, taper profile is down-taper, which means that the diameter of the tapered fiber decreased from the proximal end to the distal

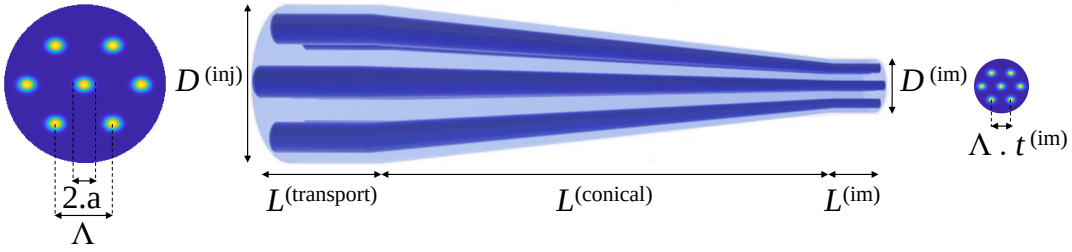

FIGURE 4.1: Sketch of tapered multi-core fiber, showing proximal and distal end faces where a is core radius and Λ the pitch size. Only seven of the N cores are represented for compactness.

end. Figure 4.1 presents a scheme of a tapered multi-core fiber. It starts with a uniform optical fiber with constant diameter $D^{(\text{inj})}$, referring to the proximal end where the beam on light is injected into the fiber, and length $L^{(\text{transport})}$ referring to the main segment that transport the light to the other end. Then the fiber's diameter decreases longitudinally within a length $L^{(\text{conical})}$, this segment is a conical taper called the taper transition, as it joins the main segment with the imaging segment of constant diameter $D^{(\text{im})}$ and length $L^{(\text{im})}$. All the structural parameters of the imaging segment such as outer diameter, pitch size and core radius are scaled by the factor of taper ratio $t^{(\text{im})} = D^{(\text{im})}/D^{(\text{inj})}$ relative to those of the transport segment.

4.3 Model

Numerically we model the tapered multi-core optical fiber by developing a code based on coupled-mode theory (CMT) and perturbation theory (presented in details in Chapter 1 Section 1.7.2), which we refer to as the "CMT model". In parallel, we developed a model based on the finite-element beam propagation method (FE-BPM) which we refer to as "the FE-BPM model".

In Section 4.3.1 we present the coupled-mode theory (CMT) method to model the tapered multi-core optical fiber. The input and output arguments of the Matlab function which implement the essential of the CMT model are detailed in Appendix A by Table A.2. In section 4.3.2 we present an overview of the Finite element beam propagation method to model the tapered multi-core fiber.

4.3.1 Coupled-mode theory model

In Chapter 1 Section 1.7.2, we presented the coupled mode theory to model a uniform multi-core fiber. This model returns the effective indices of the guided modes as well as its transmission matrix $\mathbf{H}$ which is represented by Equation (1.101).

In this section, we used the coupled-mode theory method to model a tapered multi-core fiber. In our model, we considered the tapered multi-core fiber as a concatenation of uniform segments. Therefore, the transmission matrix of the tapered multi-core fiber $\mathbf{H}^{(\text{taper})}$ is calculated as the product of uniform segments transmission matrices $\mathbf{H}_i$:

$$\mathbf{H}^{(\text{taper})} = \prod_i \mathbf{H}_i \tag{4.1}$$

The transmission matrix $\mathbf{H}^{(\text{taper})}$ is expressed in the basis of the fundamental modes of the N cores and is of dimension $N \times N$.

In Section 1.7.3, we present the calculation of the distal field from the transmission matrix of a multi-core fiber. Using Equation (1.104), we can compute the field in the far-field of the tapered multi-core fiber distal end face, by substituting the transmission matrix of the tapered multi-core fiber $\mathbf{H}^{(\text{taper})}$, thus

$$\mathbf{e}^{(\text{FF,pix})} = \mathbf{U}^\dagger \mathbf{H}^{(\text{taper})} \mathbf{e}^{(\text{prox,mode})} \tag{4.2}$$

Consequently, from this distal field, we can compute the properties of Strehl ratio and the memory effect. The Strehl ratio is a measure of the intensity in the focus and the memory effect is a measure of input-output angular correlations allowing distal point-scanning by proximal angular scanning [90].

The Strehl ratio S can then be defined as the ratio of the energy in the focus on far-field pixel j_0 to the total energy in the field (P is the set of far-field pixels within one $1/e^4$ half-width of far-field pixel j_0—where intensity is maximum):

$$S = \frac{\sum_{k \in P} |e_k^{(\text{FF,pix,j}_0)}|^2}{\sum_{k=1}^{N_{\text{pix}}} |e_k^{(\text{FF,pix,j}_0)}|^2} \tag{4.3}$$

The so-called "memory effect" is the effect by which the direction (phase ramp) of the output field changes by the same amount as the direction (phase ramp) of an input field [90]. In presence of the memory effect, it is therefore possible to displace a distal focus by simply adding a phase ramp to the proximal field. $\mathbf{p}(f_x^{(0)}, f_y^{(0)})$ is $N \times 1$ and its elements are the [complex exponential of] the additional proximal modal phases required to move the focus in the far-field by $(f_x^{(0)}, f_y^{(0)})$ using the memory effect:

$$\mathbf{p}(f_x^{(0)}, f_y^{(0)}) : p_k(f_x^{(0)}, f_y^{(0)}) = \exp(i2\pi f_x^{(0)} x_k^{(\text{core})} + i2\pi f_y^{(0)} y_k^{(\text{core})}) \tag{4.4}$$

The memory effect can then be quantified as a two-dimensional curve, the denominator contains the intensity of the field "optimally focused on far-field pixel j_1" cf Equation (1.107); and the numerator contains the intensity of the field "initially optimally focused on far-field pixel j_0 then shifted to far-field pixel j_1 using the memory effect":

$$M(f_x, f_y) = \frac{|e_{j_1}^{(\text{FF,pix},j_0 \to j_1)}|^2}{|e_{j_1}^{(\text{FF,pix},j_1)}|^2} \tag{4.5}$$

where "$\circ$" signifies Hadamard product (element-by-element multiplication) and

$$\mathbf{e}^{(\text{FF,pix},j_0 \to j_1)} = \mathbf{U}^\dagger \mathbf{H}^{(\text{taper})} [\mathbf{e}^{(\text{prox,mode},j_0)} \circ \mathbf{p}(f_x^{(0)}, f_y^{(0)})] \tag{4.6}$$

M is constant $= 1$ for "full" memory effect, and $= 0$ everywhere expect the origin for "no" memory effect.

4.3.2 Finite element method model

To accurately simulate the propagation of light in longitudinally varying waveguides, we used a homemade scalar wide-angle beam propagation method [91] based on a finite element method (FE-BPM) with first order elements.

We first designed the multi-core fiber cross-section in the transverse x–y plane by creating a non-uniform mesh of triangular elements. The field E_0 of the fundamental mode in one core was computed with a 1D-finite difference method and was interpolated on the structure of the multi-core fiber to obtain the E_{initial} matrix containing the fundamental mode field of one of the N cores of the multi-core fiber. Then we use our FE-BPM algorithm to propagate the field of each core individually along the z-direction with a step of 1 µm, and thus generate the E_{final} matrix at each propagation step. This is repeated for E_{initial} centered on each of the N cores. We compute the transmission matrix $\mathbf{H}$ by projecting the N resulting E_{final} on the non-orthogonal basis formed by the fundamental modes E_0 of the N cores, obtaining a $N \times N$ matrix in the core (fundamental mode) basis. When $E_{\text{final}} = E_{\text{initial}}$ for all cores, this means that core fields do not loose any energy during propagation and thus cross-talk in the multi-core fiber is zero, and $\mathbf{H}$ is diagonal. However, when cross-talk is non-zero, E_{final} differs from E_{initial} and thus $\mathbf{H}$ will contain some non-zero off-diagonal elements. Consequently, from $\mathbf{H}$ alone we are able to compute $\mathbf{X}$ by the same way mentioned in Section 1.7.3.

4.3.3 Validation of model

Unlike CMT, FE-BPM makes no prior assumptions on the modes of the multi-core fiber and so is generally the more accurate of the two. It is however much slower. Here, we have used the FE-BPM model as a "gold standard" against which we have compared the results of the CMT model. Consequently, we used the CMT model for the identification of the optimal design parameters.

In Figure 4.2(a) and Figure 4.2(b) we present cross-talk matrices for a $N = 475$ core uniform multi-core fiber as predicted by the CMT model and the FE-BPM model respectively. The two matrices look qualitatively and quantitatively similar. The cross-talk preferentially occurs between neighbor cores. Typically, in the modelled case there is significant cross-talk ($X_{ij} > -30$ dB) between cores up to 5Λ apart. However, the far cores have extremely low cross-talk, as seen in the southwest and northeast of the matrix which represent the cross-talk between the middle cores and the extreme cores.

Moreover, in Figure 4.3 we present the comparison of the average total cross-talks X_{ave} predicted by the two models as a function of wavelength, again displaying agreement. From this comparison we establish the accuracy of the CMT model up to average total cross-talk of at least X_{ave} = -2 dB and down to effective indices 0.8e-3 above the cladding index.

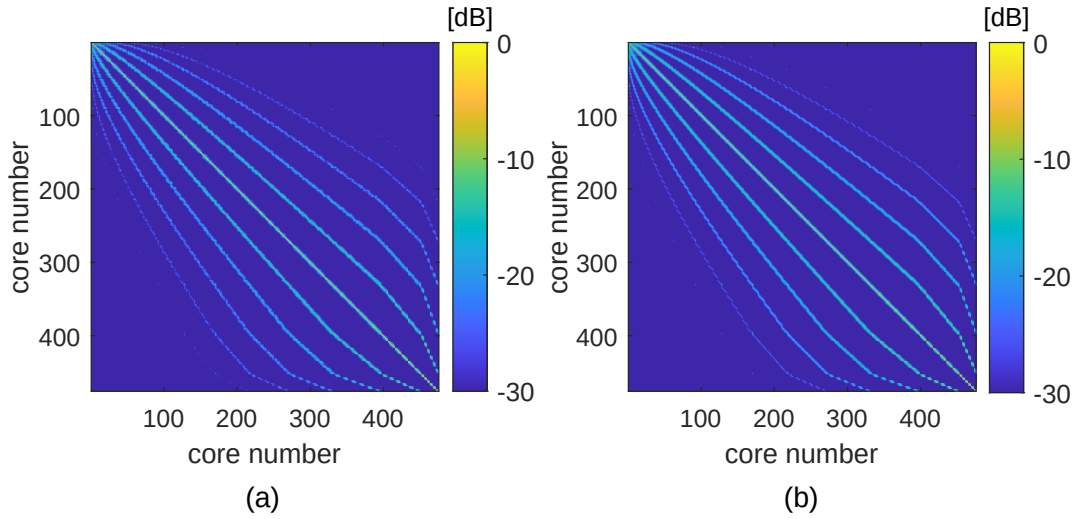

FIGURE 4.2: cross-talk matrix $\mathbf{X}$ of a uniform multi-core fiber segment computed by (a) CMT model; and (b) FE-BPM model at 800 nm. Core numbering convention, the center core is number 1, the six cores in the first hexagonal ring are 2–7, etc. Simulation parameters: $L = 5$ mm; $N = 475$; $\Lambda = 7.5$ µm; $a = 1.4$ µm.

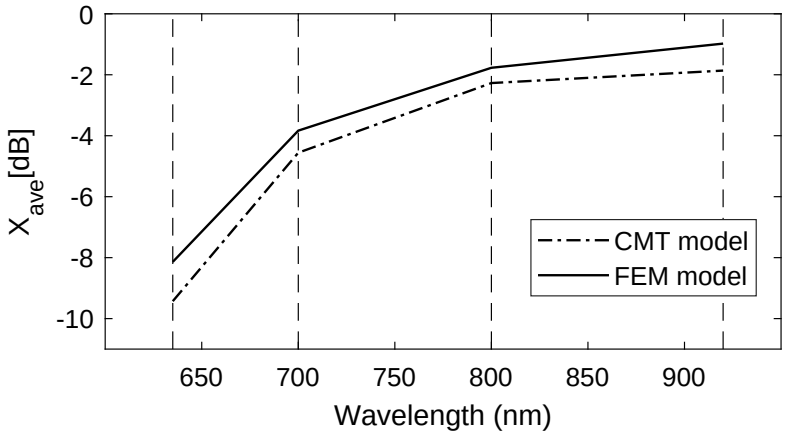

FIGURE 4.3: The average total cross-talks X_{ave} predicted by CMT model (dash-dotted line) and FE-BPM (solid line) as a function of wavelength

4.4 Design

As indicated in Section 4.3.1, the CMT model can be used to predict the properties of tapered multi-core fiber from its structural properties. And thus it can be used to identify the tapered multi-core fiber designs that result in a chosen set of properties.

We used the CMT model to identify the design parameters of an optimized tapered multi-core fiber with triangular core layout with suitable properties for two-photon lens-less imaging with a pulsed 920 nm excitation laser. As we are dealing with imaging optical fiber, we are concerned in design of the three main parts in the fiber which are (i) the injection segment where laser beam is injected into the fiber through it, (ii) the transport segment which is responsible of transporting (or transmitting) the laser beam from input to the output of the fiber, and (iii) the imaging segment from where laser beam is emerged to image the sample. In the following sections, we present the design parameters for optimizing the three segments to form together an optimized imaging multi-core fiber.

4.4.1 Transport segment

Firstly, the transport segment of the multi-core fiber should exhibit minimal coupling between multi-core fiber cores (inter-core coupling), and this is important to assure that light injected into one core remains confined to only that core during propagation through the multi-core fiber. Another important consequence of low inter-core coupling is to preserve a significant property in multi-core fiber which is the memory effect. The existence of memory effect is of primordial importance for two-photon point-scanning imaging as will be shown in the coming sections. The inter-core coupling is a function of several multi-core fiber parameters, the most important one is the distance between cores which is well known as the pitch size Λ. Therefore, in the following sections we will show the criterion to choose fiber parameters in order to design a transport segment with low coupling between cores.

Moreover, the transport segment of the multi-core fiber here should transport an ultra-short pulse distributed over all cores without deforming it through dispersion or non-linearity. And the major form of dispersion in multi-core fiber transporting pulsed laser is the inter-core group delay dispersion. This dispersion arises from uncorrelated variations in core diameters along the length of the multi-core fiber. So as first step, we wanted to minimize the inter-core group delay dispersion, to allow the simultaneously launched sub-pulses to arrive at the distal end of the fiber synchronously.

Inter-core group delay dispersion

The inter-core group-delay dispersion (GDD) is directly proportional to the derivative of the group index with respect to core radius $\mathrm{d}n_g/\mathrm{d}a$. Variation can be hypothesized to appear during all fabrication steps: from the deposition of the doped silica during the preform fabrication up to the final fiber draw (more details in Section 4.5.1). Even in the case of an ideal stack, its draw

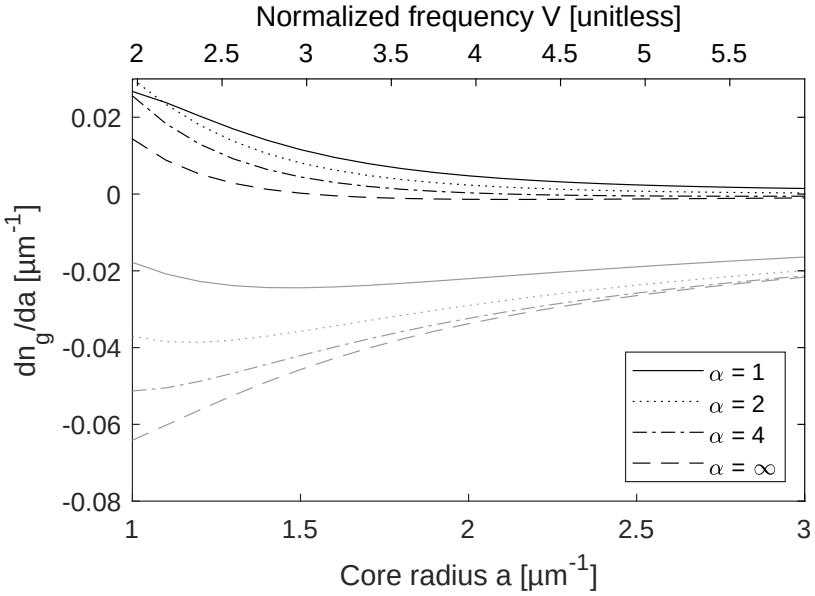

FIGURE 4.4: Calculated derivatives of the group delay vs. core radius for the four combinations of index profile (step and parabolic) and origin of core radius variation (black curves correspond to (i) uneven drawing speed and grey curves to (ii) uneven heating) as described in the text. The parameters of the calculation were taken similar to the experimental parameters in the main article.

can lead to small transverse variations between cores from at least two possible origins: (i) uneven drawing speed; (ii) uneven heating. In case (i) core radii a vary while the maximum core refractive indices n_1 are preserved; in case (ii) core radii a vary while maximum core refractive indices vary as a^{-2} as dopant quantity is preserved in a transverse plane. The impact of (i) and (ii) are predicted for four different initial index profiles with grading parameters $\alpha =$ 1, 2 (parabolic), 4, and ∞ (step). Effective indices of the fundamental mode are calculated by a scalar mode solver as a function of wavelength λ and core radius a. Group indices are then calculated using Equation (1.26), from which the sought derivative $\mathrm{d}n_g/\mathrm{d}a$ is subsequently calculated numerically.

Calculated derivatives are presented in Figure 4.4 for four different grading parameters ($\alpha = 2$, parabolic-index fiber; $\alpha = \infty$, step-index fiber). The results permit to conclude that a step-index profile eliminates inter-core group-delay dispersion ($\mathrm{d}n_g/\mathrm{d}a = 0$ for $V = 3$—dashed line) but under the condition that (i) is the physical origin. If (ii) is the origin the step index profile is the worst (dash-dotted line). In practice, it is known than dopant does diffuse during fiber drawing, effectively smoothing refractive index profiles in the process. This is particularly marked for the small core diameters relevant for the present study [83]. It is then to be expected that an initial step-index profile in the pre-form evolves toward a gaussian profile during drawing. The black and grey dotted lines in Figure 4.4 show curves for case (i) and (ii) for parabolic index profile (a parabolic profile can be thought of a second-order approximation of a gaussian profile). As shown by Figure 4.4, these curves converge uniformly toward zero

for increasing core radius. According to this example, the trend is that inter-core group-delay dispersion (of the fundamental mode) is reduced with bigger core radius.

Consequently, we identify the rule-of-thumb that inter-core group delay dispersion decreases with increasing V-parameter. This holds for all the hypothesized physical origins that is considered in the above section and in Refs. [92, 93, 94]. We therefore choose to constrain the V-parameter to around 5.06, which represents the second cutoff of a parabolic-index core, thus making the core bi-mode. We choose this V value to compromise between low group delay dispersion and only the second order mode is guided, but not other higher-order modes.

Refractive-index difference and core radius

The core-cladding index contrast, which is called the refractive index step Δn, should generally be chosen as high as practically possible, for its role in obtaining tighter mode confinement and higher NA which in its turn increases the light collection efficiency of the fiber. Therefore, we choose $\Delta n = 0.03$.

Then, to conserve $V = 5$ for a 920 nm wavelength laser beam, the radius must then be chosen $a = 2.5$ µm, calculated by Equation (1.22).

Pitch size

As mentioned in the introduction of this chapter, the main segment of the multi-core fiber which is the transport segment favors multi-core fiber with sparse core layout. This will makes the fiber non-sensitive to twists and bends as we aim to invariant transmission matrix to assure flexible operation.

The most important criterion on the pitch size is that there should be very low cross-talk ($<$ -30 dB) in one metre of un-tapered (uniform) multi-core fiber. Therefore, to choose the pitch size, we used the CMT model to compute the average total cross-talk XT_{ave} in one meter of multi-core fibers with different pitch sizes. Taking in to account that a sparse core layout with around 12–15 µm core separation is better suited as mentioned in Refs. [67, 49, 82]. Consequently, as shown in Figure 4.5 we predict that the chosen criterion on XT_{ave} is respected for $\Lambda > 14$ µm. Where the predicted X_{ave} = -62 dB per meter in the uniform segment.

Cores number and fiber diameter

The number of cores may be chosen arbitrarily, generally "the more the better" as the number of resolvable image pixels is proportional to N (as described in Section 2.1.5). Other than that N only impacts on the outer diameter of the transport section, so it can be chosen so as to respect a chosen condition on the outer diameter. Here, we choose $N = 349$, resulting in an outer diameter $D^{(\text{transport})} = 330$ µm.

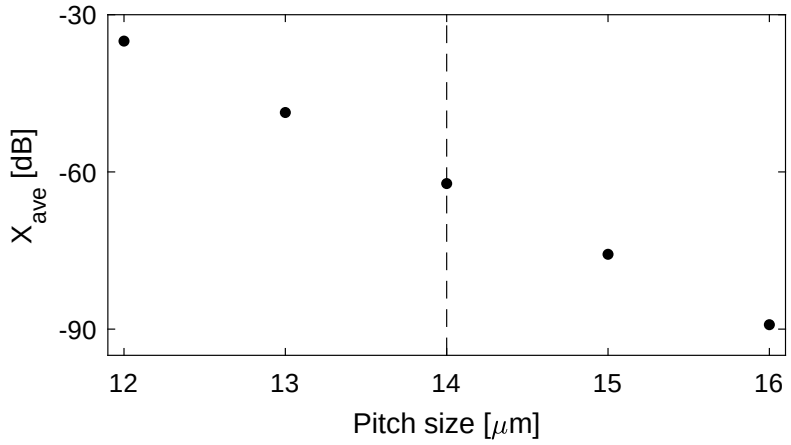

FIGURE 4.5: XT_{ave} in one meter multi-core fibers with for different pitch sizes

4.4.2 Injection segment

The injection segment is where beam of light is injected to the fiber cores. Hence, its the best candidate to be used as a mode filter. Therefore, to avoid exciting the higher-order mode in the transport segment, we decide to taper a short length of the fiber at the launch end until the V value is locally brought below the single mode cutoff ($V_{\text{cutoff}} = 3.518$). Allowing a pure fundamental mode to be launched into each core. Since the fundamental mode offers a better focusing performance when compared to the higher-order modes, and its propagation is effective for synchronized arrival times.

Consequently, we obtain "injection" segment separated from the transport segment by a conical taper whose dimensions are scaled by the factor $t^{(\text{inj})} = 0.6$ resulting in $V = 3.0$ which is comfortably below the single-mode cutoff. The predicted average total cross-talk in the injection segment with $t^{(\text{inj})} = 0.6$ is X_{ave} = -26 dB.

4.4.3 Imaging segment

The final and the most important step in the design, is to choose the dimensions of the imaging segment, where all its structural parameters are scaled by the factor $t^{(\text{im})}$ relative to those of the transport segment.

The imaging segment as its name indicate is the segment which is responsible of the imaging task and its design is what define the imaging properties. And here we are mainly interested in two properties, which are : the Strehl ratio and the Memory effect. Therefore, we are particularly interested in two values of $t^{(\text{im})}$, a first one which maximizes the Strehl ratio under the condition that the "full" memory effect is conserved; and a second one which maximizes the Strehl ratio without any conditions on the memory effect. But in this case a new condition must be respected, that core guidance is maintained, i.e. the effective indices of all modes must remain comfortably above the cladding index so as not to be too close to the single-mode cutoff.

In the following sections, we will present the imaging properties predicted by the CMT model, in order to identify the value of $t^{(\mathrm{im})}$ that attain the above requirements.

Predicted imaging properties

Point-spread function

To plot the distal focus, we reshape the complex field optimally focused on the central far-field pixel (Equation (1.107)) in to 2D image in the far-field pixel basis. Consequently, we obtain the point-spread function (PSF) at a distance Z from tapered multi-core fiber distal end. The image is the convolution of the object with the PSF, so obviously we are interested in having a PSF which is as singly peaked as possible to enhance image quality. However, the point-spread function of a hexagonal multi-core fiber consists of a central spot surrounded by periodic replica, and this arises from the periodicity of the core layout. As shown by Figure 4.6, tapering the imaging segment of the multi-core fiber makes the point-spread function become more singly peaked.

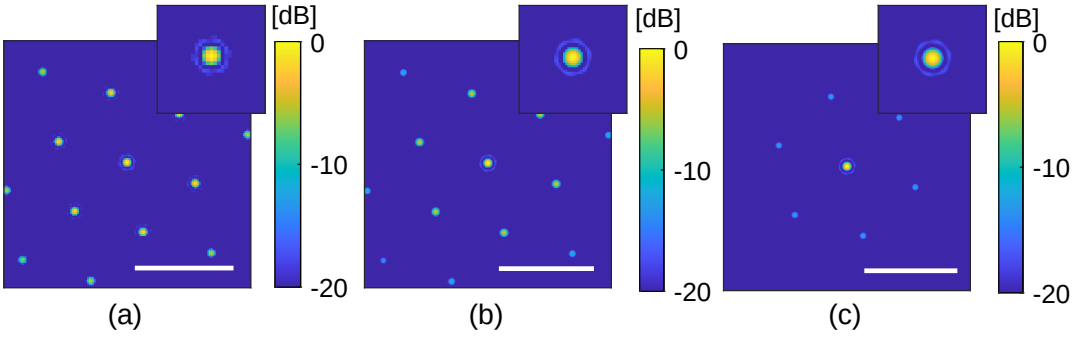

FIGURE 4.6: Point-spread function predicted by CMT model for (a) $t^{(\mathrm{im})} = 1.0$, (b) $t^{(\mathrm{im})} = 0.6$, and (c) $t^{(\mathrm{im})} = 0.4$ in a plane $Z = Z_0 \cdot t^{(\mathrm{im})}$. Each image is normalized to its maximum intensity. Scale bar in all images is 50 μm. Insets, 7× zoom on the central spot.

Figure 4.6(a)-4.6(c) present the predicted point-spread functions (PSF) at distance $Z = Z_0 \cdot t^{(\mathrm{im})}$ from the distal end of multi-core fibers with $Z_0 = 500$ μm and $t^{(\mathrm{im})} = 1$, 0.6, and 0.4 (*per se* they are far-field images scaled by $x = f_x Z\lambda$, $y = f_y Z\lambda$). It comprises a central spot surrounded by a dimmer periodic replicas for untapered multi-core fiber ($t^{(\mathrm{im})} = 1$). However, it becomes more singly-peaked, very beneficial for image quality, as the taper ratio decreases while the width of the mode profile is virtually unaltered. Also the focal spot size which is presented by the full-width at half-maximum (FWHM) of the PSF is fairly constant equal to 2.4 μm with decreasing taper ratio.

Memory effect

We compute the memory effect by the CMT model using Equation (4.5). Figure 4.7 presents the memory effect curves for different taper ratios $t^{(\mathrm{im})}$. The curves $t^{(\mathrm{im})} = 1$ and 0.6 are coincident and constant equal to 1, which means

conservation of full memory effect. However, the curve $t^{(\mathrm{im})} = 0.4$ is strongly peaked around $x = 0$ and then drops to zero, which denote an almost complete absence of the memory effect. Therefore, lowest value of $t^{(\mathrm{im})}$ which can be retained as a design parameter for which memory effect is "fully" conserved is 0.6.

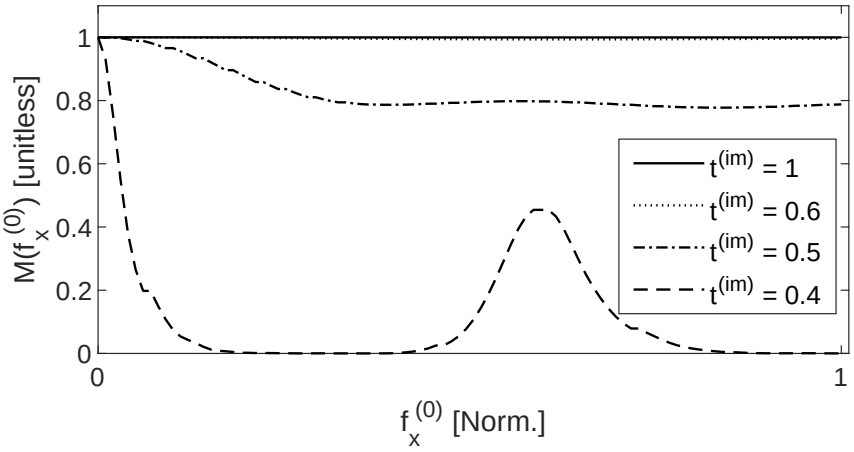

FIGURE 4.7: Memory effect curves predicted by CMT model for multi-core fibers with different taper ratios.

Strehl ratio

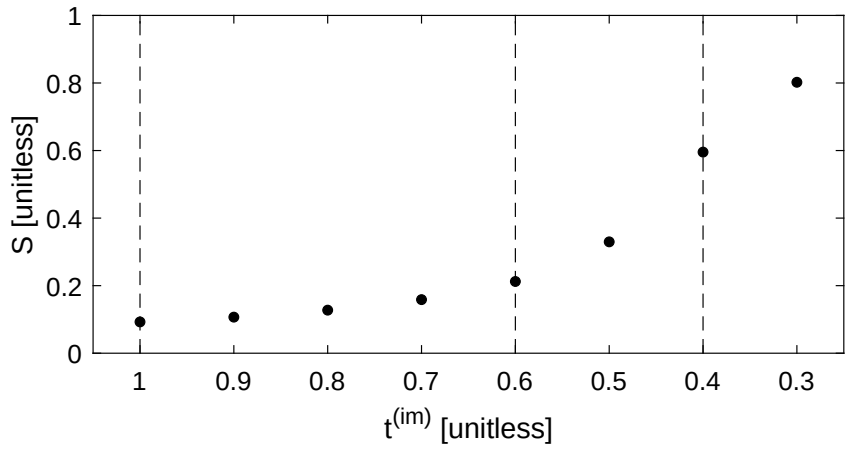

FIGURE 4.8: Strehl ratio of multi-core fibers with different taper ratios predicted by CMT model.

The predicted Strehl ratios are computed from Equation (4.3). Figure 4.8 present the Strehl ratios for different taper ratios $t^{(\mathrm{im})}$. As clearly shown, the Strehl ratio shows a dramatic increases as we decrease the taper ratio $t^{(\mathrm{im})}$. It starts with 9 % at $t^{(\mathrm{im})} = 1$ (untapered fiber) and increases to reach a maximum of 80 % at $t^{(\mathrm{im})} = 0.3$. However, as mentioned in the introduction of this section, we are looking for $t^{(\mathrm{im})}$ parameters that obtain a maximum Strehl ratio while conserving core guidance. Therefore, we plot in Figure 4.9 the predictions of

effective indices for different taper ratios $t^{(\mathrm{im})}$. Which shows that at $t^{(\mathrm{im})} = 0.3$ some of the indices drop below the cladding index (lower dashed line) making leaking to cladding modes inevitable. For this reason, the lowest value of $t^{(\mathrm{im})}$ that can be retained as design parameter is 0.4 for which it maximize the Strehl ratio while effective indices remain $2{\cdot}10^{-3}$ above the cladding index.

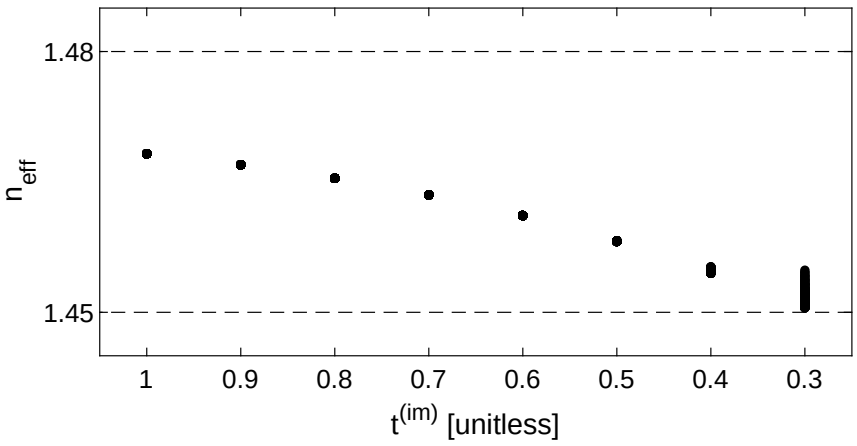

FIGURE 4.9: Effective indices of supermodes of multi-core fibers with different taper ratios.

4.4.4 Sketch of design

Based on the above sections, we realized a multi-core fiber comprising three segments comprising "injection", "transport", and "imaging" segments joined by conical tapers. Figure 4.10 represents a sketch of the designed multi-core fiber. From the left, it start with an injection segment of constant diameter $D^{(\mathrm{inj})}$ and length $L^{(\mathrm{inj})}$, then first conical segment of length $L^{(\mathrm{conical},1)}$, then a transport segment of constant diameter $D^{(\mathrm{transport})}$ and length $L^{(\mathrm{transport})}$, a second conical segment of length $L^{(\mathrm{conical},2)}$, and finally it end up with an imaging segment of constant diameter $D^{(\mathrm{im})}$ and length $L^{(\mathrm{im})}$. All the structural parameters of injection segment are scaled by the factor $t^{(\mathrm{inj})}$ relative to those of the transport segment, with

$$t^{(\mathrm{inj})} = \frac{D^{(\mathrm{inj})}}{D^{(\mathrm{transport})}} \tag{4.7}$$

And all the structural parameters of imaging segment are scaled by the factor $t^{(\mathrm{im})}$ relative to those of the transport segment, with

$$t^{(\mathrm{im})} = \frac{D^{(\mathrm{im})}}{D^{(\mathrm{transport})}} \tag{4.8}$$

4.5 Fabrication

We fabricated a multi-core fiber to the specification requirement of the transport segment identified in Section 4.4.1 ($\Delta n = 30{\cdot}10^{-3}$; $\Lambda = 14$ µm; $a = 2.5$ µm;

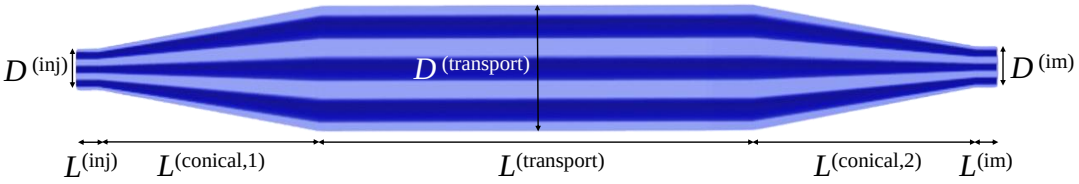

FIGURE 4.10: Sketch of tapered MCF.

$N = 349$) by the stack-and-draw process. Then we post-processed the uniform multi-core fiber to obtain the tapered multi-core fiber represented by Figure 4.10 by tapering a short length at the terminals of the multi-core fiber using a CO_2 laser-based glass processing and splicing system. The two steps of fabrication process are presented in details in the following sections.

4.5.1 Fiber drawing: stack-and-draw process

The stack-and-draw technique has become the preferred fabrication technique in recent years, where it allows versatile and flexible manufacture. The main concept of the stack-and-draw process is creating a macroscopic version of the fibre design before drawing it down to the required microscopic size.

Multicore optical fibers are usually manufactured in three main steps, (i) fabricating fiber preform, (ii) stacking doped rods and filling rods inside a jacketing tube, (iii) drawing the fiber with a high-temperature furnace in a tower setup.

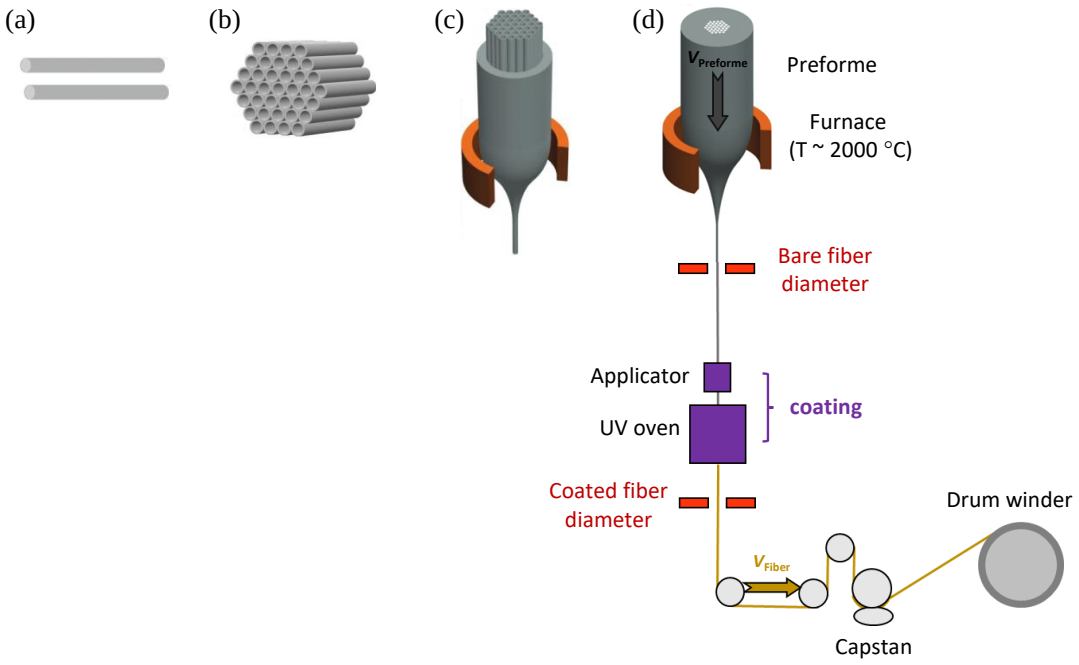

FIGURE 4.11: (a) Prepare Ge-doped silica rods (b) Stack rods in hexagonal (c) draw the canes (d) draw the fiber

Figure 4.11 sketches the fabrication process of the multi-core fiber showing all steps. The first stage in fabricating a multi-core fibre is drawing the doped

rods which will create the individual cores within the fiber. Therefore, a germanium doped silica preform with a parabolic index profile (maximal index contrast of $30 \cdot 10^{-3}$ compared to its silica cladding) has been drawn into hundreds of rods of 1.46 mm diameter with a doped diameter of about 0.52 mm. These rods were then stacked manually on a hexagonal lattice and jacketed into a silica tube of 34 mm outside diameter. This assembly containing the 349 cores was then drawn at about 2000 $°C$ into canes of about 5 mm while applying a vacuum inside the jacketing tube to collapse the interstitial holes between the rods constituting the stack. Finally, one of these canes was drawn into a 330 µm fiber at 1990 $°C$ with relatively slow speed (feed rate of 5 mm/min for a drawing speed of 12 m/min). In the final stage a coating is added to the outside of the fibre To protect the bare fiber from contaminants and scratches, making the fibre more durable.

4.5.2 Fiber post-processing: Tapering

Tapering an optical fiber is achieved by the combined local heating of the fiber and simultaneously applying a pulling force lengthwise on the fiber to obtain a fiber whose diameter varies longitudinally.

Traditionally tapering fibers was done by the "flame-brush" method [95] which typically utilize a flame fed by oxygen and butane moving forward and backward over a certain length of the fiber to heat it while two motorized stages pull the fiber ends in opposite directions along its axial length. Later on, another heat source is used to taper fibers, such as electrical resistance elements [96], which uses a resistive material and running a controlled current through it to reach a certain temperature. These resistive materials are then used to create furnaces in which the fiber will be tapered.

Currently, the state-of-the-art method for tapering fibers is the CO_2 laser-based glass processing and splicing system (LZM-100 FUJIKURA). The heat source in this method is the carbon dioxide laser, where heating the fiber is based on the fiber's absorption of the power emitted by the laser. This method provides extremely stable operation that allows control over a wide range of parameters.

The tapering process is achieved by a combined local heating of the fiber by CO_2 laser beam and simultaneously applying a pulling force lengthwise on both ends of the fiber. Once tapering process ended, we obtain a bi-conical tapered optical fiber connected with the waist as shown by Figure 4.12 . Then we remove the fiber carefully, and we cleave it using CT-106 FUJIKURA cleaver in the middle of the waist (dashed line in Figure 4.12), and thus we obtain two pieces, one long piece of an optical fiber with adiabatic taper at one end, and this is the target taper. And the second (15 cm) whose cleaved end is measured under a microscope to check whether the cleave is clean after which it is discarded. Then we repeat the same process on the un-tapered side of the realized tapered fiber, and thus to obtain a double tapered multi-core fiber as shown in Figure 4.10.

Specific details of the process are given in the following. The parameters of the target profile, a bi-conical taper, is specified in the fiber processing software

which controls the LZM-100. Figure 4.12 is a screenshot from the software giving an example of such a profile and the parameters that can be set to define it. From this, the software automatically calculates the tension and pulling speed to be applied by the stepper motors of the LZM-100.

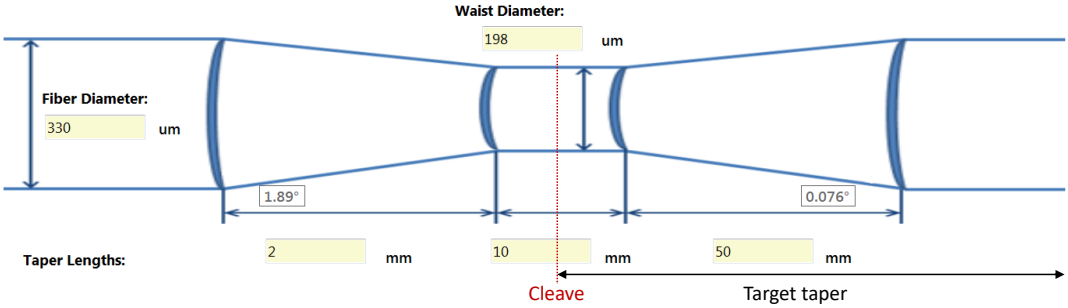

FIGURE 4.12: Screenshot from the fiber processing software showing the target profile and the parameters that can be entered. The dashed vertical line indicated the point where the bi-conical taper is cleaved after processing to yield one extremity (either the injection or the imaging segment) of the final tapered multi-core fiber. The given example is for a taper ratio of 0.6.

Before the multi-core fiber is placed in the LZM-100 the polymer coating is completely removed over the length of the multi-core fiber, this is an essential step especially for the area that will be exposed to laser beam, using a razor blade and cleaned using a tissue soaked with isopropanol or ethanol. Then fiber is fixed in the LZM-100 by clamping its terminals by fiber holders chosen with sizes appropriate to the fiber diameter. These holders are based on the stepper motors that will apply the pulling force lengthwise on both ends of the fiber. Fibers are also fixed tightly using a split v-groove clamps placed on the left and right of the laser source, these v-groove clamps are automatically adjusted to fiber diameter.

The tapering process typically takes 200 s. When it is finished the software can measure the actual profile using the internal cameras of the LZM-100 and create a report in Excel format containing the target profile and the measured profile. We usually start with a test draw to check the fineness of automatically calibrated parameters. From data in the extracted report, if the curve of measured profile is above the target, then laser heating power is insufficient. If measured curve exhibits large ripple, then laser heating power is excessive. In both cases, we should manually modify some of power parameters by increasing (case of insufficient heating power) or decreasing (case of excessive heating power) their values by small percentage, until we identify the optimal power for obtaining the target profile.

The CO_2 laser-based glass processing and splicing system provides extremely stable operation and allows control over a wide range of parameters to achieve the tapered multi-core fibers precisely with the chosen design parameters. Table 4.1 present the physical dimensions of the fabricated tapered multi-core fiber samples.

Additionally, microscope images were acquired of the distal end faces of the fabricated tapered fibers i.e. their imaging segment. Figure 4.13 shows the

Identifier	0	1	2
$D^{(\text{inj})}$ [µm]	196	194	196
$t^{(\text{inj})}$	0.6	0.6	0.6
$L^{(\text{inj})}$ [m]	0.005	0.005	0.005
$L^{(\text{conical},1)}$ [m]	0.025	0.025	0.025
$D^{(\text{transport})}$ [µm]	330	330	330
$L^{(\text{transport})}$ [m]	0.23	0.21	0.24
$L^{(\text{conical},2)}$ [m]	0	0.05	0.05
$D^{(\text{im})}$ [µm]	330	199	135
$t^{(\text{im})}$	1	0.6	0.4
$L^{(\text{im})}$ [m]	0	0.005	0.005

TABLE 4.1: The physical dimensions of the fabricated tapered multi-core fiber samples.

microscope images of the distal end faces of the three tapered multi-core fibers with parameters as in Table 4.1 as well as the measured values of their diameter $D^{(\text{im})}$; pitch Λ; and core radius a.

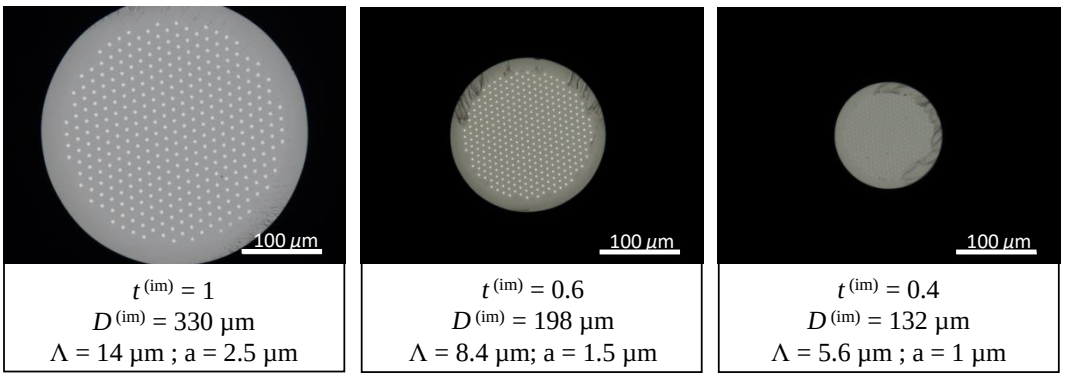

FIGURE 4.13: Distal end faces of the tapered multi-core fibers from Tab. 4.1 with taper ratios $t^{(\text{im})} = 1$, 0.6 and 0.4. All images are on the same scale. $D^{(\text{im})}$, diameter of imaging segment. Λ, pitch and core radius a in the imaging segment.

4.6 Characterization: Optical properties

After fabricating the tapered multi-core fiber, we characterized its optical properties to validate them with the properties predicted by the CMT model. So we build a simple optical setup and characterize the tapered multi-core fiber using a super-continuum laser source. Using this setup, we first confirm that these

tapered multi-core fibers are effectively single mode, then we measure the mode field diameter of the fundamental mode, and finally we measure the inter-core cross talk between multi-core fiber cores.

4.6.1 Optical setup

The experimental setup is schematically described in Figure 4.14. We used super-continuum laser source (YSL Photonics SC-PRO). Both proximal and distal ends of the double tapered multi-core fiber are fixed on XYZ translation stages. Neutral density filter (NDF) is used to prevent the camera from saturation. The laser beam entering the proximal end of the multi-core fiber is focused by an aspheric lens L_1 with focal length 4.03 mm into one core at a time. We use the XYZ translation stage to move the focus from core to core. The emerging light at the distal end of the fiber is imaged with aspheric lens L_2 of 4.51 mm focal length onto a monochrome CMOS camera (Thorlabs, DCC1545M). A bandpass filter (FB900-10) is placed in front of the camera in order to measure the tapered multi-core fiber properties at a wavelength of 900 nm.

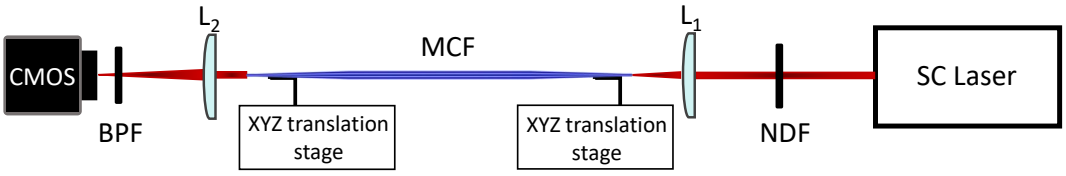

FIGURE 4.14: Experimental setup for measuring optical properties of tapered multi-core fiber. SC Laser, super-continuum laser source (YSL Photonics SC-PRO); NDF, neutral density filter; L1, lens with focal length 4.05 mm; multi-core fiber, tapered multi-core fiber; L2, lens with focal length 4.51 mm; BPF, band-pass filter (Thorlabs, FB900-10); CMOS, CMOS camera (Thorlabs, DCC1545M).

Single-mode guidance

All tested tapered multi-core fibers were tapered at the proximal end with $t^{(\mathrm{inj})} = 0.6$ to assure injection into only the fundamental mode of each core. To confirm that the tapered multi-core fibers were effectively single-mode with the choice of injection segment parameters, we tested a long multi-core fiber ($L^{(\mathrm{transport})} > 1$ m) with $t^{(\mathrm{inj})} = 0.6$ and $t^{(\mathrm{im})} = 1$. On the camera we visualized the intensity profile exiting one core and verified that it did not change while applying a perturbation on the fiber. This verifies that only the fundamental mode propagates through the transport segment despite it being bi-modal, thus the injection segment allows the selective excitation of only the fundamental mode of each core.

Mode field diameter

We injected the focused laser beam into multi-core fiber cores in the injection segment successively, and imaged the emerging beam out of imaging segment on a camera in the far field. The recorded images are composed of a gaussian-like spot which corresponds to the intensity profile of the fundamental mode of the injected core as shown by Figure 4.15(a). We treat this image and plot the data of a horizontal line passing through its center which gives the dotted curve presented in Figure 4.15(b) which coincide with the Gaussian fit curve (red). This curve is the intensity profile of the mode along the radial distance. Then the mode field diameter (MFDs) of the fundamental mode is measured as the full-width of the intensity profile at $1/e^2$ of its maximum. In Figure 4.15(b), the black horizontal line represent the $1/e^2$ of the maximum intensity, then the MFD is the distance between the intersection of the black line with the intensity curve.

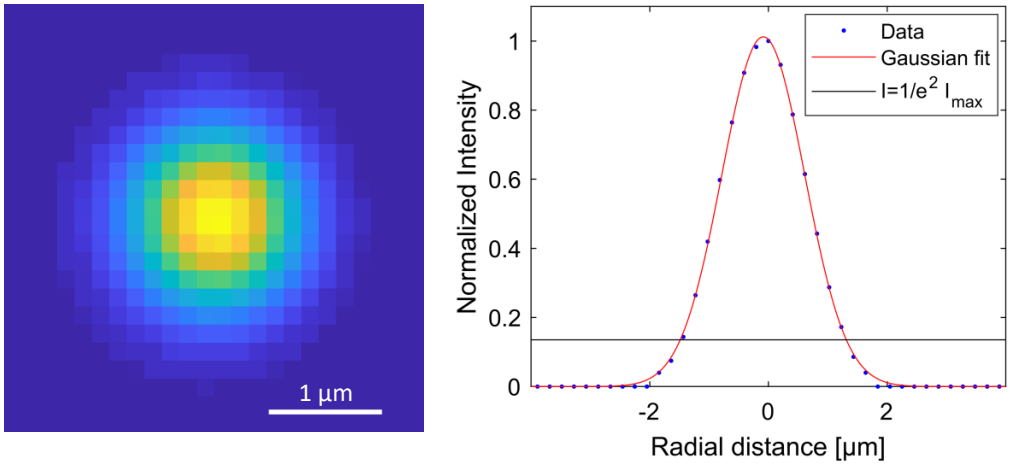

FIGURE 4.15: (a) Mode profile of one excited core in a tapered multi-core fiber with $t^{(\mathrm{im})} = 0.6$. (b) The intensity profile of fundamental mode.

Consequently, we could measure the mode field diameter (MFD) of the visualized mode profile for each $t^{(\mathrm{im})}$ and confirm the agreement with the predictions of the CMT model. as shown in Table 4.2. Noting that the reported $\mathrm{MFD}^{(\mathrm{exp})}$ values represent an average of MFDs calculated for multiple cores.

MCF sample	$t^{(\mathrm{im})} = 1$	$t^{(\mathrm{im})} = 0.6$	$t^{(\mathrm{im})} = 0.4$
$\mathrm{MFD}^{(\mathrm{sim})}$ [µm]	3.2	2.5	2.4
$\mathrm{MFD}^{(\mathrm{exp})}$ [µm]	3.6	2.8	2.3

TABLE 4.2: The MFDs of the tapered multi-core fiber samples predicted by CMT model ($\mathrm{MFD}^{(\mathrm{sim})}$) and experimentally measured ($\mathrm{MFD}^{(\mathrm{exp})}$).

Inter-core cross-talk

To measure the inter-core cross-talk in the tapered multi-core fiber samples, we injected the focused laser beam into multi-core fiber cores in the injection segment once at a time. In the absence of cross-talk the recorded images are composed of the intensity profile of the fundamental mode of the injected core. However, if a number of additional spots show up in the recorded image this means that injected light is no more confined in single core while propagating through the tapered fiber, however it spread to other cores.

Experimentally, the cross-talk matrix $\mathbf{X}$ is measured as follows. The intensities I_j of the spots are measured from the image. The i'th line of $\mathbf{X}$ is $X_{ij} = I_j / \sum_j I_j$ where i is the number of the core one is injecting into. This is repeated for all cores $1 \leq i \leq N$ to construct the full cross-talk matrix. In practice the full measurement of $\mathbf{X}$ is extremely tedious and time consuming. A measure of the average total cross-talk X_{ave} is more useful for comparing with the predictions of the CMT model. It can be estimated by measuring X_{ij} for a small number N_{red} of randomly chosen core numbers i and then calculating by the appropriately modified Equation (1.103).

$$X_{\text{ave}} = \frac{1}{N_{\text{red}}} \sum_i \left(\sum_{j \neq i} X_{ij} \right). \tag{4.9}$$

As shown by the Figure 4.16, the average total cross-talk X_{ave} measured experimentally (empty circles) agrees reasonably with the predicted values (filled circles).

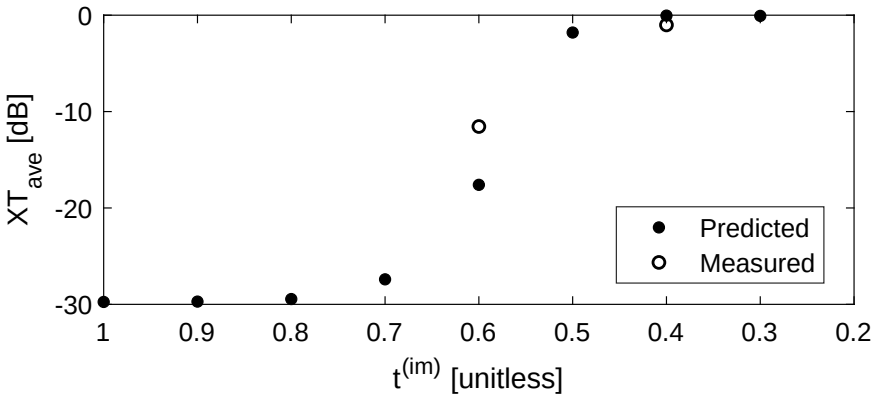

FIGURE 4.16: The average total cross-talk X_{ave} predicted by CMT model (full circle) and measured experimentally (empty circle) for multi-core fibers with different taper ratios.

4.7 Implementation

As a first step towards implementing the tapered multi-core fibers in a lensless endoscope system we measured the transmission matrix and the imaging properties of the fabricated tapered multi-core fibers.

4.7.1 Transmission matrix measurement

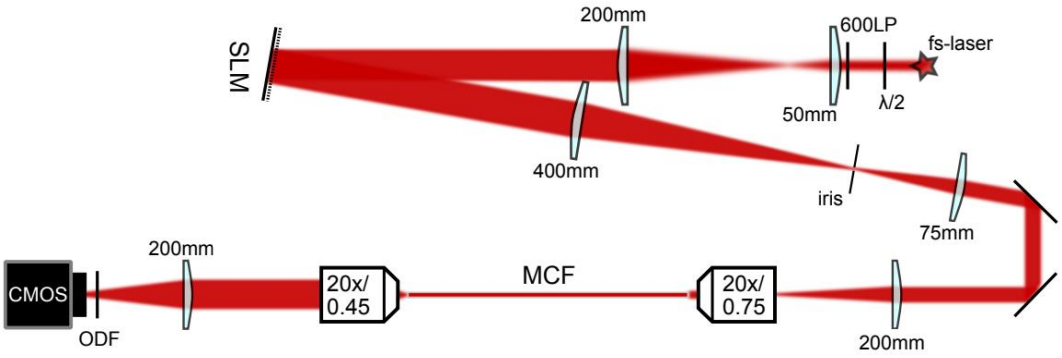

FIGURE 4.17: lens-less endoscope setup used to characterize the transmission matrix, memory effect, Strehl ratio etc. of the tapered multi-core fibers.

The experimental setup is sketched in Figure 4.17. We used a pulsed fs-laser (Chameleon Ultra II, Coherent) tuned to 920 nm wavelength. It has a repetition rate of 80 MHz and 150 fs pulse length. The laser beam is expanded by a keplerian telescope with a magnification of 4 to fill the active area of the spatial light modulator (SLM) (X10468-07, Hamamatsu). As in Ref. [67] the SLM is used for multiple purposes, mainly to phase the individual fiber cores to form a coherent focus for nonlinear imaging. However, it serves equally to create the micro-lens array for efficient light coupling into the individual fiber cores of the multi-core fiber (Figures 4.18(a), 4.18(e)), and is used as a selective blazed grating that allows to individually switch on fiber cores for the measurement of the transmission matrix. To ensure the unused parts of the SLM are not coupled in the fiber, an iris is used to cut off the 0th order of this blazed grating, and so only the deflected light in the 1st order passes Figure 4.18(e). The half-wave plate ($\lambda/2$) before the telescope rotates the linear polarization to match the orientation of the extraordinary axis of the SLM which is horizontal in the given setup. The combination of the following three lenses (400 mm, 75 mm and 200 mm) and the microscope objective (CFI Plan Apo, 20× / NA 0.75, Nikon) ensures to demagnify the hexagonal tiling from the SLM to the proximal end of the fibers. Thus, the system magnification is $M_{\text{sys}} = 400/75 \cdot M_{\text{obj}} = 400/75 \cdot 20 = 106.67$. This allows to space the SLM such that 169 cores of the multi-core fiber can be addressed for incoupling. In order to measure the transmission matrix of the multi-core fiber, the emerging light at the distal end of the fiber is imaged with an objective (LUCPlanFLN, 20× / 0.45 NA, Olympus) and the tube lens of 200 mm focal length onto a standard CMOS camera (BFLY-U3-23S6M-C, FLIR). Optical density filters (ODF) prevent the camera from saturation.

In this work, we use TM as shorthand for a subset of the full transmission matrix. The full transmission matrix would contain four quadrants corresponding to the four combinations of input and output polarizations; and all elements would be complex ie comport an amplitude and a phase. The TM measured here is strictly speaking the "complex exponential of the phases of one quadrant

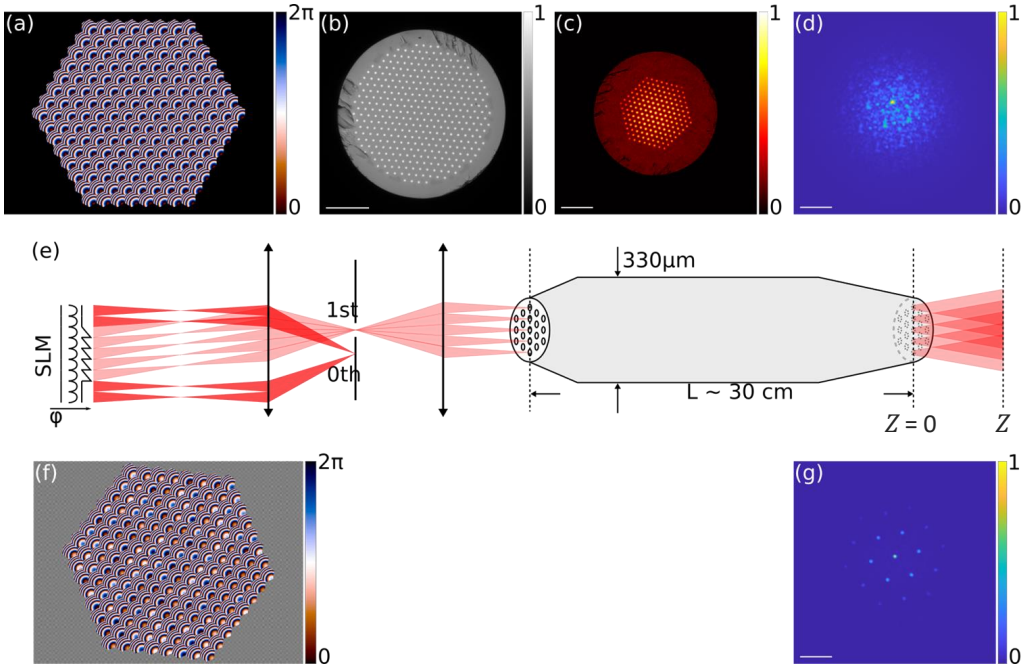

FIGURE 4.18: Schematic of incoupling of light at the proximal end and focusing at the distal end of a tapered multi-core fiber. Exemple for $t^{(\mathrm{im})} = 0.6$. (a) Phase mask on SLM for incoupling into 169 cores. (b) Microscope image of the multi-core fiber end face. (c) Intensity profile in the plane $Z = 0$ (logarithmic color scale). (d) Speckle seen in the plane Z with the phase mask (a) displayed on the SLM. (e) Sketch of light paths from SLM to the distal end of the tapered multi-core fiber. (f) Example of a phase mask which results in a focus at the distal end of the tapered multi-core fiber. (g) Example of intensity distribution in the plane Z with the phase mask (f) displayed on the SLM. SLM, spatial-light modulator. Scale bars, 50 µm.

of the full transmission matrix". In the experiment it is measured as follows. First, a reference field is required since the TM is retrieved by an interferometric measurement. We choose the center core of the hexagonal incoupling pattern [Figure 4.18(a)] as the reference. Using the SLM we inject into the reference core and one other core and the phase of the reference is stepped through 0 to $7\pi/4$ in eight steps. The three resulting interferograms on the CMOS camera, conjugated with the plane Z are recorded. This is repeated for all N cores resulting in an image stack of $3N$ images. From each group of three images the phase difference between the two cores on any of the N_{pix} pixels of the CMOS camera can be found by the methods of phase-stepping interferometry. This gives N_{pix} phase values for each of the N cores. The complex exponential of these phase values are the elements of the sought TM. The resulting TM is then a $N_{\text{pix}} \times N$ matrix in the basis of (input) core modes and (output) camera pixels.

4.7.2 Experimentally measured Imaging properties

Point spread function

Once the transmission matrix is measured it can be used to calculate the required input wavefront to create arbitrary intensity patterns at the output field. Therefore, to establish the distal focus, the appropriate phase mask had to be generated and displayed on the SLM. First, we identify the line of the previously measured TM that corresponds to a central pixel on the CMOS camera. Then, we extracted the phase values and use it to set the phases of the corresponding segments to produce a phase mask typically resembling Figure 4.18(f). Displaying this phase mask on the SLM resulted in a distal central focus, which is an intensity image measured on a CMOS camera conjugated to the plane Z. The measured intensity image stand for the point-spread function and is typically resembling Figure 4.18(g).

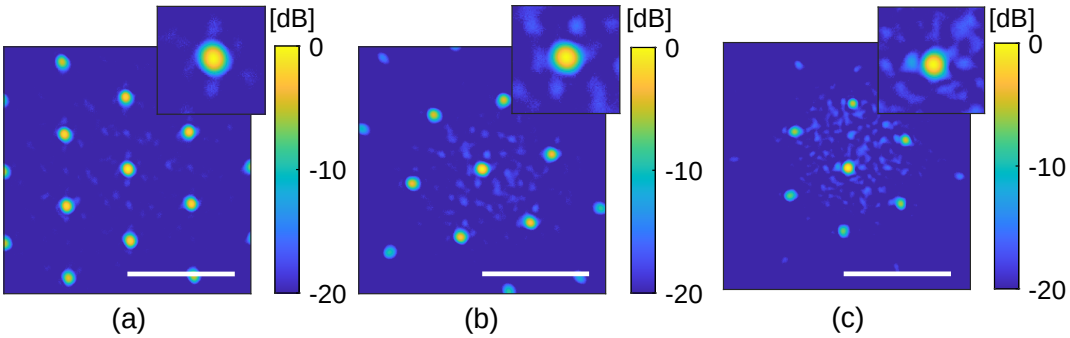

FIGURE 4.19: Point-spread function measured for (a) $t^{(\text{im})} = 1.0$, (b) $t^{(\text{im})} = 0.6$, and (c) $t^{(\text{im})} = 0.4$ in a plane $Z = Z_0 \cdot t^{(\text{im})} = 500$, 300, and 200 µm. Each image is normalized to its maximum intensity. Scale bar in all images is 50 µm. Insets, 7× zoom on the central spot.

Figure 4.19 shows the PSFs of $t^{(\text{im})} = 1$, 0.6, and 0.4, measured at distance $Z = Z_0 \cdot t^{(\text{im})} = 500$ µm, 300 µm, and 200 µm respectively. The reason behind

measuring the PSF at different distances for different taper ratios is that as the taper ratio decreases at the distal end of the multi-core fibers, the distance between cores shrinks and thus, diffracted light interferes closer to the distal end. The measured FWHMs of the PSFs are 4.2, 4.0, and 3.6 μm, slightly larger than predicted.

The experimentally measured PSFs are in line with the predictions, that is, increasing intensity in the central focus and decreasing intensity in the satellite peaks as $t^{(\mathrm{im})}$ is decreased. This trend is quantified in the measured Strehl ratio.

Memory effect

The experimentally measured memory effect curves are presented in Figure 4.20. The data underlying this figure was two image stacks acquired on the CMOS camera. The first stack was acquired by using the TM scan method as follows. The TM scan method was used to generate the phase masks resulting in a number of distal foci on a line along the x-direction. At each position, the image of the optimized focus was acquired by the CMOS camera. The second stack was acquired by using the ME scan method as follows. The first image of the ME scan stack was identical to the first image of the TM scan stack, with the focus on $x = 0$. Subsequently the focus was moved to the same x-positions as for the TM scan stack by using the ME scan method, and for each position an image was acquired by the CMOS camera. The memory effect curve $M(x)$ in Figure 4.20 was extracted from the two image stacks in the following way.

$$M(x) = \frac{\text{intensity of focus on } x \text{ produced by ME scan}}{\text{intensity of focus on } x \text{ produced by TM scan}} \tag{4.10}$$

So, we measure the memory effect in a similar way as in Equation (4.5).

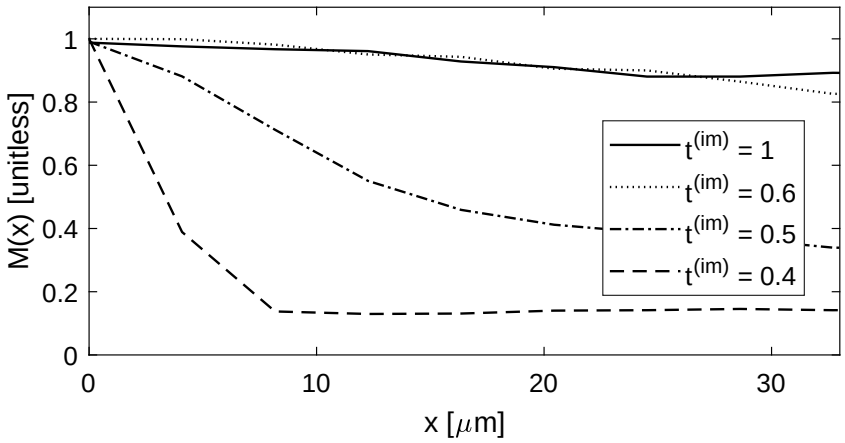

FIGURE 4.20: Memory effect measured experimentally for multi-core fibers with different taper ratios.

As shown in Figure 4.20, the measured memory effect curves are in line with the predicted ones in Figure 4.7. Figure 4.20 shows a conservation of almost full memory effect until the taper ratio $t^{(\mathrm{im})} = 0.6$. However, further decrease

in taper ratio minimize the memory effect, where it shows an almost complete absence at $t^{(\mathrm{im})} = 0.4$.

Strehl ratio

The Strehl ratios of the tapered multi-core fiber with $t^{(\mathrm{im})} = 1,\ 0.6,\ 0.4$ are extracted from the intensity images presented in Figure 4.19(a-c) respectively. It is calculated in similar way as in Equation (4.3), then measured Strehl ratio is

$$S = \frac{\text{sum of the intensities of pixels comprising the central focus}}{\text{sum of the intensities of all pixels}} \tag{4.11}$$

Figure 4.21 presents the Strehl ratio of $t^{(\mathrm{im})} = 1,\ 0.6$, and 0.4, measured at distance $Z = Z_0 \cdot t^{(\mathrm{im})} = 500$ µm, 300 µm, and 200 µm respectively. These measured Strehl ratios confirm the predictions, so the Strehl ratio increases as the taper ratio of the imaging segment $t^{(\mathrm{im})}$ decreases. It starts with a value of 7 % at $t^{(\mathrm{im})} = 1$, then it increases to 15 % at $t^{(\mathrm{im})} = 0.6$ and reaches 19 % at the smallest value of $t^{(\mathrm{im})} = 0.4$. In terms of absolute power in focus these values correspond to 20, 43, and 54 mW respectively.

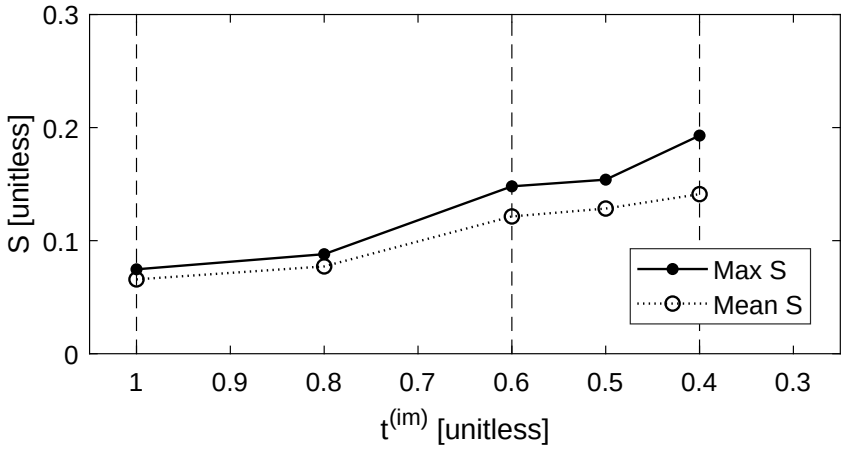

FIGURE 4.21: Strehl ratio measured experimentally for multi-core fibers with several taper ratios. (Max S) refers to maximum Strehl ratio and (Mean S) to the mean of Strehl ratio

4.8 Application

In the following section, we give a demonstration of the application of the fabricated tapered multi-core fibers in a two-photon lens-less endoscope system and quantify the gains in imaging performance.

4.8.1 Two-photon excitation fluorescence imaging

The formation of a two-photon fluorescence image in a lens-less endoscopy system requires a single-point detector to acquire the two-photon fluorescence generated by the sample; and a raster scanning scheme where the focus is scanned across two dimensions. The distal focus can be moved across the (x,y)-plane at the distance Z from the distal end facet of the tapered multi-core fiber in two ways which we refer to as "TM scan" and "ME scan".

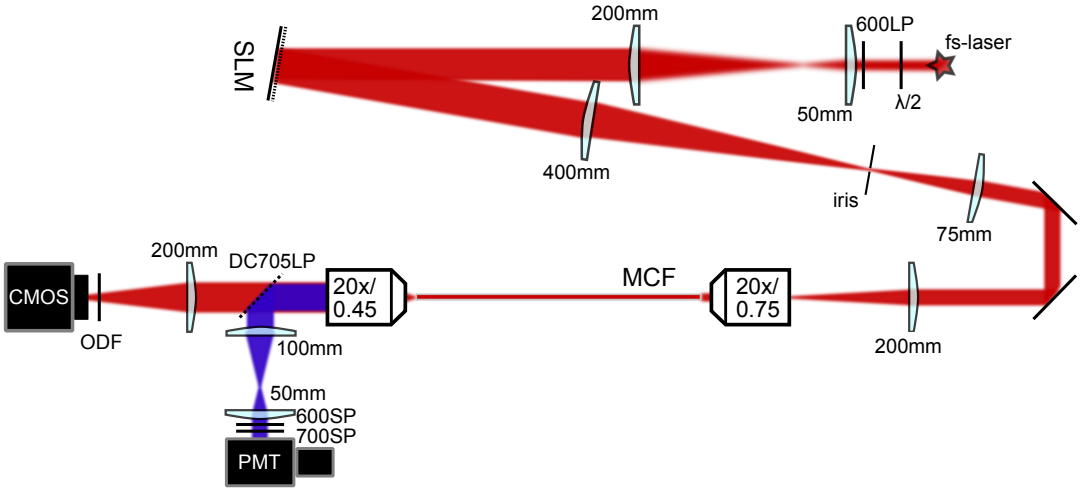

FIGURE 4.22: Lens-less endoscope setup used to perform focus scanning two-photon-imaging in the forward direction.

The "TM scan" method uses the knowledge of the previously measured TM to generate a dedicated phase mask for each (x,y)-position of the distal focus similar to what was done to establish a central focus in the preceding paragraph. When these masks were displayed in succession on the SLM the distal focus was scanned across the (x,y)-plane.

The "ME scan" method takes its starting point in the phase mask that results in a central focus. If the tapered multi-core fiber exhibits some ME then the distal focus can be moved by adding a small phase increment on each segment of the phase mask. This increment should be proportional to the segment's x- and y-coordinate, i.e. a phase ramp. The resulting displacement of the spot is proportional to slope of the phase ramp, the exact dependence can be found from Equation (4.4). When possible, the ME scan method has the dual advantage of not requiring knowledge of a full transmission matrix; and the possibility to use fast galvo mirrors to generate the phase ramps (virtually unbound image acquisition time) [49].

In our lens-less endoscope system, we performed two-photon imaging with both the TM scan method and the ME scan method using multi-core fibers samples with different taper ratios. For simplicity and pragmatism, here, we used the SLM for both TM scan method and the ME scan, and so we are unable to demonstrate the speed advantage. For these proof-of-principle demonstrations, we used yellow-green fluorescent beads as a sample whose emission spectrum is similar to that of yellow fluorescent proteins commonly expressed for example in mice neurons during in-vivo exploration of neuronal activity.

Figure 4.22 is the same experimental setup as the one shown in Figure 4.17 but adapted for the collection of the two-photon fluorescence (TPF) signal in forward direction. For this mission a dichroic 705 long-pass (FF705-Di01-25×36, Semrock) was put after the collection objective. The back-focal plane of the objective is imaged on an analogue photomultiplier tube (R9110, Hamamatsu). A combination of two short-pass filters (600SP and 700SP, Thorlabs) block leakage radiation from the excitation laser. The long-pass filter (600LP, Thorlabs) before the SLM additionally hinders pump diode leakage radiation from the fs-laser to interfere with the TPF signal detection on the PMT.

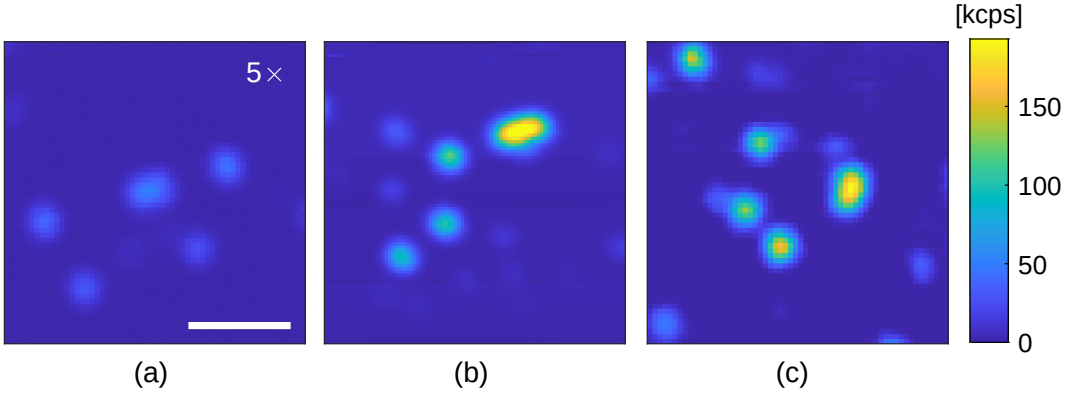

FIGURE 4.23: Two-photon excited fluorescence images of fluorescent beads with the lens-less endoscope. Point-scanning with an optimal focus on each pixel (TM scan) and taper ratios (a) $t^{(\mathrm{im})} = 1$ and $Z = 500$ µm; (b) $t^{(\mathrm{im})} = 0.6$ and $Z = 300$ µm; and (c) $t^{(\mathrm{im})} = 0.4$ and $Z = 200$ µm. Spatial scales are identical for all the images. Intensities in (a) have been multiplied by 5 for visualization. Scale bar, 10 μm.

The acquired two-photon images are presented in Figures 4.23 and 4.24. Figures 4.23(a)-4.23(c) presents the TPEF images acquired using "TM scan" method with $t^{(\mathrm{im})} = 1$, 0.6, and 0.4. These images are acquired as follows. The TM was measured with the CMOS camera conjugated to the plane Z. Then the sample of fluorescent beads was placed in the plane Z, the focus was scanned across 60×60 points in the (x,y)-plane by the TM method, and at each focus position the fluorescence signal was acquired by the PMT.

Figures 4.24(a)-4.24(b) presents TPEF images of fluorescent beads acquired using the "ME scan" method with $t^{(\mathrm{im})} = 1$ and 0.6. These images are acquired as follows. The TM was measured with the CMOS camera conjugated to the plane Z. Then the sample of fluorescent beads was placed in the plane Z, the focus was scanned across 60×60 points in the (x,y)-plane by the ME method, and at each focus position the fluorescence signal was acquired by the PMT.

The comparison of Figures 4.24(a)-4.24(b) to Figures 4.23(a), 4.23(b) provides visual evidence that the memory effect is indeed retained at these values ($t^{(\mathrm{im})} = 1$, 0.6), as predicted. No image with the ME scan is shown for $t^{(\mathrm{im})} = 0.4$ because the ME is absent, thus for this taper ratio we can only acquire TPEF imaging by "TM scan" method.

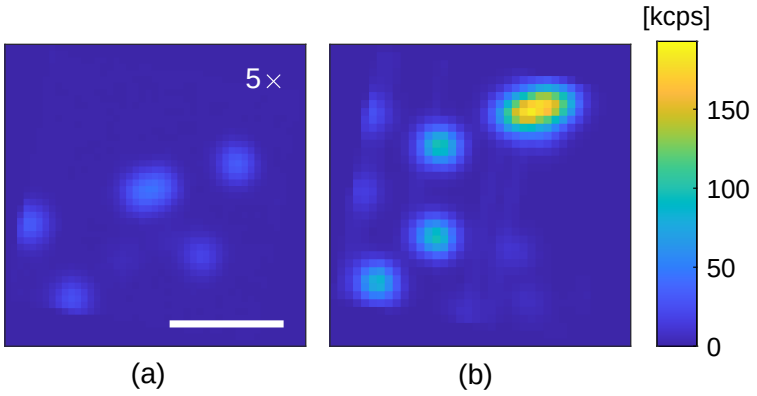

FIGURE 4.24: Two-photon excited fluorescence images of fluorescent beads with the lens-less endoscope. Point-scanning with memory effect starting from an optimal focus on the central pixel (ME scan) and taper ratios (a) $t^{(\mathrm{im})} = 1$; and (b) $t^{(\mathrm{im})} = 0.6$. Spatial scales are identical for all the images. Intensities in (a) have been multiplied by 5 for visualization. Scale bar, 10 μm.

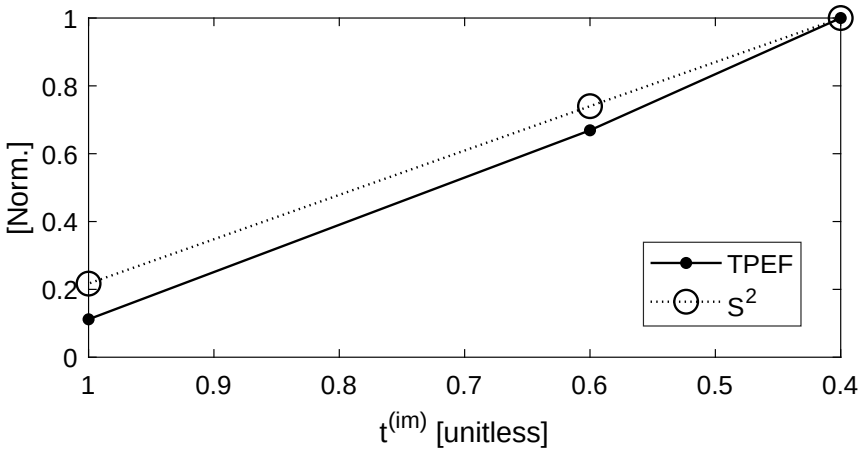

FIGURE 4.25: Evolution of two-photon signal with taper ratio. (dots) Observed two-photon signals; and (circles) the square of the observed Strehl ratios.

All images are on the same intensity scale which allows to appreciate the increase in two-photon signal with decreasing $t^{(\mathrm{im})}$. It can be seen that the signal from single, isolated beads increases appreciably from Figure 4.23(a) over 4.23(b) to 4.23(c). This two-photon signal increase is quantified in Figure 4.25. The points represent a mean over two-photon signal measured on several single, isolated beads. The relative increases are a factor 6.0 for $t^{(\mathrm{im})} = 0.6$ and a factor 8.9 for $t^{(\mathrm{im})} = 0.4$. The two-photon signal increase is expected to be proportional to the square of the Strehl ratio, represented by circles. And indeed the two curves are coincident to a high degree.

4.9 Discussion

Initially, we remark that for the experimental two-photon imaging, only 169 out of the $N = 349$ cores of the tapered MCFs were employed simultaneously. An experimental constraint limiting the number of cores that can be used simultaneously is the number of pixels on the SLM. A 800×600 pixel SLM can be divided into 169 40×40 pixel segments which must control not only the phase but also the focusing of light injected into a core (cf Section 4.8.1), and the latter is compromised as the number of pixels per segment decreases. So, while not a hard limit, 169 cores was the compromise we chose. Workarounds are to use one of the newer SLM generations with higher pixel count; or using the SLM in conjunction with a passive elements like a micro-lens array to take care of the focusing. The modelling was limited to the same number of cores ($N = 169$) in order to have directly comparable results.

Next, we remark that the CMT model has not correctly predicted the experimentally measured Strehl ratios [Figure 4.8 compared to Figure 4.21]. For $t^{(\mathrm{im})} = 0.6$ the prediction is $S = 21$ % versus the observed $S = 15$ %. This discrepancy can be accounted for by two factors not included in the model. (i) Polarization is not accounted for in the CMT model, but the fabricated tapered multi-core fiber has circular ie non-polarization-maintaining cores. In the experiment a polarizer selects one of the polarization components, each core thus contributes a random amplitude to the image on the camera. The effect can be modelled by multiplying each element of $\mathbf{e}^{(\mathrm{prox,mode},j_0)}$ by a random number between zero and one before applying Equation (1.107), and the consequence is a drop of S down to 18 %. (ii) The model calculates the Strehl ratio in the far-field whereas the experiments were done in intermediate planes $Z = 500$, 300, and 200 µm. The predicted Strehl ratio should therefore be taken as upper bounds. If we numerically propagate the predicted far-field to the intermediate plane, this effect alone leads to a drop of S down to 16.5 %. Both effects together result in a drop of S to 12 %. These effects thus seem to fully explain the discrepancy. For $t^{(\mathrm{im})} = 0.4$ the discrepancy is more flagrant, the prediction is $S = 59$ % versus the observed $S = 19$ %. Here; effects (i) and (ii) combined would only result in a drop of S down to 42 %. It is possible that at this small value of $t^{(\mathrm{im})}$ the effect of leakage from the cores into the cladding becomes important. This would signify that the CMT model is at the limit of or even beyond its regime of validity for $t^{(\mathrm{im})} = 0.4$. Beyond this point one would have to resort to FE-BPM modelling to assure accurate results.

Inter-core group delay dispersion [94] is also not accounted for in the CMT model. Non-zero inter-core group delay dispersion has the consequence of reducing the coherence between the fields emerging from different cores (since we are using ultra-short pulses) and hence the Strehl ratio. We have sampled inter-core group delay dispersion in some pairs of cores which indicate that the distribution of inter-core group delay dispersion is narrower than the duration (150 fs) of the ultra-short laser pulse. This is not expected to be a main source of the discrepancy in Strehl ratios and the above discussion corroborates this.

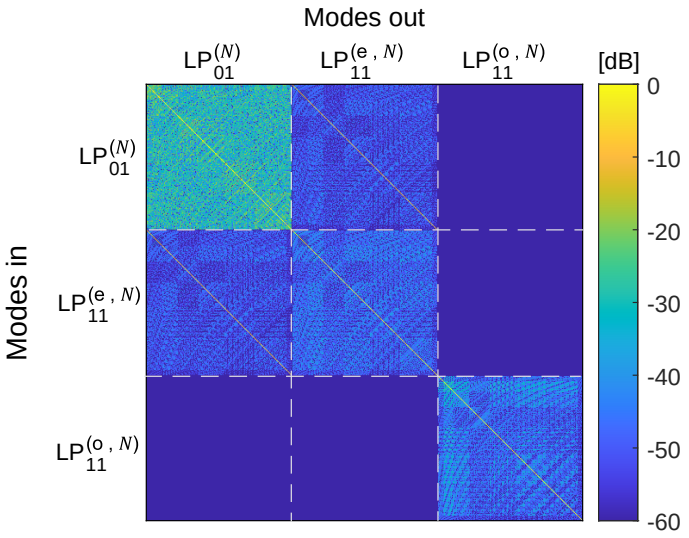

FIGURE 4.26: $3N \times 3N$ Cross-talk matrix between N LP_{01} modes, N $\mathrm{LP}_{11}^{(e)}$ modes and N $\mathrm{LP}_{11}^{(o)}$.

We studied the coupling between the the LP_{01} modes of different cores in the multi-core fiber, as we taper the injection segment to allow only fundamental mode to be launched into each core. However, as we are tapering the distal end of the fiber which we call the imaging segment, we are perturbing the fiber and so cores start to experience coupling. In principle coupling between LP_{01} mode in one core and LP_{11} mode in another core can occur, and if it does, it leads to leakage of LP_{11} mode to the cladding, and this could be potential loss mechanism in these tapers which lead to loss in absolute power. For this reason, we studied the coupling between different modes of a multi-core fiber with taper ratio $t^{(\mathrm{im})} = 0.77$ which leads to V-parameter value just before the cutoff of the LP_{11} mode. Using the CMT model we computed the coupling matrix, transmission matrix and the cross-talk matrix, the same way presesnted in Section 4.3.1. However, here we have $3N \times 3N$ matrices, refer to the coupling between three modes LP_{01}, $\mathrm{LP}_{11}^{(e)}$ and $\mathrm{LP}_{11}^{(o)}$ existing in the multi-core fiber N cores. Figure 4.26 represent the cross-talk matrix computed by the CMT model. This cross-talk matrix show very low cross-talk between LP_{01} and $\mathrm{LP}_{11}^{(e)}$ modes of different N cores (XT $\approx$ -50 dB) and extremely low cross talk between LP_{01} and $\mathrm{LP}_{11}^{(o)}$ modes (XT $\approx$ -250 dB). These low cross-talk are a consequence of large $\Delta n_{\mathrm{eff}} = 8.2 \cdot 10^{-3}$ between LP_{01} and LP_{11} modes. Moreover, the cross-talk between the even and odd modes, $\mathrm{LP}_{11}^{(e)}$ and $\mathrm{LP}_{11}^{(o)}$ respectively, is negligible

and this is because of they have different symmetries. Therefore, we can state that we have almost negligible coupling between the LP_{01} and LP_{11} modes.

In this chapter, we have presented a novel tapered multi-core fiber for optimal two-photon lens-less endoscopy by point-scanning imaging. And we have shown that tapering can ameliorate multi-core fiber for imaging. However, the gain that we achieve depends so much on the main fiber which is used as a starting point. To clarify, we will use the CMT model to predict the imaging properties in an older generation of multi-core fibers which have been optimized for lens-less endoscope imaging in several papers [49, 67, 50, 94], and study the gain that can be achieved by tapering these old generation of multi-core fibers in comparison with the new generation fiber that we present in the above chapter.

The first example is the multi-core fiber that is used in Ref. [67] as a two-photon lens-less endoscope probe. This multi-core fiber contains $N = 169$ cores within an outer diameter $D^{(\text{transport})} = 250$ µm and have the following parameters: $a = 1.5$ µm, $\Delta n = 31{\cdot}10^{-3}$, $\Lambda = 11.8$ µm. Figure 4.27 presents the predicted properties of this multi-core fiber using the CMT model. As shown by Figure 4.27, for these fiber parameters, the taper ratio which maximizes the Strehl ratio under the condition that the "full" memory effect is conserved is $t^{(\text{im})} = 0.8$, and the minimum taper ratio that maximizes the Strehl ratio without any conditions on the memory effect but retaining core guidance (Figure 4.27(f)) is $t^{(\text{im})} = 0.6$. Which are two times smaller than the values identified using the multi-core fiber that we optimize and present in the above chapter [Figure 4.7]. And more importantly, the maximum gain in Strehl ratio achieved by smallest possible $t^{(\text{im})}$ in this fiber is $S \approx 0.5$ [Figure 4.27(e)] which is smaller than the optimized one [Figure 4.8] by a factor of 1.2.

Another example is a multi-core fiber with extremely low cross-talk between cores, is used in Ref. [49] as a lens-less endoscope probe. This multi-core fiber has $N = 475$ cores within an outer diameter $D^{(\text{transport})} = 395$ µm, and has the following parameters: $a = 1.5$ µm, $\Delta n = 30{\cdot}10^{-3}$, $\Lambda = 15.4$ µm. Figure 4.28 presents the predicted properties of this multi-core fiber. As shown by the figure, the smallest taper ratio before cores start to leak to the cladding is $t^{(\text{im})} = 0.6$ (2 times larger than what we got with our multi-core fiber [Figure 4.9]). The distinctive feature in this fiber is the large memory effect which is remaining full until $t^{(\text{im})} = 0.7$. Thus we can define $t^{(\text{im})} = 0.7$ as the value which maximize Strehl ratio while retaining full memory effect. However, the maximum Strehl ratio that can be achieved by this fiber is 0.37 which is the belonging to $t^{(\text{im})} = 0.6$ as being the smallest taper ratio before cores start to loose their guidance. This Strehl ratio is 3 times smaller than the maximum Strehl ratio achieved by the multi-core fiber that we optimize in this thesis [Figure 4.8].

From these two examples, where we apply tapering to a multi-core fibers that were already optimized at some point the same way as we did for our optimized multi-core fiber. We have seen that the old generation of multi-core fiber is not able to achieve the same performance and gain in imaging properties as the ones achieved by tapering the "new generation" multi-core fiber that we optimize in this thesis work. Therefore, we can emphasize that the gain that we can achieve by tapering a multi-core fibers depends mainly on the fiber parameters that is used as a starting point.

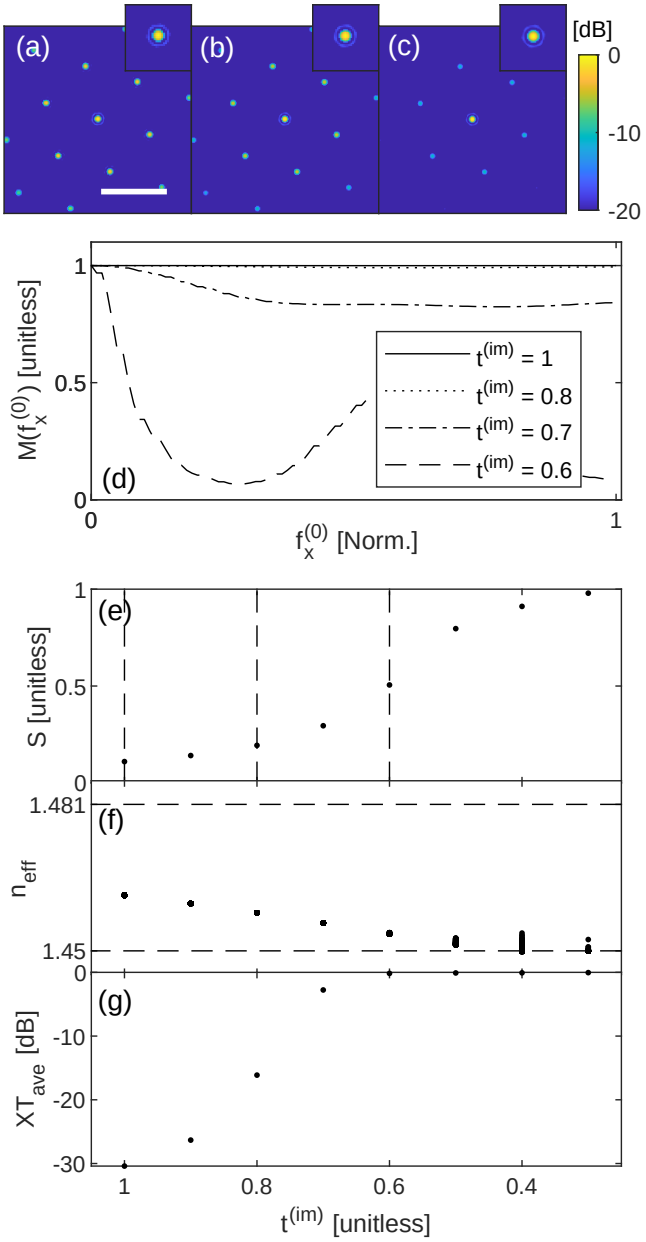

FIGURE 4.27: Properties of multi-core fiber, from Ref. [67], predicted by CMT model. (a)-(c) PSF for $t^{(\mathrm{im})} = 1.0$, 0.8, and 0.7 in a plane $Z = Z_0 \cdot t^{(\mathrm{im})}$. Each image is normalized to its maximum intensity. Scale bar, 50 μm. Insets, 5× zoom on the central spot. (d) Memory effect curves. Horizontal axis normalized to half the distance between replica spots. (e) Strehl ratio. (f) Effective indices of supermodes. (g) Average XT.

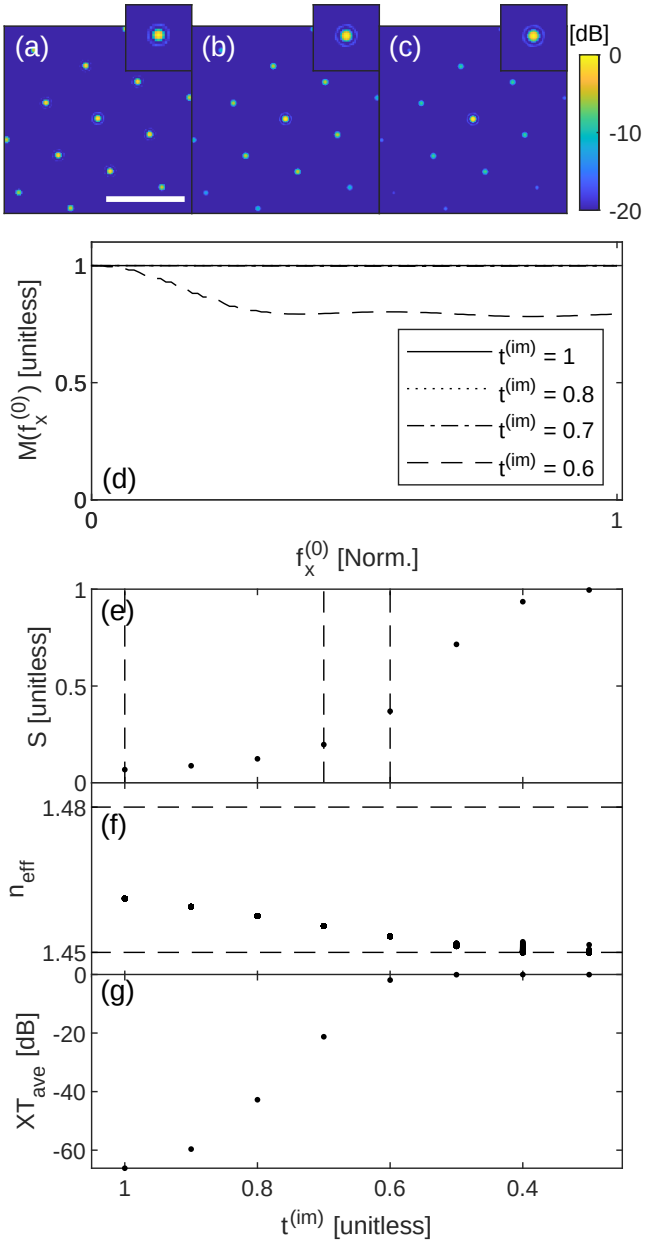

FIGURE 4.28: Properties of multi-core fiber, from Ref. [49], predicted by CMT model. (a)-(c) PSF for $t^{(\mathrm{im})} = 1.0$, 0.7, and 0.6 in a plane $Z = Z_0 \cdot t^{(\mathrm{im})}$. Each image is normalized to its maximum intensity. Scale bar, 50 μm. Insets, 5× zoom on the central spot. (d) Memory effect curves. Horizontal axis normalized to half the distance between replica spots. (e) Strehl ratio. (f) Effective indices of supermodes. (g) Average XT.

4.10 Conclusion

In this chapter, we have presented a novel tapered multi-core fiber for optimal two-photon lens-less endoscopy by point-scanning imaging. Our key result is that optimized tapered multi-core fiber can increase two-photon yield by a factor 6.0 while still keeping the ability to point-scan by the memory effect, and up to a factor 8.9 while sacrificing the memory effect. These results are decoupled from the transport segment of the tapered multi-core fiber with low cross-talk which can be meters in length without altering the results.

The lens-less endoscope system used to generate the two-photon excited fluorescence images presented in Figures 4.23 and 4.24 employed a detector located at the distal end, after both multi-core fiber and sample. Thus it is collection the fluorescence signal generated from the fluorescent beads in transmission configuration. In the coming Chapter 5, we demonstrate the use of the optimized tapered multi-core fiber that we present in this chapter to generate two-photon excited fluorescence images in a "true" endoscopic configuration, and thus detecting fluorescence collected in the backward direction through the multi-core fiber.

Chapter 5

Polymer-coated tapered fiber

5.1 Genuine lens-less endoscope

The lens-less endoscope system used to generate two-photon images presented in chapter 4 are acquired in transmission or forward direction, which means that the detector is located at the distal end, after both multi-core fiber and sample, and so it detects the fluorescence signal transmitted through the sample. However, in a "true" endoscopic configuration, the detector is located at the proximal end, detecting fluorescence collected in the backward direction through the multi-core fiber. Therefore, we aim to realize versions of the optimized tapered multi-core fiber presented in chapter 4 with double cladding to collect fluorescence in the backward direction, and thus demonstrating a "genuine" lens-less endoscope. Accordingly, we think of coating the tapered multi-core fibers with a low-index polymer as a final step to realize a tapered multi-core fibers with double cladding, and thus called double-clad (also called dual-clad) fiber.

5.2 Double-coated tapered multi-core fiber

In 2013, Andresen et al. demonstrate how a double-clad multi-core fiber allows for efficient fluorescence collection and thus to work with a proximal detector [67]. In this paper, the double-cladding was a ring of air holes around the N cores. However, in the present work we were unable to use the same kind of double cladding because the post-processing on the glass processing and splicing system would have collapsed the air holes.

Therefore, we think of coating the tapered multi-core fibers with a low-index polymer to serve as a second cladding. The schematic presentation of polymer-coated tapered multi-core fiber is shown by Figure 5.1. In this design, the cores of the multi-core fiber are contained in an “inner cladding” of silica, which is surrounded by a low index polymer, as an “outer cladding”. Due to the big refractive index difference between silica ($n_{silica} = 1.45$) in the inner cladding and the low index polymer ($n_{polymer} = 1.37$) in the outer cladding, the whole inner cladding will function as a multi-mode waveguide with high numerical aperture and therefore very efficient in collecting backscattered fluorescence.

The polymer-coated tapered multi-core fibers will then compromise two distinct guiding regions, the first one is the cores of the multi-core fiber and the second one is the inner cladding which is the cladding of the multi-core fiber.

Therefore, the polymer-coated tapered multi-core fiber will has the ability to support single-mode propagation through the cores for illumination and multi-mode propagation through the inner cladding for epi-detection.

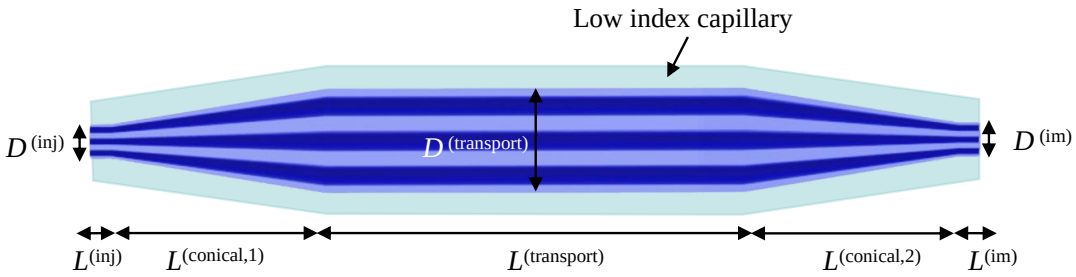

FIGURE 5.1: Scheme of polymer-coated tapered multi-core fiber.

5.2.1 Fabrication

The fabrication of the uniform multi-core fiber to the specification requirement of the transport segment ($\Delta n = 30{\cdot}10^{-3}$; $\Lambda = 14$ µm; $a = 2.5$ µm; $N = 349$) is described in details in Section 4.5.1.

Then we post-processed the uniform multi-core fiber to obtain the tapered multi-core fiber represented by Figure 5.2(a) by tapering a short length at two distinct positions of the uniform multi-core fiber using a CO_2 laser-based glass processing and splicing system (Detailed in Section 4.5.2). After tapering process, we are not going to cleave in the middle of the waists of the two tapers as mentioned in Section 4.5.2. However, we keep the two terminals of the tapered fiber for coating process.

Coating the tapered multi-core fibers is implemented using a system developed within our laboratory. Coating process is done by two consecutive steps, in the first step the whole tapered multi-core fiber is coated with a low-index polymer (refractive index n= 1.37) which will function as a second cladding. And in the second step, the whole tapered multi-core fiber is re-coated with high index polymer (n=1.514) for mechanical protection. Figure 5.2(b) presents a sketch of the tapered multi-core fiber after the re-coating process.

As a final step we cut in the waist and polish the terminal ends of the fiber (Figure 5.2(b)) to obtain a polymer-coated tapered multi-core fiber represented by Figure 5.2(c). The polishing process will be described in details in the coming section which is used as final touch to prepare the polymer-coated tapered multi-core fibers for imaging application.

5.2.2 Polish terminal ends

The first and crucial step for using fiber optic probes in imaging applications is preparing the end-face of fiber optic precisely. The end-face of the optical fiber should be uniform and smooth in order to reduce the optical loss due to light scattering [97]. In Chapter 4 we used to cleave the terminals of the tapered

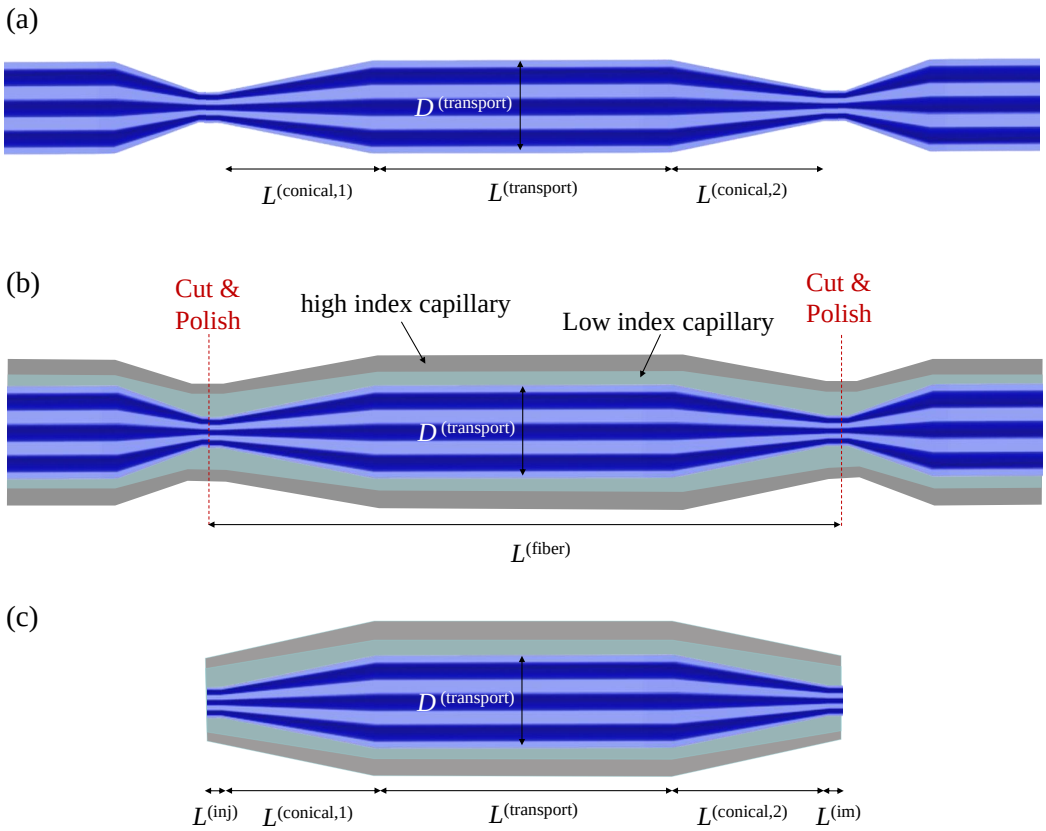

FIGURE 5.2: Scheme of the polymer-coated tapered multi-core fiber in different steps of fabrication. (a) Fiber tapered at two distinct positions by CO_2 laser-based glass processing and splicing system. (b) Fiber coated with low index polymer (green) and high index polymer (grey). (c) Scheme of the final fiber sample.

multi-core fibers and create a perfectly flat end-faces. However, for polymer-coated multi-core fibers it is not practical to cleave the fibers while they are coated with the polymer especially that we need the polymer to reach the extreme end of the tapered multi-core fiber. Therefore, we resort to polishing the end-faces of the coated multi-core fibers instead of cleaving them.

For this aim we used mechanical polisher (KrellTech-Trig Lite Fiber Polisher). This process is basically based on rubbing the fiber end-face on a polishing films and thus forming a smooth end-face with the desired geometry (flat, side-firing or conical). This polisher machine comprises of polishing film attached to a rotary disk. A fiber adapter for mounting the ferrule to which optical fiber is fixed, the ferrule is interchangeable to match fiber diameter. A real-time video system which actively monitors the polishing process. An inspection module which permits the in-line viewing of the polished fiber to insure surface quality.

Specific details of the process are given in the following. The polymer-coated tapered multi-core fiber is cut 2 mm before the middle of its waist, so that we have to polish 2 mm to get the fiber polished to its middle of the waist. Then, the fiber is inserted inside the fiber adapter with the supported ferrule tip. The end-face of the fiber is set smoothly in contact with the polishing films that are stucked to the spinning disk by means of a high precision translation stage (micron-level positioning). The films are changed according to their roughness, starting from rough to finer ones. Thus, the roughness of fiber end-face is also changed implicitly. In our work, we used the commercially available KrellTech polishing films and their roughness follows the following order 30 μm, 9 μm, 3 μm, 0.3 μm. Where we spent from 30 s to 60 s of polishing on each film. In order to obtain flat-ended fiber tip, we positioned the fiber vertically (90°) to the polishing film. Then we check on the side camera that is accompanied with the polisher, the fiber polished end-face, and if its still looks not smooth we re-polish it again with the finest polish paper (0.3 μm). Finally, we remove the fiber and re-check its polished end on an optical microscope.

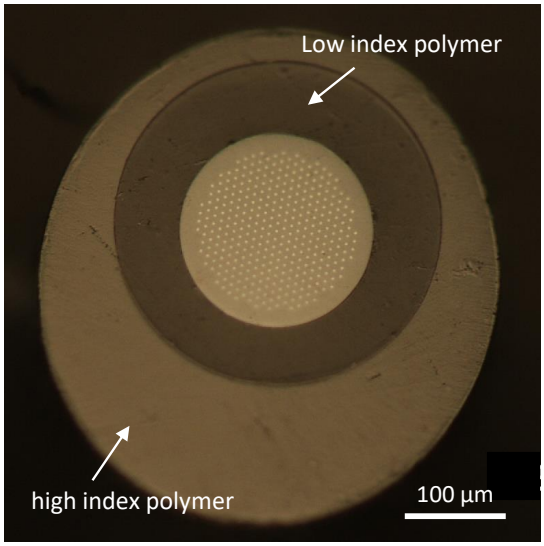

FIGURE 5.3: Microscopic image of the end face of polymer-coated tapered multi-core fiber after polishing.

For future in-vivo biomedical imaging, we polished the terminals of some of the samples of the polymer-coated tapered multi-core fibers in a conical shape, to facilitate piercing them in soft tissues, where conical shape tip has the advantage to penetrate to the tissue more easily than a flat tip. Note that we are polishing only the polymer in a conical shape in the aim of reducing the total diameter of the distal tip of the fiber by reducing the thickness of the polymer.

Figure 5.4 shows the polisher adapted for polishing with an angle to form the conical shape in the distal end of the fiber. We positioned the fiber in 60° (the highest reached angle with our polisher system) with the polishing film. Then, the fiber is rotated around its axis by means of a chuck connected to an electric motor with a belt. The end-face of the tilted fiber is set smoothly in contact with the polishing film attached to the spinning disk in order to polish the polymer in conical shape without damaging the fiber.

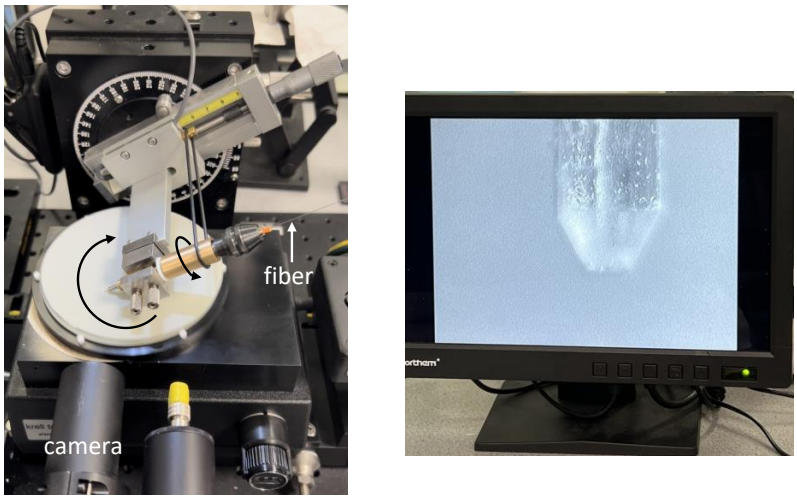

FIGURE 5.4: (a) Polisher system while polishing the polymer in the end of the fiber in cone shape as shown by the screen of the system (b) which is visualized by the camera of the polisher.

5.3 2PEF imaging in true endoscope system

The experimental setup of two-photon excitation fluorescence imaging in true endoscopic configuration is sketched in Figure 5.5. This setup is similar to the one shown in Figure 4.22 but adapted for the collection of the two-photon fluorescence (TPF) signal in backward direction. Thus, the detector and camera are placed in the proximal end of the multi-core fiber, which is opposite to the sample side. The imaging process occurs as follows. First, we measured the transmission matrix of the polymer-coated tapered multi-core fiber in the same way as presented in Section 4.7.1. Then we incident pulsed fs-laser (Chameleon Ultra II, Coherent) tuned to 920 nm wavelength into the spatial-light modulator. Using the spatial light modulator, we inject the majority of the excitation light from the pulsed laser source into the individual fiber cores of the multi-core

fiber at the proximal end, without significantly injecting into the inner cladding modes. So excitation light can be relayed to the sample at the distal end through the cores of the multi-core fiber. At the distal end, the fluorescence signal emitted from the sample overlaps strongly with the inner cladding modes and much less with the cores modes. So it mainly gets injected into the inner cladding (the cladding of multi-core fiber) in which it is relayed back from the distal end to the proximal end where it can be filtered and detected on the photomultiplier tube (PMT). Note that, a CMOS camera is placed at the distal end of the fiber just for inspection and positioning of the sample.

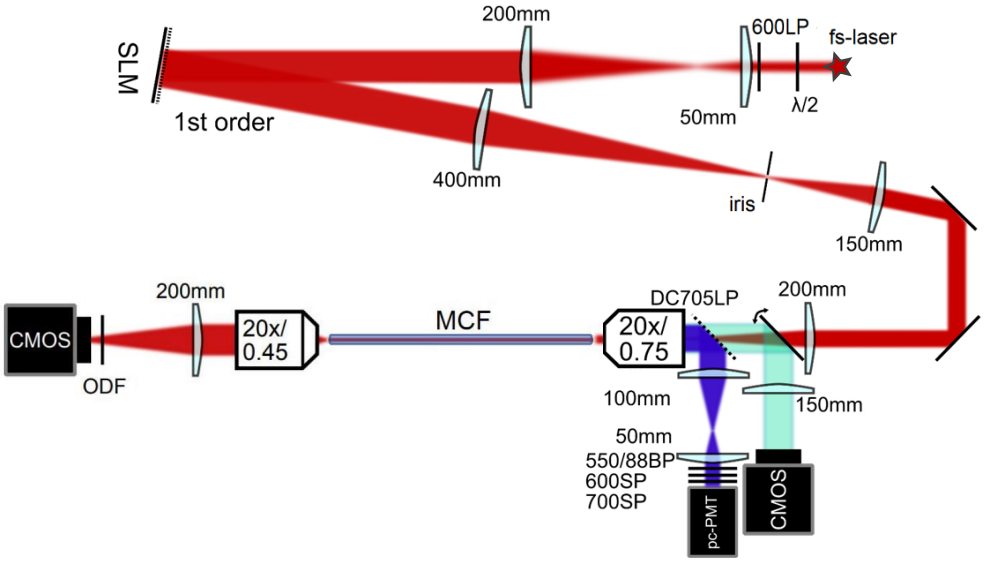

FIGURE 5.5: Lens-less endoscope setup used to perform focus scanning two-photon-imaging in the backward direction. CMOS, CMOS camera (FLIR, BFLY-U3-23S6M-C). ODF, neutral density filter. PMT, photo-multiplier tube (Hamamatsu, R9110). 20×/0.45, microscope objective (Olympus, LUCPlanFLN, 20× / 0.45 NA). Polymer-coated tapered multi-core fiber. 20×/0.75, microscope objective (Nikon, CFI Plan Apo, 20× / NA 0.75). SLM, spatial-light modulator (Hamamatsu, X10468-07.

To demonstrate two-photon endoscopic imaging, we placed a sample of fluorescent beads at the distal end of the fiber. We recorded the two-photon signal from the fluorescent beads on a detector located at the proximal end to construct the point-scanning image, using the spatial-light modulator as the scanning element. The sample of fluorescent beads is placed in a plane at distance $Z = Z_0 \cdot t^{(\mathrm{im})}$ ($Z_0 = 500$ µm) from the distal end face.

For the purpose of checking the efficiency of the polymer-coated multi-core fiber, we acquired two-photon images of the fluorescent beads under the same circumstances, though not simultaneously, in both forward-direction and epi-direction. For detection in forward-direction, the detector placed at the distal end of the fiber and the two-photon signal from the sample was collected directly on the distal detector. However, For detection in epi-direction, the detector is placed at the proximal end of the fiber, and the two-photon signal from the

sample was collected in the backward direction through the polymer-coated multi-core fiber.

Figure 5.6 present two-photon images of fluorescent beads, collected in forward and epi-direction with a polymer-coated periodic multi-core fiber of taper ratio $t^{(\mathrm{im})} = 0.6$. These images are acquired by point-scanning with an optimal focus on each pixel (TM scan). We can see that the signal levels are roughly the same in both forward-detection (Figure 5.6(a)) and epi-detection (Figure 5.6(b)), and this basically means that the polymer-coated fiber is very efficient in collecting the back-scattered two-photon signal.

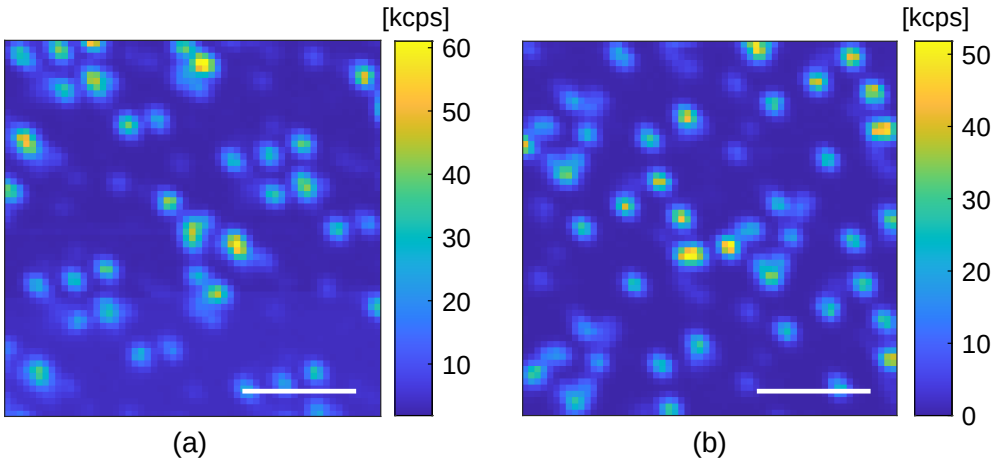

FIGURE 5.6: Two-photon excited fluorescence images of fluorescent beads with polymer-coated periodic MCF of taper ratio $t^{(\mathrm{im})} = 0.6$ detected at $Z = 300$ µm in (a) forward-direction and in (b) epi-direction. Scale bar, 20 µm.

Furthermore, we also acquired two-photon excited fluorescence images of mammalian osteosarcoma cells, labelled with Alexa Fluor 488 dye, with epi-detection. The cellular resolution and sensitivity is clearly demonstrated in the two-photon excited fluorescence image presented in Figure 5.7(b), compared to the transmission image (one-photon image using LED source detected by the camera on the distal end) of the same cell presented in Figure 5.7(a).

5.4 Aperiodic multi-core fiber

In Chapter 4 we established that the point-spread function is inherently determined by the characteristics of the fiber used. In this Chapter we have considered multi-core fiber with a periodic core layout, cores arranged in a multi-ring hexagonal lattice. Periodicity in the core layout of a multi-core fiber has the consequence of additional peaks in the point-spread function, as shown in Sections 4.4.3 and 4.7.2. These multi-peaked point-spread functions lead to overlapping replica images in lens-less endoscopes. Accordingly, the performance of the lens-less endoscope is highly dependent on the layout of the fiber cores.

In this Section we will explore multi-core fiber with aperiodic core layout to make amelioration to the point-spread function.

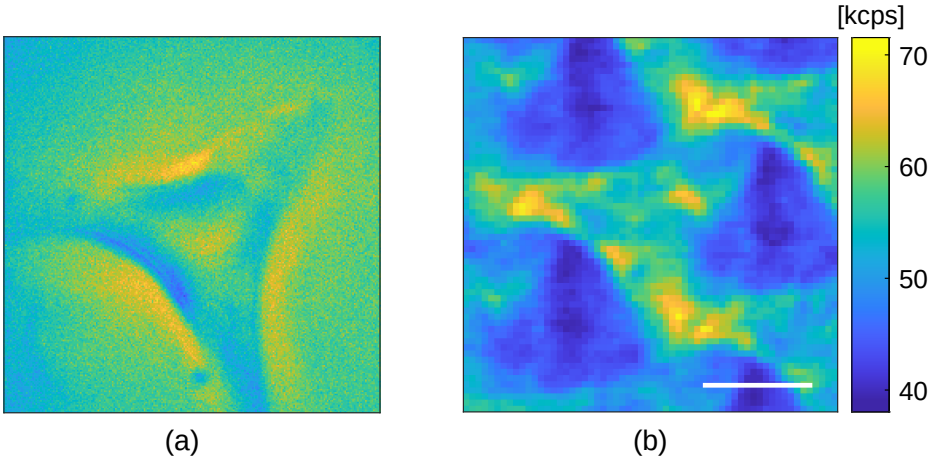

FIGURE 5.7: (a) One-photon transmission image of mammalian osteosarcoma cell. (b) Two-photon excited fluorescence images of mammalian osteosarcoma cell detected in epi-direction with a polymer-coated periodic MCF with taper ratio $t^{(\mathrm{im})} = 0.6$ at $Z = 300$ µm. Scale bar, 10 µm.

5.4.1 Aperiodic layout properties

The design of the aperiodic multi-core fiber was born out of the necessity to get rid of a persistent imaging artifact that is always present when using the periodic multi-core fibers. This artifact, and its solution, can be understood by calculating the relation between core positions and excitation intensity distribution on the sample. Even though lens-less endoscopes based on multi-core fiber typically operate in the Fresnel regime, a good approximation can be obtained by assuming that the sample is located in the far-field. In this case, the field on the sample (far-field) can be found by Fourier transform of the field in the multi-core fiber distal end-face (near-field).

Let us consider a multi-core fiber consists of N identical cores. The cores are located at (x_i, y_i) and the core positions can be defined in an array factor (AF)

$$AF(x,y) \;=\; \sum_{i=1}^{N} \delta(x - x_i)\; \delta(y - y_i) \tag{5.1}$$

All the cores in the multi-core fiber emit with the same intensity distribution. Additionally, we suppose that all the emissions are in-phase, then the fields of all the cores are also identical and denoted by $E_{1\mathrm{core}}$. The general expression for the near-field at the multi-core fiber distal end-face is then

$$E^{\mathrm{NF}}(x,y) = E_{1\mathrm{core}} \otimes AF(x,y) \tag{5.2}$$

Thus the general expression for the far-field (field on the sample) can be found as

$$\begin{aligned} E^{\mathrm{FF}}(x,y) &= \mathcal{F}[E^{\mathrm{NF}}(x,y)] \\ &= \mathcal{F}[E_{1\mathrm{core}} \otimes AF(x,y)] \\ &= \mathcal{F}[E_{1\mathrm{core}}] \cdot \mathcal{F}[AF(x,y)] \\ &= \tilde{E}_{1\mathrm{core}}(f_x, f_y) \cdot \tilde{AF}(f_x, f_y) \\ &= \tilde{E}_{1\mathrm{core}}(\frac{x}{\lambda Z}, \frac{y}{\lambda Z}) \cdot \tilde{AF}(\frac{x}{\lambda Z}, \frac{y}{\lambda Z}) \end{aligned} \tag{5.3}$$

where the tilde denotes Fourier transformation.

The right hand side of Equation (5.3) contains two factors. The first one ($\tilde{E}_{1\mathrm{core}}$) is the far-field distribution of the emission of a single core, which is in general a broad, smooth function which defines the attainable field-of-view. The second one ($\tilde{AF}$) basically determines the point-spread function of the lens-less endoscope. Therefore, from this expression, we can evaluate the impact of core positions in a multi-core fiber with periodically arranged cores.

In general, the hexagonal periodic structure is naturally adapted by the cores during fabrication of the multi-core fibers by the "stack-and-draw" method [98]. Considering the one-dimension case with a pitch Λ, the AF can be described as a comb function

$$AF_{\mathrm{periodic}}(x) = \mathrm{comb}(\frac{x}{\lambda}) \tag{5.4}$$

which leads to an $\tilde{AF}_{\mathrm{periodic}}$ of

$$\tilde{AF}_{\mathrm{periodic}}(x) = \frac{1}{\Lambda}\mathrm{comb}(\Lambda\frac{x}{\lambda Z}) \tag{5.5}$$

The imaging artifact in periodic multi-core fiber becomes immediately apparent by Equation (5.5). The point-spread function is approximately equal to $|\tilde{AF}|^2$. Thus the point-spread function is not single-peaked, but consists of an entire array of peaks with a period of recurrence equals to $\lambda Z/\Lambda$. Thus, period of recurrence is inversely proportional to pitch size and could in principle be increased by decreasing Λ. In endoscopic imaging, $\tilde{AF}_{\mathrm{periodic}}$ thus gives rise to superposed replica images which must be considered as, a very detrimental imaging artifact. An example is shown by Figure 5.10(a), it should present the image of number 7 from a resolution test chart, but what we see is a periodic replicas of the imaged number 7.

However, if we consider an "aperiodic multi-core fiber", which has its cores arranged on an aperiodic grid, the situation changes and AF becomes

$$\tilde{AF}_{\mathrm{aperiodic}}(x) = \mathcal{F}[AF_{\mathrm{aperiodic}}(x)] \approx \delta(x) \tag{5.6}$$

It is clear from Equation (5.6) that aperiodic multi-core fiber results in a singly-peaked point-spread function, eliminating the duplicate peaks of the

periodic layout. Then singly-peaked point-spread function should permit to acquire an artifact-free image over the entire attainable field-of-view given by the width of $\tilde{E}_{1\text{core}}$.

One way to obtain an aperiodic multi-core fiber is to map each core of a multi-core fiber onto a copy of itself shifted to a random position. However the random core layout is obviously impractical for two reasons. First reason is because there is no scalable method to fabricate a multi-core fiber with the random layout, thus it would not be realistically susceptible to fabrication. Second reason is because, in a completely random layout, the inter-core distances vary wildly, which means that some cores are extremely far and some other cores are extremely close. And extremely close cores would compromise the diagonal nature of the transmission matrix of the multi-core fiber because cross-talk between very close cores would be inevitable.

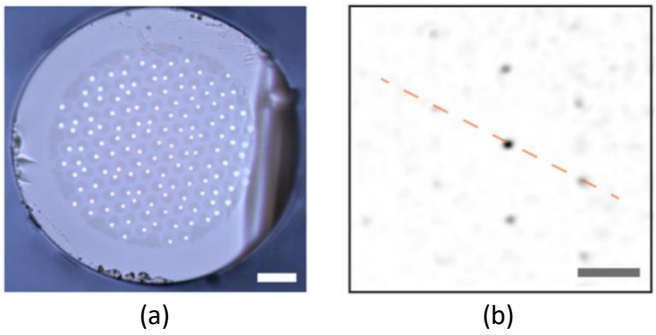

FIGURE 5.8: (a) Microscope image of the fabricated multi-core fiber with pseudo-random core layout. (b) Measured resulting point-spread function from Ref. [99].

Another way of introducing randomness in a multi-core fiber, that is still practical to fabricate, is the pseudo-random layout approach, which is proposed by Sivankutty et al. [99]. The authors in this paper chose the hexagonal lattice as a starting point of their design. Then each core is offset radially from the master lattice by a fixed distance, and then rotated by a random angle about the original center. Hence generating a multi-core fiber with cores laid out as shown by Figure 5.8(a). By this approach, authors were able to fabricate an aperiodic multi-core fiber with the conventional fiber drawing technique. Additionally, in this approach, the magnitude of the transverse core shift is constant, and only the direction of the shift is random. Therefore, a degree of control can still be exerted on the inter-core coupling. The point-spread function resulting from this core layout is shown in Figure 5.8(b). As clearly shown, the point-spread function is much closer to be singly-peaked than in the case of the hexagonal-periodic core layout (Figure 4.6), but a significant secondary peaks still be observable. This is due to the fact that the master lattice of the pseudo-random layout is still hexagonal. The authors then integrated the fabricated aperiodic multi-core fiber in a lens-less endoscope to confirm the added imaging capabilities brought about by this aperiodic multi-core fiber. A resulting image of a USAF test chart is shown in Figure 5.10(b). This image approve the absence of duplicate images that present in the case of periodic multi-core fiber.

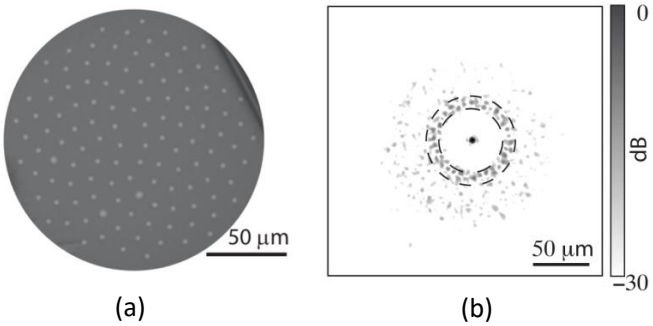

FIGURE 5.9: (a) Electron micrograph of the Fermat's spiral multi-core fiber. (b) Measured resulting point-spread function from Ref. [81].

Later on, Sivankutty et al. reports a novel aperiodic multi-core fiber with a core layout based on Fermat's golden spiral, in order to reach a more random layout than the pseudo-random one detailed above. The authors here show that Fermat's spiral multi-core fiber exhibits a point-spread function that is centrally peaked with the absence of multiple satellite peaks associated with the hexagonal array [81]. Figure 5.9(b) presents the point-spread function resulting from the Fermat's golden spiral multi-core fiber shown by Figure 5.9(a). It is immediately apparent that this point-spread function is much more singly-peaked than the ones presented in Figure 5.8(b) which is associated with the pseudo-random layout. An image obtained with the Fermat's spiral multi-core fiber is presented in Figure 5.10(c) showing the absence of replica images.

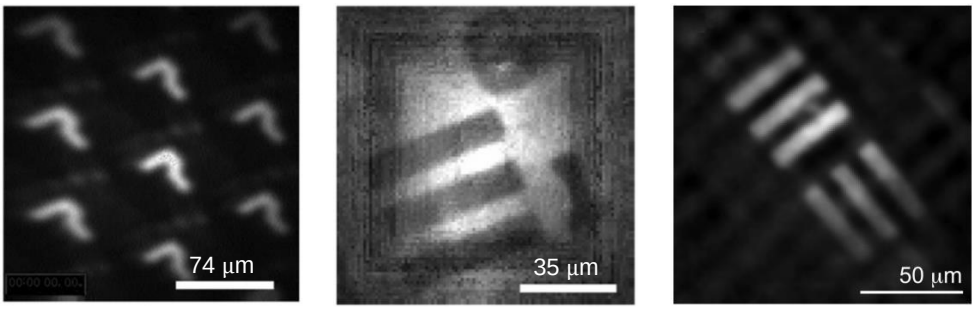

FIGURE 5.10: Imaging properties in lens-less endoscopes with different types of multi-core fiber. (a) Image of a resolution test chart using a multi-core fiber with a periodic layout from Ref. [50]. (b) Image of a resolution test chart using a multi-core fiber with a pseudo-random core layout from Ref. [99]. (c) Image using a multi-core fiber with a Fermat's golden spiral core layout from Ref. [81].

5.5 Fermat's golden spiral multi-core fiber

In this section, we will present a unique multi-core fiber which merges between the Fermat's golden spiral core layout approach (demonstrated in Ref. [81]) and

the tapering approach (presented in chapter 4). And so, to obtain a multi-core fiber that combines the advantages of both approaches.

We used the CMT model described in chapter 4 and we apply it to a Fermat's golden spiral core layout multi-core fiber, to predict the essential properties of an arbitrarily tapered Fermat multi-core fibers. Then we fabricate the tapered samples and characterize it. Finally, we apply the tapered samples in a two-photon lens-less endoscope system and quantify the gains in imaging performance.

5.5.1 Core layout

The positions of the core number n in a Fermat's spiral layout follow the relations

$$\rho_n = \Lambda\sqrt{n} \tag{5.7}$$

$$\theta_n = n\pi(3 - \sqrt{5}) \tag{5.8}$$

where ρ_n is the radial distance of the n'th core from the center core with $n = 0$, and θ_n is its corresponding azimuthal coordinate. The parameter Λ is a free parameter that controls the minimal spacing between the cores, and the golden angle constant, (3 - $\sqrt{5}$), results in non-redundant positions of the cores. This layout has the triple advantage of being deterministic, i.e. the core positions are determined from the simple generating function above; the resulting layout, while discrete, has no apparent periodicities; finally the layout also has a high packing fraction (cores per unit area) [100] with limited variance of nearest neighbor distances which facilitates the minimization of cross-talk between cores.

5.5.2 Predicted imaging properties

In this section we will present the properties of tapered Fermat multi-core fibers that are predicted by the CMT model from its structural parameters.

The un-tapered Fermat multi-core fiber ($t^{(\mathrm{im})} = 1$) used in this section has the following structural parameters: refractive index difference $\Delta n = 30{\cdot}10^{-3}$, core pitch $\Lambda = 11.7$ µm, core radius $a = 2.5$ µm, outer diameter $D^{(\mathrm{transport})} = 250$ µm and core number $N = 120$.

Point-spread function

The point-spread function resulting at distance $Z = Z_0 \cdot t^{(\mathrm{im})}$ from the distal end of Fermat's spiral multi-core fibers with $Z_0 = 500$ µm and $t^{(\mathrm{im})} = 1$, 0.6, and 0.4 is presented in Figure 5.11. As clearly shown, the Fermat's spiral multi-core fiber exhibits a point-spread function that is centrally peaked, in comparison with the point-spread function with multiple satellite peaks associated with the periodic hexagonal array multi-core fibers [Figures 4.6]. As shown by Figure 5.11(a) we still observe a non zero intensities in the parts of the point-spread function outside the central peak which is presented as a speckle background. However,

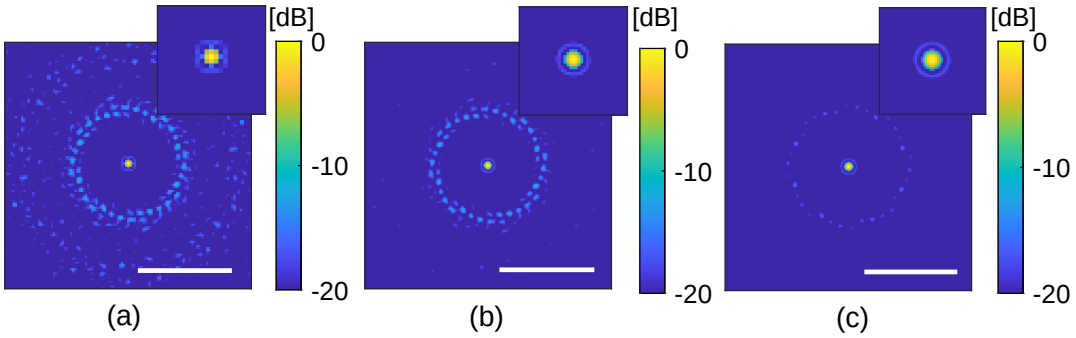

FIGURE 5.11: Point-spread function predicted by CMT model for (a) $t^{(\mathrm{im})} = 1.0$, (b) $t^{(\mathrm{im})} = 0.6$, and (c) $t^{(\mathrm{im})} = 0.4$ in a plane $Z = Z_0 \cdot t^{(\mathrm{im})}$. Each image is normalized to its maximum intensity. Scale bar in all images is 50 μm. Insets, 7× zoom on the central spot.

Figure 5.11(b) and 5.11(c) present the disappearance of this speckle background and an evident decrease in its intensity as the taper ratio $t^{(\mathrm{im})}$ decreases.

Memory effect

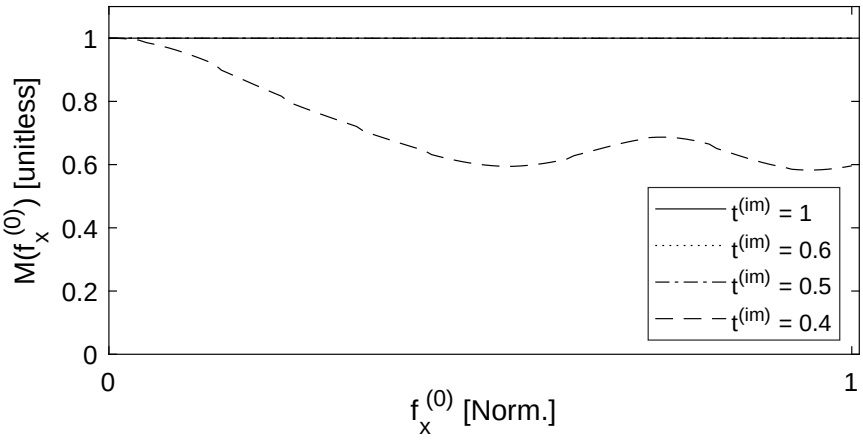

FIGURE 5.12: Memory effect curves predicted by CMT model for Fermat multi-core fibers with different taper ratios.

We compute the memory effect in the Fermat's multi-core fiber. Figure 5.12 presents the memory effect curves for different taper ratios $t^{(\mathrm{im})}$. The curves $t^{(\mathrm{im})} = 1$, 0.6 and 0.5 are coincident and constant equal to 1, which means conservation of full memory effect is retained in this Fermat multi-core fiber until $t^{(\mathrm{im})} = 0.5$. Moreover, the curve $t^{(\mathrm{im})} = 0.4$ which represent the smallest possible taper ratio while preserving core guidance descend slowly to a minimum value representing 60% of the full memory-effect, which means that even smallest possible taper ratio still conserve some memory effect. These results are actually reasonable as these tapered Fermat's multi-core fibers have an extremely low average cross-talk, as shown by Figure 5.13.

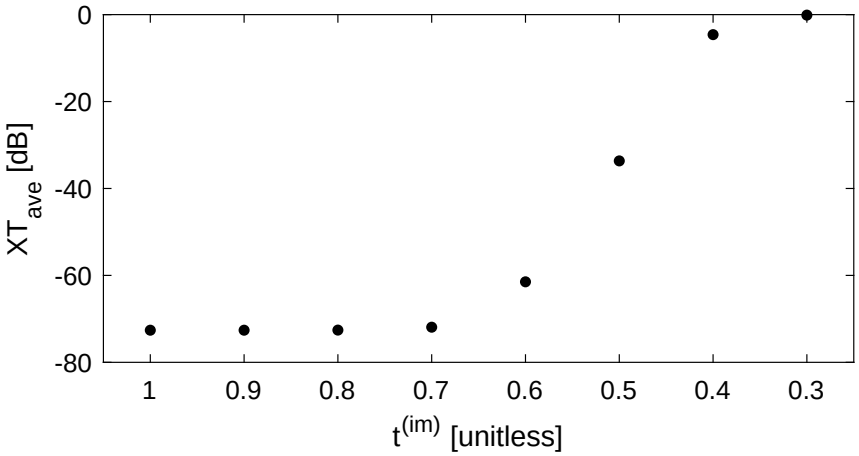

FIGURE 5.13: The The average total cross-talk Xave predicted by CMT model for Fermat multi- core fibers with different taper ratios.

Strehl ratio

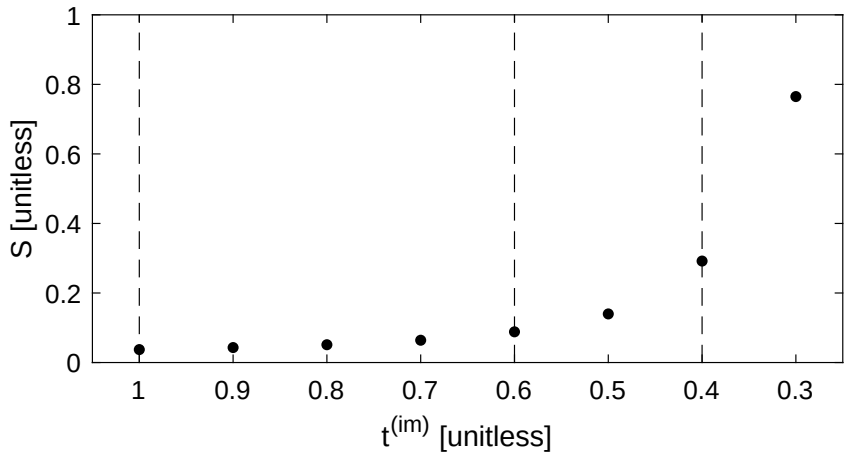

FIGURE 5.14: Strehl ratio of Fermat multi-core fibers with different taper ratios predicted by CMT model.

Figure 5.14 presents the predicted Strehl ratios of Fermat's multi-core fibers with different taper ratios $t^{(\mathrm{im})}$. The Strehl ratio show a slight increase with decreasing taper ratio, with a maximum possible value S ≈ 0.3 at $t^{(\mathrm{im})} = 0.4$.

5.5.3 Fabrication

The Fermat's golden spiral multi-core was fabricated from an existing preform, the one used in Ref. [81]. The fabrication of this fiber was done in the following way. Initially 120 holes of 2.1 mm diameter following the Fermat's spiral were drilled into a 50 mm silica rod to a depth of 230 mm. The standard deviations of the positions relative to the Fermat's spiral on both the inlet and outlet face were only around 4 µm and 90 µm, while the standard deviation on the

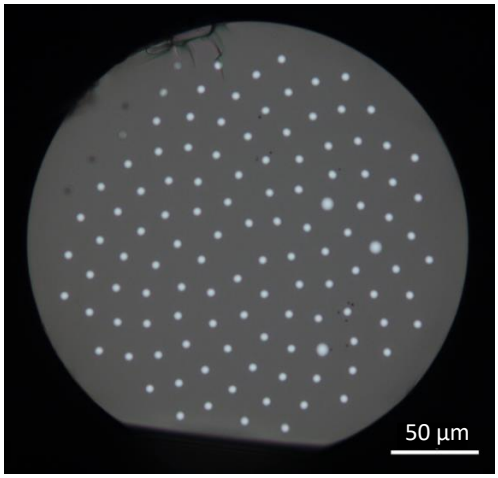

FIGURE 5.15: Microscope image of the Fermat's spiral multi-core fiber.

diameter was 15 µm. Germanium-doped silica glass rods drawn from a preform with a parabolic index and a maximum refractive index difference of $30 \cdot 10^{-3}$ relative to silica were then inserted into these holes.

For our project, we use this preform and redrew the fiber into the following final parameters: outer diameter of 250 µm, core diameter 2.5 µm. The end face of the drawn fiber is shown in Figure 5.15.

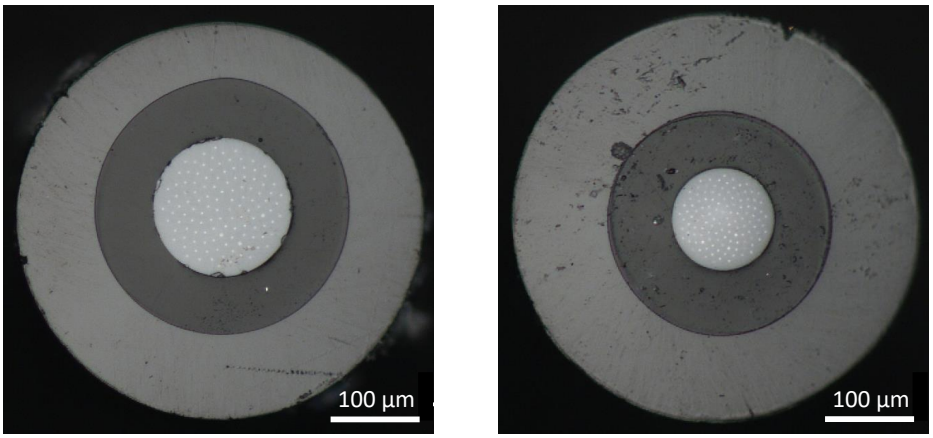

FIGURE 5.16: Polymer-coated Fermat multi-core fiber with taper ratio (a) $t^{(\mathrm{im})} = 0.6$ and (b) $t^{(\mathrm{im})} = 0.4$. Middle dark grey part is the low index polymer and external light grey part is the high index polymer.

Then we post-processed the uniform Fermat multi-core fiber to obtain the tapered Fermat multi-core fiber represented by Figure 5.2(a) by tapering a short length at two distinct positions of the uniform Fermat multi-core fiber using a CO_2 laser-based glass processing and splicing system (Detailed in Section 4.5.2). Next, we coated the the tapered fiber with low index polymer (n=1.37) and then with high index polymer (n=1.51) as sketched by Figure 5.2(b). As a final step we cut in the waist and polish the terminal ends of the fiber to obtain a

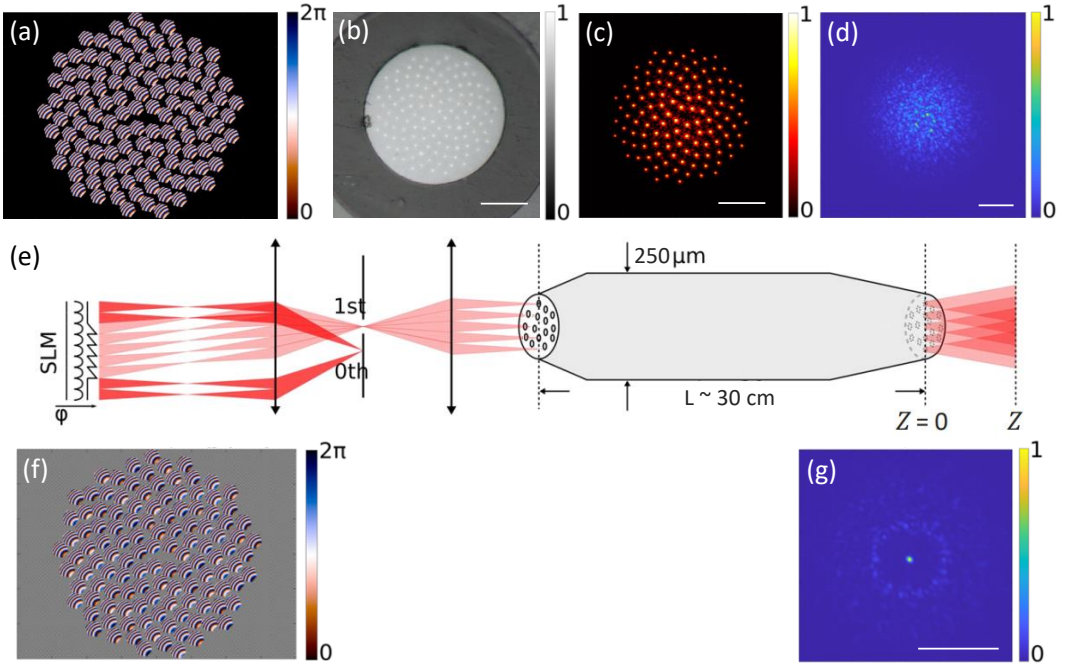

FIGURE 5.17: Schematic of incoupling of light at the proximal end and focusing at the distal end of a tapered polymer-coated Fermat multi-core fiber. Example for $t^{(\mathrm{im})} = 0.6$. (a) Phase mask on SLM for incoupling into 120 cores. (b) Microscope image of the Fermat multi-core fiber end face. (c) Intensity profile in the plane $Z = 0$ (logarithmic color scale). (d) Speckle seen in the plane Z with the phase mask (a) displayed on the SLM. (e) Sketch of light paths from SLM to the distal end of the tapered Fermat multi-core fiber. (f) Example of a phase mask which results in a focus at the distal end of the tapered Fermat multi-core fiber. (g) Example of intensity distribution in the plane Z with the phase mask (f) displayed on the SLM. Scale bars, 50 µm.

polymer-coated tapered Fermat multi-core fiber represented by Figure 5.2(c). The proximal and distal end faces of the polished Fermat multi-core fiber are shown by Figure 5.16(a) and Figure 5.16(b) respectively. Figure 5.16(a) represents the end face of a polymer-coated Fermat multi-core fiber tapered with taper ratio $t^{(\mathrm{im})} = 0.6$ and Figure 5.16(b) that of the one with taper ratio $t^{(\mathrm{im})} = 0.4$.

5.5.4 Two-photon excitation fluorescence imaging

To implement the Fermat multi-core fiber in lens-less endoscope system, we should first measure its transmission matrix. The measurement of the transmission matrix is acquired in the same way as the one presented in Section 4.7.1 in Chapter 4. But, with few changes to fit the use of the Fermat multi-core fiber. First, the phase mask displayed on the spatial light modulator is chosen in Fermat pattern (Figure 5.17) to be appropriate for efficient light incoupling into the individual fiber cores of the Fermat multi-core fiber (Figures 5.17(a),5.17(e)).

Then, we used the measured transmission matrix to produce a phase mask (typically resembling Figure 5.17(f)), which when displayed on the SLM resulted in the distal central focus that presents in Figure 5.17(g). This distal central focus stands for the experimentally measured point-spread function of the Fermat multi-core fiber. It is in line with the point-spread function predicted by the CMT model (Figure 5.11(b)), which show that Fermat multi-core fiber exhibits a centrally peaked point-spread function.

Once the transmission matrix is measured, we implemented the tapered polymer-coated Fermat multi-core fiber in a lens-less endoscopy system to acquire two-photon excitation fluorescence imaging in true endoscopic configuration as described in Section 5.3 and sketched in Figure 5.5. First, we imaged a 1 µm fluorescent beads to define endoscope performance. Figure 5.18(b) presents two-photon excited fluorescence image of 1 µm fluorescent beads in detected epi-direction with Fermat multi-core fiber of taper ratio $t^{(\mathrm{im})} = 0.4$. Comparing the TPEF image with the a transmission image of the same sample detected in forward-direction using LED as light source (Figure 5.18(a)) show the capability of this lens-less endoscope to aqcuire TPEF imaging in good resolution.

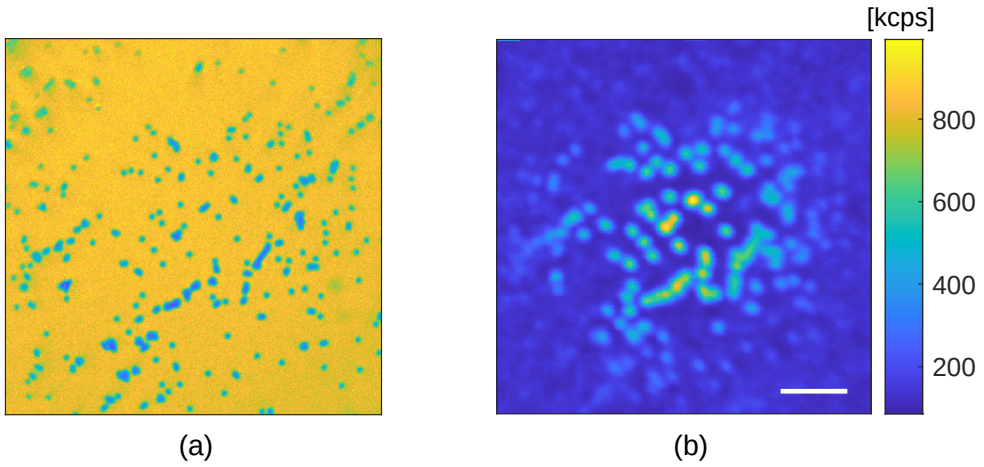

FIGURE 5.18: (a) One-photon transmission image of 1 µm fluorescent beads. (b) Two-photon excited fluorescence images of same sample, detected in epi-direction with a polymer-coated Fermat multi-core fiber with taper ratio $t^{(\mathrm{im})} = 0.4$ at $Z = 200$ µm. Scale bar, 20 µm.

We also acquire two-photon excited fluorescence images with Fermat multi-core fibers of different taper ratios. Figure 5.19 presents TPEF images of 1 µm fluorescent beads with Fermat multi-core fiber of $t^{(\mathrm{im})} = 0.6$ at $Z = 300$ µm from distal end of the fiber (Figure 5.19(a)) and of $t^{(\mathrm{im})} = 0.4$ at $Z = 200$ µm from distal end of the fiber(Figure 5.19(b)). The two images are detected in epi-direction by TM scan method. Comparing the intensity scales of the two images show the increase in two-photon signal with decreasing taper ratio $t^{(\mathrm{im})}$, as expected.

Furthermore, we also acquired two-photon excited fluorescence imaging of mammalian osteosarcoma cells, labelled with Alexa Fluor 488 dye. Figure 5.20 and Figure 5.21 present the TPEF images of mammalian osteosarcoma cells with

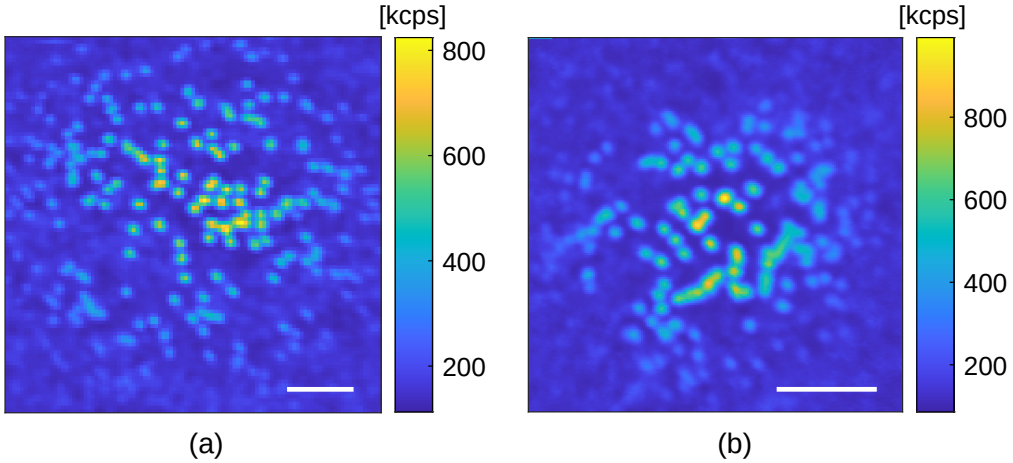

FIGURE 5.19: Two-photon excited fluorescence images of 1 µm fluorescent beads, detected in epi-direction with a polymer-coated Fermat MCF with taper ratio (a) $t^{(\mathrm{im})} = 0.6$ at $Z = 300$ µm and (b) $t^{(\mathrm{im})} = 0.4$ at $Z = 200$ µm. Scale bar, 20 µm.

Fermat multi-core fiber of taper ratios $t^{(\mathrm{im})} = 0.6$ (Figure 5.20) and $t^{(\mathrm{im})} = 0.6$ (Figure 5.21), also they present one-photon transmission images of the same cells for comparison. These TPEF images are detected in epi-direction by TM scan method. The cellular resolution and sensitivity is clearly demonstrated in the TPEF images, as compared to their similar images in transmission.

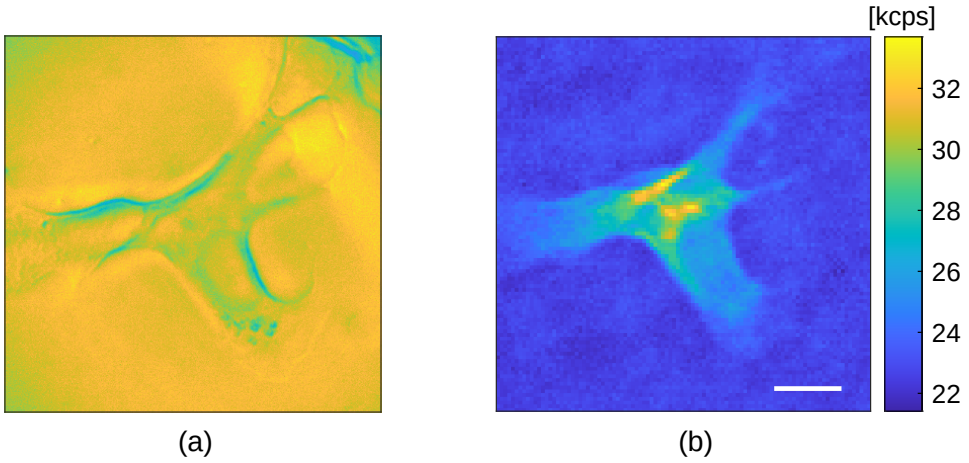

FIGURE 5.20: (a) One-photon transmission image of mammalian osteosarcoma cell. (b) Two-photon excited fluorescence images of same sample, detected in epi-direction with a polymer-coated Fermat MCF with taper ratio $t^{(\mathrm{im})} = 0.6$ at $Z = 300$ µm. Scale bar, 20 µm.

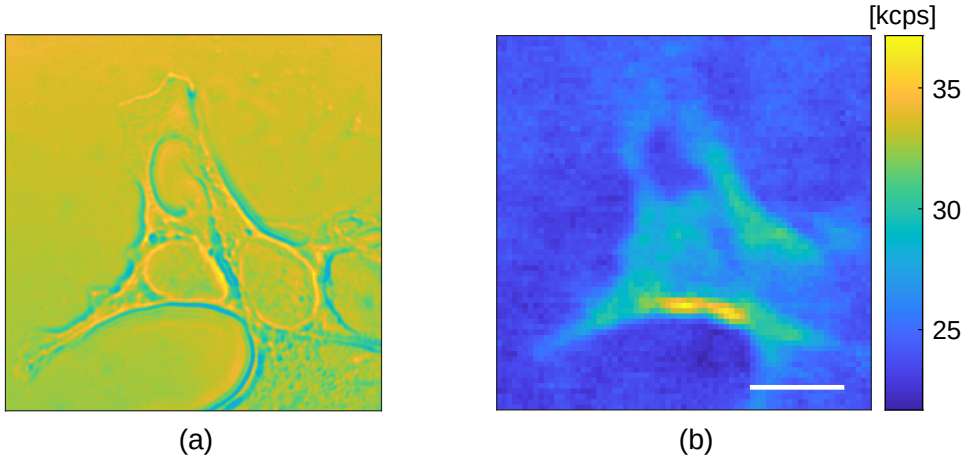

FIGURE 5.21: (a) One-photon transmission image of mammalian osteosarcoma cell. (b) Two-photon excited fluorescence images of same sample, detected in epi-direction with a polymer-coated Fermat multi-core fiber with taper ratio $t^{(\mathrm{im})} = 0.4$ at $Z = 200$ µm. Scale bar, 20 µm.

5.6 Photonic lantern

In this section, we will display a more advanced approach of lens-less endoscope "the photonic lantern" that can improve the generated output focus beyond the one that is already meliorated by the approach of tapered multi-core fiber. Photonic lantern will open the way to high resolution lens-less endoscope.

The photonic lantern is a specialty optical fibre which consists of a set of single-mode waveguides that are interfaced to a multi-mode waveguide through a physical waveguide transition. The function of this physical transition is to adiabatically form a multi-mode waveguide in which the single-mode waveguides form a composite waveguide via strong coupling. Therefore, the photonic lantern allows a low-loss transition from a set of single-mode fibers to a multi-mode fiber. Figure 5.22 is a schematic presentation of one type of photonic lantern.

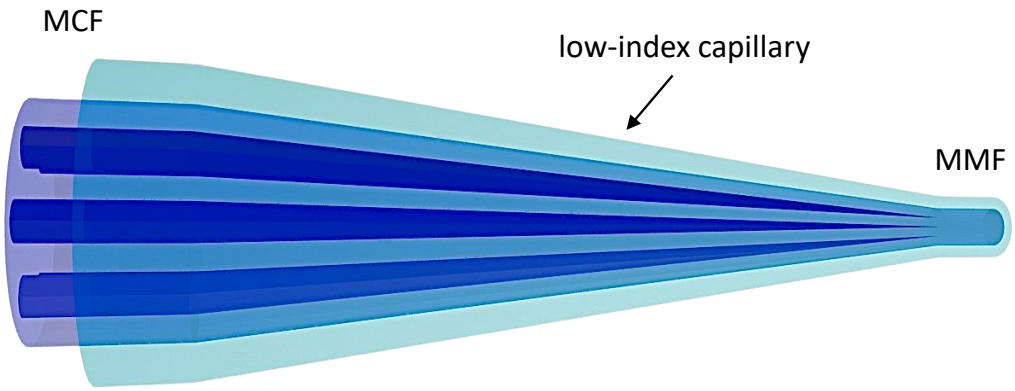

FIGURE 5.22: Sketch of photonic lantern.

5.6.1 Fabrication

To date, photonic lanterns have been manufactured and demonstrated by three different techniques; two using optical fibers [101, 102] and the third by using ultra-fast laser writing techniques [103, 104]. One approach using optical fibers for the realization of photonic lanterns is demonstrated by Leon-Saval et al. [105]. In this paper, a bundle of single-mode fibers is insert it into a low-index glass capillary tube, which is then fused and tapered down in a glass processing machine to form a multi-mode fiber at the other end. Another approach is demonstrated by Birks et al. by using a multi-core fiber with an array of identical single-mode cores [101]. In this paper, the multi-core fiber is jacketed with a low-index F-doped silica glass and then tapered down to form a multi-mode fiber with the F-doped silica its cladding.

Here, we fabricated the photonic lantern using the approach of multi-core fiber, but with a different technique. We start up by the uniform multi-core fiber that we optimized with the following parameters: refractive index difference $\Delta n = 30{\cdot}10^{-3}$, pitch size $\Lambda = 14$ µm, core radius $a = 2.5$ µm and cores number $N = 349$.

Then we post-processed the uniform multi-core fiber by tapering a short length at the terminals of the multi-core fiber using a CO_2 laser-based glass processing and splicing system (LZM-100 FUJIKURA) (Detailed in Section 4.5.2). First, we tapered the first terminal of the multi-core fiber (which will be the injection segment) with a taper ratio $t^{(\mathrm{inj})} = 0.6$, to avoid exciting the higher-order mode and ensure that only fundamental mode in guided in the transport segment. Then, at the second terminal of the fiber, which will be the imaging segment, we tapered the multi-core fiber with a sufficiently small taper ratio to create the photonic lantern. Then, the creation of the photonic lantern will be as follows. The imaging segment is tapered to the minimum so that, somewhere along the tapered section, the multi-core fiber cores become too small to guide light which will therefore couple into the cladding modes of the multi-core fiber. Afterwards, we jacket the whole tapered fiber with a low index capillary by coating it with low index polymer (as shown in Section 5.2.1). Consequently, the cladding modes become the guided modes of a multi-mode fiber having the low-index capillary as cladding. As a final step, we polished the two end-faces of the photonic lantern (polishing process is detailed in Section 5.2.2) to be ready to implemented in lens-less endoscopy setup.

The criterion of choosing the minimum taper ratio $t^{(\mathrm{im})}$ is to preserve the same number of modes between the multi-core fiber and the multi-mode fiber. Therefore, to get the mode matching, we should taper the multi-core fiber with $t^{(\mathrm{im})} \approx 0.09$, but this taper ratio was really too small and it was difficult to handle these tapered samples because of its fragility.

Therefore, we only taper the multi-core fiber down to $t^{(\mathrm{im})} = 0.175$ to end up with a multi-mode fiber of 57.75 µm core diameter, which was kind of the limit of what could be reasonably handled. Then we coat the whole tapered fiber with low index polymer (n=1.37) that we already use for polymer-coated multi-core fiber presented in the beginning of this chapter. This fabricated photonic lantern then has a multi-mode core with numerical aperture NA = 0.47. Figure 5.23 presents the microscopic images of the polymer-coated multi-core

end-face Figure 5.23(a) and the multi-mode end-face representing the photonic lantern Figure 5.23(b).

In fact, it would have been better to coat the fiber with a polymer of $n = 1.40$ refractive index, which was available from the supplier but unavailable at the time the fabrication was done. With this $n = 1.40$ polymer, we can get better matching at taper ratio $t^{(\mathrm{im})} \approx 0.175$, and the photonic lantern will then has a multi-mode core with numerical aperture NA $= 0.3775$.

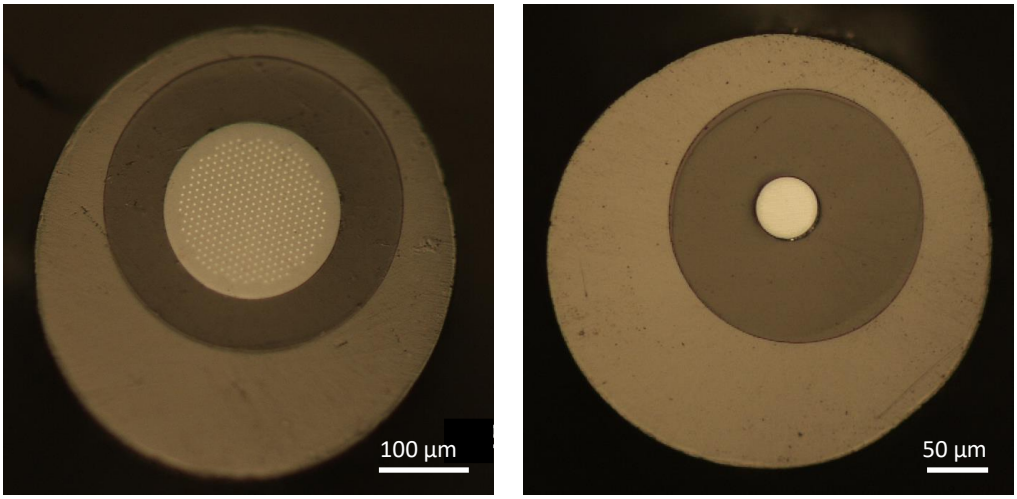

FIGURE 5.23: Microscope images of the (a) Polymer-coated MCF end-face with $t^{(\mathrm{inj})} = 0.6$ and (b) Multi-mode fiber end-face of the photonic lantern with $t^{(\mathrm{im})} = 0.175$.

5.6.2 How the photonic lantern works

As mentioned in the previous section, for creating the photonic lantern, the multi-core fiber is tapered enough until at some point in the taper transition the cores have reduced in size and separation enough for appreciable coupling to occur between them. In that part of the transition the single-mode cores are far apart enough to be distinct yet close enough to be weakly coupled, and the modes are described as supermodes. As a reminder, for N single-mode cores, there are also N supermodes. So, light injected in a certain single-mode core excites light in several modes of the multi-mode core, which is determined by the superposition of the supermodes.

Photonic lanterns can efficiently couple light from N single-mode cores to a multi-mode fiber with M modes, where the number of modes in the multi-mode fiber should in principle equals to the number of single-mode cores, $M = N$. Therefore, M distinct distal focus can be generated at the multi-mode output by coupling light into each core (one at a time) at the multi-core fiber input. As the multi-core fiber is being the transport segment of the photonic lantern, this gives it the advantage of the capability to be optimized for bend resilience [82] and negligible cross-talk between the cores along the length of the multi-core fiber, such that the light propagates along just one core. Consequently, the

distal focus generated from the multi-mode fiber do not change when bending the fibre, which is not the case with ordinary multi-mode fiber. In the other hand, like an ordinary multi-mode fibre, the photonic lantern allows the full area of the multi-mode fibre end-facet to be sampled, and the size of output (distal) focus can be reduced to the minimum allowed by the numerical aperture (NA) of the multi-mode core.

5.7 Conclusion

In this chapter, we have presented an extension and further advance of the work presented in Chapter 4. Where we have been coated the optimized tapered multi-core fiber with a low index polymer to act as a secondary cladding, and thus collect the two-photon signal in epi-direction, as a genuine lens-less endoscope. By imaging a 1 µm fluorescent beads and a mammalian osteosarcoma cells, we have shown that these polymer-coated tapered multi-core fibers are very efficient in collecting the two-photon signal in epi-direction.

We further tapered a Fermat multi-core fibers, coat them with low index polymer as a secondary cladding and apply them in a two-photon lens-less endoscope system to acquire two-photon excitation fluorescence imaging in epi-direction. An important feature in using the Fermat multi-core fiber is the absence of replica images that are seen when using the periodic hexagonal multi-core fibers. In fact, the properties of the presented Fermat multi-core fiber are not the definitive best ones can be taken by Fermat multi-core fiber. However, we can use the same procedure presented in Chapter 4 for optimizing the hexagonal multi-core fiber, to design an optimized Fermat multi-core fiber.

We also fabricated a photonic lantern, with the hexagonal multi-core fiber, however we actually didn't have the time to characterize it and apply it to the lens-less endoscope system.

Chapter 6

Conclusion and perspectives

During this thesis, we have introduced a novel specialty optical fiber component, a “tapered multi-core fiber”, designed for integration into ultra-miniaturized endoscopes for minimally-invasive two-photon point-scanning imaging. In Chapter 4 we have outlined the entire procedure of conception, design, fabrication, and application in a lens-less endoscopy system of this novel fiber-optic component. The procedure, namely the step involving the CMT model, is generic and applicable to other ranges of properties, other multi-core fiber core layouts, wavelength ranges, etc. We confirm that in Section 5.5, where we used the CMT model to predict the essential properties of a Fermat’s golden spiral multi-core fiber, which then implemented in a lens-less endoscope system and confirm the predictions.

In a further advance, in Chapter 5 we coated the tapered multi-core fiber samples with a low-index polymer to function as a second cladding, and we have shown that these polymer-coated tapered multi-core fibers are very efficient in collecting the two-photon signal in the epi-direction. Consequently, we were able to demonstrate a genuine lens-less endoscope. The cellular resolution and sensitivity of this genuine endoscope is demonstrated in a two-photon excitation fluorescence images of labelled mammalian osteosarcoma cells.

In Section 5.5 of Chapter 5, we presented the tapering of Fermat multi-core fiber that was drawn from an existing preform. The properties of the presented Fermat multi-core fiber are not the definitive best ones can be taken by Fermat multi-core fiber. However, we can use the same procedure presented in Chapter 4 for optimizing the hexagonal multi-core fiber, to design an optimized Fermat multi-core fiber. For instance, a Fermat multi-core fiber with the following parameters: core size $a = 2.5$ µm, core pitch $\Lambda = 8$ µm, refractive index difference $\Delta n = 30{\cdot}10^{-3}$, core number 120, outer diameter $D^{(\text{transport})} = 170$ µm can present an optimized generation of the Fermat multi-core fiber presented previously. This optimized fiber can achieve a lens-less endoscope with an optimized properties and a smaller probe size. Tapering this optimized generation fiber with taper ratio $t^{(\text{im})} = 0.6$ can maximize the Strehl ratio up to 10 % while conserving a "full" memory effect, and with taper ratio $t^{(\text{im})} = 0.4$ can maximize the Strehl ratio up to 45 % while conserving core guidance. An important property at $t^{(\text{im})} = 0.4$ is obtaining a clear single-peaked point-spread function, which in turn should permit to acquire an artifact-free image. The essential properties of the optimized Fermat multi-core fiber are presented in Appendix B.

In the last section of Chapter 5 we have displayed a more advanced approach of lens-less endoscopes represented by photonic lanterns (Section 5.6). The approach of photonic lanterns increase the numerical aperture of the fiber, which allow for a smaller effective pixels and thus increase in the imaging resolution. We have shown the fabrication of a photonic lantern, however more work is needed, an immediate work that can be done is the characterization of the fabricated sample, but it couldn't be done due to time constraints. Moreover, future work should use a low index polymer of $n = 1.4$ as a jacket for these lanterns, for better match in the number of modes between multi-core and multi-mode fiber.

In Chapter 3, we demonstrated a numerical investigation of a potential solution for ameliorating spatial resolution in lens-less endoscopes, using a short segment of structured multi-mode fiber. We have shown that this approach outperformed a similar reported idea. However, our approach still remains challenging to be applied experimentally. But the future might permit new ways of experimentally realizing the kind of wave guiding structures we displayed.

In the present thesis, we conclude that tailoring of the taper profile is a degree of freedom that can be efficiently exploited for ameliorating multi-core fiber based lens-less endoscopes, and we have shown here that it contributes to solving the major power delivery issue encountered by multi-core fiber based lens-less endoscopes. More generally a tapered multi-core fiber is a valuable add-on into the lens-less endoscope toolbox to design, optimize and fabricate ultra-miniaturized endoscope tailored to a broad range of applications. Moreover, the realization of two-photon lens-less endoscope using the tapered multi-core fibers opens the door to many other nonlinear image contrasts in these lens-less endoscopes. Any kind of nonlinear microscopy that can proceed by point-scanning, such as three-photon fluorescence, second-harmonic generation, and third-harmonic generation microscopy, could straightforwardly be implemented in our endoscope.

Future work should try to realize a lens-less endoscope that simultaneously combines all the advantages of multi-core fiber. A future work will be on a tapered multi-core fibers with increased resilience to bend. First step toward this goal is already taken. I have tapered a number of twisted Fermat multi-core fibers with different structural parameters, but due to time consideration, we were not able to characterize and apply these samples in a lens-less endoscope system. However, the near future work will focus on trying these samples in the lens-less endoscope setup. Tapering a twisted Fermat multi-core fiber will merge the advantages of three approaches in one single piece of multi-core fiber. And consequently, we will obtain an ultra-miniaturized genuine lens-less endoscope with the following properties: increased power delivery due to taper profile, enhanced image quality with single peaked point-spread function and increased field-of-view due to the Fermat layout, and increased resilience to bend due to twisted cores. This lens-less endoscope is going to be a promising imaging tool for in-vivo biomedical imaging and for measuring neuron activity in freely moving animals.

Appendix A

Overview of Matlab functions

Variable	Input/Output	Description
`lambda`	Input	Scalar. Units meters. The wavelength.
`l`	Input	Scalar. Unitless. The azimuthal number of LP modes.
`mmax`	Input	Scalar. Unitless. The maximum value of radial number of LP modes.
`function`	Input	Function. Pointer to a function n(r).
`h`	Input	Scalar. Steps of the finite difference method.
`rmax`	Input	Scalar. Units meters. Boundary of the calculations.
`a`	Input	Scalar. Units meters. Radius of the fiber core.
`n1`	Input	Scalar. Unitless. The maximum of the refractive index profile of the core.
`n2`	Input	Scalar. Unitless. The cladding refractive index.
`neff`	Output	Scalar. Unitless. The effective indices of modes.
`E`	Output	$[M \times 1]$. Arbitrary units. The field of the calculated mode as a function of the radial coordinate contained in variable `r`.
`r`	Output	$[1 \times M]$. Units meters. The radial coordinates at which variable `E` is evaluated.

Table A.1: Overview of mode solver function

.

Variable	**Input/Output**	**Description**
`Lseg_array`	Input	[$1 \times N_{\text{seg}}$]. Units meters. Contains the lengths of each of the N_{seg} segments into which the simulated tapered MCF is sub-divided.
`lambda`	Input	Scalar. Units meters. The wavelength of the laser.
`a0`	Input	Scalar. Units meters. Radius of a single core in a segment where `t_array = 1`. Article equivalent a, the radius of a single core in the transport segment.
`n1`	Input	Scalar. Unitless. The maximum of the refractive index profile of a single core.
`n2`	Input	Scalar. Unitless. The cladding refractive index.
`poscore0`	Input	[$N \times 2$]. Units metres. Positions of the N cores of the MCF in a segment where `t_array = 1`. Article equivalent $\{x_j^{(\text{core})}, y_j^{(\text{core})}\}$.
`t_array`	Input	[$1 \times N_{\text{seg}}$]. Unitless. Contains the homothetic scaling factors of each of the N_{seg} segments into which the simulated tapered MCF is sub-divided. Ie in a given segment the core radius and the core positions are scaled by this factor.
`neff`	Output	Scalar. Unitless. The effective index of the fundamental mode of an unperturbed core, ie without accounting for interaction between cores.
`E`	Output	[$N \times 1$]. Arbitrary units. The field of the fundamental mode of an unperturbed core as a function of the radial coordinate contained in variable `r`.
`r`	Output	[$1 \times N$]. Units meters. The radial coordinates at which variable `E` is evaluated.
`neffsuper`	Output	[$N \times N_{\text{seg}}$]. Unitless. The effective indices of the N supermodes of the tapered MCF, ie of the perturbed eigenmodes found by CMT. Contains N_{seg} columns correponding to the segments into which the simulated tapered MCF is sub-divided.
`TM`	Output	[$N \times N$]. Unitless. Transmission matrix of the simulated tapered MCF in the basis of the fundamental modes of the N cores. Article equivalent $\mathbf{H}$.

TABLE A.2: Overview of the Matlab function of the CMT model

.

Appendix B

Optimized Fermat multi-core fiber

We have used the CMT model to identify the design parameters of an optimized Fermat multi-core fiber with suitable properties for two-photon lens-less imaging with a pulsed 920 nm excitation laser. Consequently, we found the following parameters: core size $a = 2.5$ µm, core pitch $\Lambda = 8$ µm, refractive index difference $\Delta n = 30 \cdot 10^{-3}$, core number 120, outer diameter $D^{(\text{transport})} = 170$ µm. These parameters have been found by following the same procedure presented in Section 4.4 in Chapter 4.

The essential properties predicted by the CMT model are presented in Figure B.1. From this figure, we identify $t^{(\text{im})} = 0.6$ for maximum Strehl ratio while retaining full memory effect (Figure B.1(d)), and $t^{(\text{im})} = 0.4$ for maximum Strehl ratio while retaining core guidance (Figure B.1(f)). Figures B.1(a)-B.1(c) present the predicted point-spread functions at distance $Z = Z_0 \cdot t^{(\text{im})}$ from the distal end of Fermat multi-core fibers with $Z_0 = 500$ µm and $t^{(\text{im})} = 1$, 0.6, and 0.4. The Fermat multi-core fibers exhibit a point-spread function that is centrally peaked, but with speckle background of non zero intensities. However, the non-zero intensities that appear in the background decrease as we decrease the taper ratio, until we obtain a clear single peaked point-spread function at $t^{(\text{im})} = 0.4$ (Figure B.1(c)). Indeed, this is very beneficial for image quality, where it permit to acquire an artifact-free image.

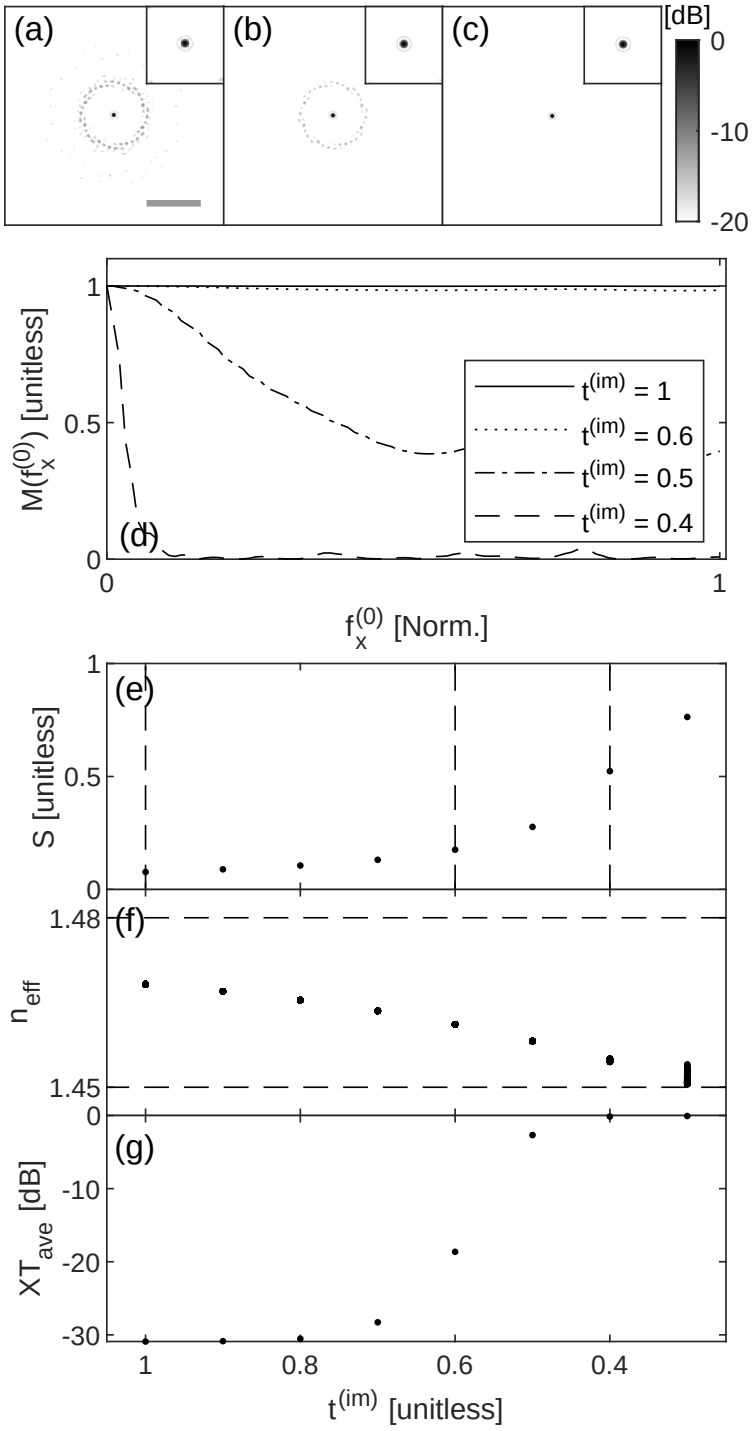

FIGURE B.1: Properties of tapered Fermat MCF predicted by CMT model. (a)-(c) PSF for $t^{(\mathrm{im})} = 1.0$, 0.6, and 0.4 in a plane $Z = Z_0 \cdot t^{(\mathrm{im})}$. Each image is normalized to its maximum intensity. Scale bar, 50 μm. Insets, 5× zoom on the central spot. (d) Memory effect curves. Horizontal axis normalized to half the distance between replica spots. (e) Strehl ratio. (f) Effective indices of supermodes. (g) Average XT.

Bibliography

[1] Liu Jia-Ming. "Photonic devices". In: *Cambridge university text* (2005).

[2] Allan W Snyder. "Asymptotic expressions for eigenfunctions and eigenvalues of a dielectric or optical waveguide". In: *IEEE Transactions on microwave theory and techniques* 17.12 (1969), pp. 1130–1138.

[3] Detlef Gloge. "Weakly guiding fibers". In: *Applied optics* 10.10 (1971), pp. 2252–2258.

[4] Jacques Bures. *Guided optics: Optical fibers and all-fiber components*. John Wiley & Sons, 2009.

[5] John Robinson Pierce. "Coupling of modes of propagation". In: *Journal of Applied Physics* 25.2 (1954), pp. 179–183.

[6] SE Miller. "Coupled wave theory and waveguide applications". In: *Bell System Technical Journal* 33.3 (1954), pp. 661–719.

[7] SA Schelkunoff. "Conversion of Maxwell's equations into generalized telegraphist's equations". In: *Bell System Technical Journal* 34.5 (1955), pp. 995–1043.

[8] Hermann A Haus. "Electron beam waves in microwave tubes". In: (1958).

[9] Allan W Snyder. "Coupling of modes on a tapered dielectric cylinder". In: *IEEE transactions on microwave theory and techniques* 18.7 (1970), pp. 383–392.

[10] Allan W Snyder. "Coupled-mode theory for optical fibers". In: *JOSA* 62.11 (1972), pp. 1267–1277.

[11] Dietrich Marcuse. "The coupling of degenerate modes in two parallel dielectric waveguides". In: *Bell System Technical Journal* 50.6 (1971), pp. 1791–1816.

[12] D Marcuse. "Coupled mode theory of round optical fibers". In: *Bell System Technical Journal* 52.6 (1973), pp. 817–842.

[13] Amnon Yariv. "Coupled-mode theory for guided-wave optics". In: *IEEE Journal of Quantum Electronics* 9.9 (1973), pp. 919–933.

[14] Herwig Kogelnik. "2. Theory of dielectric waveguides". In: *Integrated optics*. Springer, 1975, pp. 13–81.

[15] HF Taylor. "Optical switching and modulation in parallel dielectric waveguides". In: *Journal of Applied Physics* 44.7 (1973), pp. 3257–3262.

[16] Juichi Noda, Masaharu Fukuma, and Osamu Mikami. "Design calculations for directional couplers fabricated by Ti-diffused LiNbO 3 waveguides". In: *Applied Optics* 20.13 (1981), pp. 2284–2290.

[17] Peter D McIntyre and Allan W Snyder. "Power transfer between optical fibers". In: *JOSA* 63.12 (1973), pp. 1518–1527.

[18] C Yeh et al. "Accuracy of directional coupler theory in fiber or integrated optics applications". In: *JOSA* 68.8 (1978), pp. 1079–1083.

[19] K Thyagarajan and Ramanand Tewari. "Accurate analysis of single-mode graded-index fiber directional couplers". In: *Journal of lightwave technology* 3.1 (1985), pp. 59–62.

[20] Peter D McIntyre and Allan W Snyder. "Power transfer between non-parallel and tapered optical fibers". In: *JOSA* 64.3 (1974), pp. 285–288.

[21] B Crosignani, CH Papas, and P Di Porto. "Coupled-mode theory approach to nonlinear pulse propagation in optical fibers". In: *Optics Letters* 6.2 (1981), pp. 61–63.

[22] Bruno Crosignani, Antonello Cutolo, and Paolo Di Porto. "Coupled-mode theory of nonlinear propagation in multimode and single-mode fibers: envelope solitons and self-confinement". In: *JOSA* 72.9 (1982), pp. 1136–1141.

[23] DR Andersen, S Datta, and RL Gunshor. "A coupled mode approach to modulation instability and envelope solitons". In: *Journal of applied physics* 54.10 (1983), pp. 5608–5612.

[24] Stephen Jensen. "The nonlinear coherent coupler". In: *IEEE Journal of Quantum Electronics* 18.10 (1982), pp. 1580–1583.

[25] Allan W Snyder and Yijiang Chen. "Nonlinear fiber couplers: switches and polarization beam splitters". In: *Optics letters* 14.10 (1989), pp. 517–519.

[26] D Marcuse. *Light Transmission Optics. Bell Laboratory Series. New York, Cincinnati*. 1972.

[27] A Snyder and J Love. *Optical waveguide theory.-London: Chapman & Hall*. 1983.

[28] RC Alferness et al. *Guided-wave optoelectronics*. Vol. 26. Springer Science & Business Media, 2013.

[29] Govind P Agrawal. "Nonlinear fiber optics". In: *Nonlinear Science at the Dawn of the 21st Century*. Springer, 2000, pp. 195–211.

[30] Allan W Snyder and John Love. *Optical waveguide theory*. Springer Science & Business Media, 1984.

[31] Daniel Malacara-Hernández, Zacarıas Malacara-Hernández, and Zacarias Malacara. *Handbook of optical design*. CRC Press, 2003.

[32] Joseph W Goodman. "Introduction to Fourier optics. 3rd". In: *Roberts and Company Publishers* (2005).

[33] Marcus Reicherter et al. "Optical particle trapping with computer-generated holograms written on a liquid-crystal display". In: *Optics letters* 24.9 (1999), pp. 608–610.

[34] Brian Herman. *Fluorescence microscopy*. Garland Science, 2020.

[35] Marvin Minsky. "Memoir on inventing the confocal scanning microscope". In: *Scanning* 10.4 (1988), pp. 128–138.

[36] James Pawley. *Handbook of biological confocal microscopy*. Vol. 236. Springer Science & Business Media, 2006.

[37] Tony Wilson. "The role of the pinhole in confocal imaging system". In: *Handbook of biological confocal microscopy*. Springer, 1995, pp. 167–182.

[38] Winifried Denk, James H Strickler, and Watt W Webb. "Two-photon laser scanning fluorescence microscopy". In: *Science* 248.4951 (1990), pp. 73–76.

[39] Patrick Theer, Mazahir T Hasan, and Winfried Denk. "Two-photon imaging to a depth of 1000 μm in living brains by use of a Ti: Al 2 O 3 regenerative amplifier". In: *Optics letters* 28.12 (2003), pp. 1022–1024.

[40] Alexander Hopt and Erwin Neher. "Highly nonlinear photodamage in two-photon fluorescence microscopy". In: *Biophysical journal* 80.4 (2001), pp. 2029–2036.

[41] Jayne M Squirrell et al. "Long-term two-photon fluorescence imaging of mammalian embryos without compromising viability". In: *Nature biotechnology* 17.8 (1999), pp. 763–767.

[42] George H Patterson and David W Piston. "Photobleaching in two-photon excitation microscopy". In: *Biophysical journal* 78.4 (2000), pp. 2159–2162.

[43] Sébastien M Popoff et al. "Measuring the transmission matrix in optics: an approach to the study and control of light propagation in disordered media". In: *Physical review letters* 104.10 (2010), p. 100601.

[44] Ioannis N Papadopoulos et al. "Focusing and scanning light through a multimode optical fiber using digital phase conjugation". In: *Optics express* 20.10 (2012), pp. 10583–10590.

[45] Etienne Cuche, Pierre Marquet, and Christian Depeursinge. "Simultaneous amplitude-contrast and quantitative phase-contrast microscopy by numerical reconstruction of Fresnel off-axis holograms". In: *Applied optics* 38.34 (1999), pp. 6994–7001.

[46] SM Popoff et al. "Controlling light through optical disordered media: transmission matrix approach". In: *New Journal of Physics* 13.12 (2011), p. 123021.

[47] Jacopo Bertolotti et al. "Non-invasive imaging through opaque scattering layers". In: *Nature* 491.7423 (2012), pp. 232–234.

[48] Ivo M Vellekoop, Aart Lagendijk, and AP Mosk. "Exploiting disorder for perfect focusing". In: *Nature photonics* 4.5 (2010), pp. 320–322.

[49] Esben Ravn Andresen et al. "Toward endoscopes with no distal optics: video-rate scanning microscopy through a fiber bundle". In: *Optics letters* 38.5 (2013), pp. 609–611.

[50] Esben Ravn Andresen et al. "Ultrathin endoscopes based on multicore fibers and adaptive optics: a status review and perspectives". In: *Journal of biomedical optics* 21.12 (2016), p. 121506.

[51] Yaniv Ziv et al. "Long-term dynamics of CA1 hippocampal place codes". In: *Nature neuroscience* 16.3 (2013), pp. 264–266.

[52] Yaniv Ziv and Kunal K Ghosh. "Miniature microscopes for large-scale imaging of neuronal activity in freely behaving rodents". In: *Current opinion in neurobiology* 32 (2015), pp. 141–147.

[53] Alexander M Aravanis et al. "An optical neural interface: in vivo control of rodent motor cortex with integrated fiberoptic and optogenetic technology". In: *Journal of neural engineering* 4.3 (2007), S143.

[54] Tomáš Čižmár and Kishan Dholakia. "Shaping the light transmission through a multimode optical fibre: complex transformation analysis and applications in biophotonics". In: *Optics express* 19.20 (2011), pp. 18871–18884.

[55] Alex J Thompson et al. "Adaptive phase compensation for ultracompact laser scanning endomicroscopy". In: *Optics letters* 36.9 (2011), pp. 1707–1709.

[56] Youngwoon Choi et al. "Scanner-free and wide-field endoscopic imaging by using a single multimode optical fiber". In: *Physical review letters* 109.20 (2012), p. 203901.

[57] Benjamin A Flusberg et al. "High-speed, miniaturized fluorescence microscopy in freely moving mice". In: *Nature methods* 5.11 (2008), pp. 935–938.

[58] YongKeun Park et al. "Speckle-field digital holographic microscopy". In: *Optics express* 17.15 (2009), pp. 12285–12292.

[59] Viktor Tsvirkun et al. "Widefield lensless endoscopy with a multicore fiber". In: *Optics Letters* 41.20 (2016), pp. 4771–4774.

[60] Marc Davenne et al. "In vivo imaging of migrating neurons in the mammalian forebrain". In: *Chemical senses* 30.suppl_1 (2005), pp. i115–i116.

[61] Fritjof Helmchen et al. "A miniature head-mounted two-photon microscope: high-resolution brain imaging in freely moving animals". In: *Neuron* 31.6 (2001), pp. 903–912.

[62] Alberto Lombardini et al. "High-resolution multimodal flexible coherent Raman endoscope". In: *Light: Science & Applications* 7.1 (2018), pp. 1–8.

[63] Juergen Sawinski et al. "Visually evoked activity in cortical cells imaged in freely moving animals". In: *Proceedings of the National Academy of Sciences* 106.46 (2009), pp. 19557–19562.

[64] Weijian Zong et al. "Fast high-resolution miniature two-photon microscopy for brain imaging in freely behaving mice". In: *Nature methods* 14.7 (2017), pp. 713–719.

[65] Rajesh S Pillai, Dirk Lorenser, and David D Sampson. "Deep-tissue access with confocal fluorescence microendoscopy through hypodermic needles". In: *Optics express* 19.8 (2011), pp. 7213–7221.

[66] Siddharth Sivankutty et al. "Ultra-thin rigid endoscope: two-photon imaging through a graded-index multi-mode fiber". In: *Optics express* 24.2 (2016), pp. 825–841.

[67] Esben Ravn Andresen et al. "Two-photon lensless endoscope". In: *Optics express* 21.18 (2013), pp. 20713–20721.

[68] Martin Plöschner, Tomáš Tyc, and Tomáš Čižmár. "Seeing through chaos in multimode fibres". In: *Nature Photonics* 9.8 (2015), pp. 529–535.

[69] Jean Yammine et al. "Time-dependence of the transmission matrix of a specialty few-mode fiber". In: *APL Photonics* 4.2 (2019), p. 022904.

[70] Joel Carpenter, Benjamin J Eggleton, and Jochen Schröder. "110x110 optical mode transfer matrix inversion". In: *Optics express* 22.1 (2014), pp. 96–101.

[71] Damien Loterie et al. "Digital confocal microscopy through a multimode fiber". In: *Optics express* 23.18 (2015), pp. 23845–23858.

[72] Eirini Kakkava et al. "Selective femtosecond laser ablation via two-photon fluorescence imaging through a multimode fiber". In: *Biomedical optics express* 10.2 (2019), pp. 423–433.

[73] Donald B Conkey et al. "High power, ultrashort pulse control through a multi-core fiber for ablation". In: *Optics express* 25.10 (2017), pp. 11491–11502.

[74] Donggyu Kim et al. "Toward a miniature endomicroscope: pixelation-free and diffraction-limited imaging through a fiber bundle". In: *Optics letters* 39.7 (2014), pp. 1921–1924.

[75] Shay Ohayon et al. "Minimally invasive multimode optical fiber microendoscope for deep brain fluorescence imaging". In: *Biomedical optics express* 9.4 (2018), pp. 1492–1509.

[76] Sergey Turtaev et al. "High-fidelity multimode fibre-based endoscopy for deep brain in vivo imaging". In: *Light: Science & Applications* 7.1 (2018), pp. 1–8.

[77] Sebastian A Vasquez-Lopez et al. "Subcellular spatial resolution achieved for deep-brain imaging in vivo using a minimally invasive multimode fiber". In: *Light: Science & Applications* 7.1 (2018), pp. 1–6.

[78] Y. Kim et al. "Adaptive Multiphoton Endomicroscope Incorporating a Polarization-Maintaining Multicore Optical Fibre". In: *IEEE J. Sel. Top. Quantum. Electron.* 22.3 (2016), pp. 171–178. DOI: 10.1109/JSTQE.2015.2488283.

[79] Ioannis N Papadopoulos et al. "Increasing the imaging capabilities of multimode fibers by exploiting the properties of highly scattering media". In: *Optics letters* 38.15 (2013), pp. 2776–2778.

[80] S. Sivankutty et al. "Miniature 120-beam coherent combiner with 3D-printed optics for multicore fiber-based endoscopy". In: *Opt. Lett.* 46 (2021), pp. 4968–4971. DOI: 10.1364/OL.435063.

[81] Siddharth Sivankutty et al. "Nonlinear imaging through a Fermat's golden spiral multicore fiber". In: *Optics letters* 43.15 (2018), pp. 3638–3641.

[82] Victor Tsvirkun et al. "Flexible lensless endoscope with a conformationally invariant multi-core fiber". In: *Optica* 6.9 (2019), pp. 1185–1189.

[83] Andrew D Yablon. *Optical fiber fusion splicing*. Vol. 103. Springer Science & Business Media, 2005.

[84] Anthony F Mills. *Basic heat and mass transfer*. Pearson College Division, 1999.

[85] John Conrad Jaeger and Horatio Scott Carslaw. *Conduction of heat in solids*. Clarendon P Oxford, United Kingdom: 1959.

[86] MN McLandrich. "Core dopant profiles in weakly fused single-mode fibres". In: *Electronics Letters* 24.1 (1988), pp. 8–10.

[87] GS Kliros and N Tsironikos. "Variational analysis of propagation characteristics in thermally diffused expanded core fibers". In: *Optik* 116.8 (2005), pp. 365–374.

[88] Kazuo Shiraishi, Yoshizo Aizawa, and Shojiro Kawakami. "Beam expanding fiber using thermal diffusion of the dopant". In: *Journal of lightwave technology* 8.8 (1990), pp. 1151–1161.

[89] Fatima El Moussawi et al. "Tapered Multicore Fiber for Lensless Endoscopes". In: *ACS Photonics* 9.8 (2022), pp. 2547–2554. DOI: 10.1021/acsphotonics.2c00661. eprint: https://doi.org/10.1021/acsphotonics.2c00661. URL: https://doi.org/10.1021/acsphotonics.2c00661.

[90] Isaac Freund, Michael Rosenbluh, and Shechao Feng. "Memory effects in propagation of optical waves through disordered media". In: *Physical review letters* 61.20 (1988), p. 2328.

[91] Masanori Koshiba and Yasuhide Tsuji. "A wide-angle finite-element beam propagation method". In: *IEEE Photonics Technology Letters* 8.9 (1996), pp. 1208–1210.

[92] JC Roper et al. "Minimizing group index variations in a multicore endoscope fiber". In: *IEEE Photonics Technology Letters* 27.22 (2015), pp. 2359–2362.

[93] James Crawford Roper. "Advances in multicore optical fibres for endoscopy". PhD thesis. University of Bath, 2015.

[94] Esben Ravn Andresen et al. "Measurement and compensation of residual group delay in a multi-core fiber for lensless endoscopy". In: *JOSA B* 32.6 (2015), pp. 1221–1228.

[95] F Bilodeau et al. "Low-loss highly overcoupled fused couplers: Fabrication and sensitivity to external pressure". In: *Journal of Lightwave Technology* 6.10 (1988), pp. 1476–1482.

[96] Y Takeuchi and J Noda. "Novel fiber coupler tapering process using a microheater". In: *IEEE photonics technology letters* 4.5 (1992), pp. 465–467.

[97] JM Bennett and RJ King. "Effect of polishing technique on the roughness and residual surface film on fused quartz optical flats". In: *Applied Optics* 9.1 (1970), pp. 236–238.

[98] Philip St J Russell. "Photonic-crystal fibers". In: *Journal of lightwave technology* 24.12 (2006), pp. 4729–4749.

[99] Siddharth Sivankutty et al. "Extended field-of-view in a lensless endoscope using an aperiodic multicore fiber". In: *Optics letters* 41.15 (2016), pp. 3531–3534.

[100] Helmut Vogel. "A better way to construct the sunflower head". In: *Mathematical biosciences* 44.3-4 (1979), pp. 179–189.

[101] Tim A Birks et al. ""Photonic lantern" spectral filters in multi-core fibre". In: *Optics Express* 20.13 (2012), pp. 13996–14008.

[102] Danny Noordegraaf et al. "Efficient multi-mode to single-mode coupling in a photonic lantern". In: *Optics express* 17.3 (2009), pp. 1988–1994.

[103] Robert R Thomson et al. "Ultrafast laser inscription of an integrated photonic lantern". In: *Optics express* 19.6 (2011), pp. 5698–5705.

[104] Izabela Spaleniak et al. "Multiband processing of multimode light: combining 3D photonic lanterns with waveguide Bragg gratings". In: *Laser & Photonics Reviews* 8.1 (2014), pp. L1–L5.

[105] Sergio G Leon-Saval et al. "Multimode fiber devices with single-mode performance". In: *Optics letters* 30.19 (2005), pp. 2545–2547.